REVEALING MECHANISMS OF MORPHOLOGICAL AND DYNAMICAL TRANSFORMATION OF THE ACTIN CYTOSKELETON

by
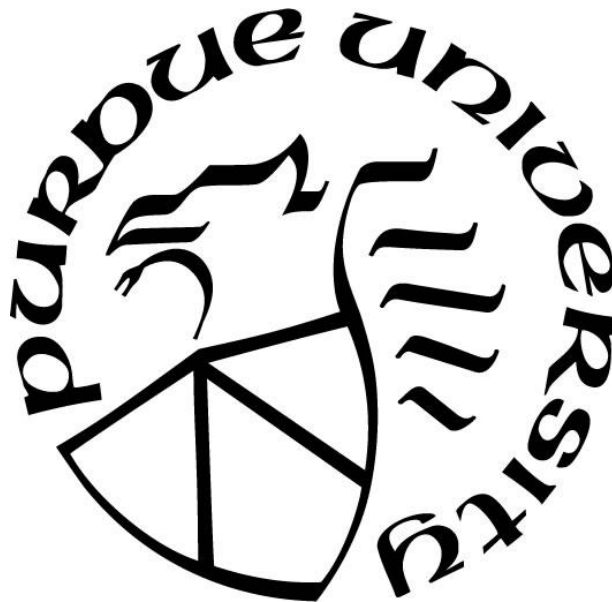
Wonyeong Jung

A Dissertation

Submitted to the Faculty of Purdue University

In Partial Fulfillment of the Requirements for the degree of

Doctor of Philosophy

Weldon School of Biomedical Engineering

West Lafayette, Indiana

August 2021

THE PURDUE UNIVERSITY GRADUATE SCHOOL
STATEMENT OF COMMITTEE APPROVAL

Dr. Taeyoon Kim, Chair

Weldon School of Biomedical Engineering

Dr. David Umulis

Department of Agricultural and Biological Engineering,
Weldon School of Biomedical Engineering

Dr. Eric A. Nauman

School of Mechanical Engineering,
Weldon School of Biomedical Engineering

Dr. Hector Gomez

School of Mechanical Engineering,
Weldon School of Biomedical Engineering

Approved by:

Dr. George R. Wodicka

ACKNOWLEDGMENTS

I am greatly thankful to my doctoral advisor, Professor Taeyoon Kim, for all the support and guidance. Thanks for providing me with ample opportunities to grow and believing in me. I always feel grateful to have the best advisor.

I would like to express my gratitude to my committee members to guide academic and professional development. I would like to thank Professor Eric Nauman for helping and guiding me to improve my research via discussion and questions on computational modeling. I also thank Professor David Umulis for providing me with valuable feedback on research and communication. I am grateful to Professor Hector Gomez for always encouraging me during this journey.

Several of the research projects described in this dissertation were conducted with collaborators. I would like to thank Professor Pasha Tabatabai (Seattle University) and Professor Michael Murrell (Yale University) for their collaboration in the myosin motion project (Ch. 5). I am grateful to Professor Ali Tabei (University of Northern Iowa) for discussions and encouragement throughout the project. Kyohei Matsuda and Professor Junichiro Yajima (The University of Tokyo) provided me with an exciting and helpful opportunity to collaborate with them (Ch. 4).

Help from colleagues and friends has been essential during my graduate study. Friendship with them enabled me to learn new things and grow as a person.

Finally, I want to thank my parents for their love and support.

TABLE OF CONTENTS

LIST OF TABLES

LIST OF FIGURES

change much at later times. Effects of $\kappa_{r,A}$ are weaker if C_A is smaller. (D) A schematic diagram showing differences in behaviors of F-actins after collisions with other F-actins. If volume-exclusion effects are very weak, F-actins cross over each other easily. If volume-exclusion effects are relatively strong, F-actins can align with each other if a contact angle at the moment of collision is small. However, they cross over each other if the angle is large. This behavior results in formation of thick, large bundles. With very strong volume-exclusion effects, F-actins cannot cross over each other regardless of whether the contact angle is large or small. Such a frequent change in the direction leads to formation of many, small ring-like structures. 51

Figure 2.10. Impacts of the extent of volume-exclusion effects on network morphology and collective motions of F-actins with three different actin concentrations (C_A = 30, 60, and 120 µM). (A) Heterogeneity of F-actin spatial distribution (Q_A). (B) A correlation between final network morphology at 100 s and morphology at each time point, t. (C-D) A correlation between velocities of two points on different F-actins located (C) near a distance r or (D) within 0.2 µm. The correlation values are averaged for last 50 s. 52

Figure 2.11. Motions and properties of F-actins drastically change depending on density (R_{ACP}) and zero-force unbinding rate constant ($k_{u,ACP}^0$) of ACPs. (a) Average speed of F-actin averaged for last 50 s. (b) Heterogeneity of F-actin spatial distribution and (c) network morphology measured in all cases at the last time point, t = 100 s. F-actins and ACPs are visualized by cyan and yellow, respectively. White dashed lines in (a-b) are drawn to include cases with $k_{u,ACP}^0$ = 0 in a log scale, so there is a discontinuity between the cases separated by the white dashed line 54

Figure 2.12. Influences of density (R_{ACP}) and zero-force unbinding rate constant ($k_{u,ACP}^0$) of ACPs. (A) Speed distribution of F-actins. (B) Autocorrelation of velocities of F-actins. A spike at low τ in some curves originates from severe confinement of F-actins. (C) Heterogeneity of F-actin spatial distribution (Q_A). (D) Time evolution of average tensile force acting on F-actins. (E) A correlation between unit tangential vectors along contour of F-actins. Dotted lines indicate the correlation corresponding to the persistence length of F-actin. 55

Figure 2.13. Effects of the density (R_{ACP}) and zero-force unbinding rate constant ($k_{u,ACP}^0$) of ACPs. (a) The fraction of active ACPs, which are ACPs that are bound to two F-actins. The fraction was averaged for last 50 s. (b) Tensile force acting on F-actins averaged for last 50 s. (c) Force exerted by motor arms averaged for last 50 s. White dashed lines in (a-c) are drawn to include cases with $k_{u,ACP}^0$ = 0 in a log scale, so there is a discontinuity between the cases separated by the white dashed line. (d) Visualization of spatial distribution of spring energy density in networks measured at t = 100 s via color scaling 57

Figure 3.1. Schematic of Model Setup. (A) Computational domain of the model setup. (B) Representation of interactions between actin and myosin. 68

Figure 3.2. Myosin and Unbinding Rate depend on Force. (A) Walking rate of myosin heads in terms of the applied force. (B) Unbinding rate between myosin heads and f-actin in terms of the applied force. 68

Figure 3.3. Velocity correlation and grid size at different radius and grid size, respectively, for various strength of volume-exclusion effects. (A) Velocity correlation found using F-actin within

and ballistic motions ($\sim\tau^2$). Motors with $N_h = 10$ in a high-connectivity network show ballistic movement ($\sim\tau^2$). Motors with $N_h = 4$ in a low-connectivity network exhibit the slope of MSD smaller than 2. More frequent unbinding of motors with lower N_h (i.e. less processive) leads to more hopping or diffusion of motors, thus hindering ballistic motions. In addition, in the low-connectivity network, larger motions of F-actins (Fig. 5.5A) hinder ballistic motions. 141

Figure 5.10. Motions of two-arm motors in networks with different connectivity and different number of motors (N_M). ACP unbinding and F-actin turnover were not considered in these simulations. (A) TE-MSD (time- and ensemble-averaged mean squared displacement) of motors. Gray dashed lines indicate the slope of MSD corresponding to diffusive motions ($\sim\tau^1$) and ballistic motions ($\sim\tau^2$). In a network with low connectivity, higher N_M leads to lower TE-MSD. (B) Average force exerted on each myosin head in motor arms, which corresponds to the ensemble average of time average of forces acting on motor arms, divided by the number of heads represented by each motor arm (N_h). For $N_M > 10$, the average force increases with N_M in a network with low connectivity, resulting in higher average force at $N_M =100$ than that in networks with medium and high connectivity. (C) The fraction of stalling indicating how long motors are stalled during a simulation run up to $t = 1000$ s. Motors are mostly stalled in networks with medium and high connectivity, regardless of N_M. In a network with low connectivity, the fraction of stalling increases at $N_M > 10$, which is consistent with the increase in the average force shown in (B). (D) Visualization of networks at 800 s. Blue, white, and red represent low, intermediate, and high forces, respectively. Only actins and motors bearing high forces (> 25 pN) are visualized. In a network with low connectivity and high N_M, adjacent motors are connected via force-bearing F-actins, indicating force transmission between the motors. 143

Figure 5.11. Motions of two-arm motors in networks with different connectivity and different number of motors (N_M). In these simulations, ACP unbinding and F-actin turnover were not included. (A) τ-MSD and (B) E-MSD of motors. The magnitude of τ-MSD and the slope of E-MSD for a low-connectivity network start decreasing later than those for medium- and high-connectivity networks. The case with $N_M = 100$ and low network connectivity shows much lower values of τ-MSD and E-MSD compared to those with $N_M = 5$ and 30, indicating much slower motor motions resulting from global force transmission as explained in the text. 145

Figure 5.12. Motions of two-arm motors in networks with different connectivity and different number of motors (N_M). In these cases, ACPs are allowed to unbind from F-actins with the reference unbinding rate. F-actin turnover is not considered ($k_{t,A} = 0$). (A) TE-MSD (time- and ensemble-averaged mean squared displacement) of motors. Gray dashed lines indicate the slope of MSD corresponding to diffusive motions ($\sim\tau^1$) and ballistic motions ($\sim\tau^2$). In a network with low connectivity, higher N_M leads to lower TE-MSD after ~5 s. (B) Average force exerted on each myosin head in motor arms, which is the ensemble average of time average of forces acting on motor arms, divided by the number of heads represented by each motor arm (N_h). Motors in networks with medium and high connectivity experience much higher forces. (C) The fraction of stalling indicating how long motors are stalled during a simulation run up to $t = 1000$ s. Motors in networks with higher connectivity are stalled for a longer time, which is consistent with higher forces exerted on motor arms shown in (B). (D) Network heterogeneity quantified using the radial distribution function from positions of actins. Networks with low/medium connectivity high N_M exhibit aggregating behaviors. (E) TE-MSD of motors walking in reconstituted F-actin networks with low motor density. Cross-linking density is 0 (blue) or 0.1 (red). (F) A correlation between

network morphology, we calculate the radial distribution function, $g(r)$, every 10 s. Then, the average value of $g(r)$ at 0.1 µm $< r <$ 1 µm, $\bar{g}(t)$, is calculated for each time point. The maximum value of $\bar{g}(t)$ normalized by its initial value, $\bar{g}_{max} / \bar{g}_{init}$, is used as a measure for network heterogeneity. All of the results shown here imply that F-actin turnover prevents motors from being stalled or confined. 154

Figure 5.17. Effects of F-actin turnover on motions of two-arm motors. (A) Visualization of networks at 800 s under the same condition as that used for Figs. 5.16C, D. An only difference is that F-actins in the center and right cases undergo turnover (i.e. treadmilling). Blue, white, and red represent low, intermediate, and high forces, respectively. Only actins and motors bearing relatively high forces (> 50 pN) are visualized. With faster F-actin turnover, force transmission between motors decreases, resulting in a reduction of global force-induced stalling. (B) Time evolution of network heterogeneity in three cases shown in Figs. 5.16E, F. The averaged value of the radial distribution function was calculated every 10 s. There were 100 motors ($N_M = 100$) in a low-connectivity network, and ACP unbinding was allowed to occur with the reference rate. With $k_{t,A} = 70$ s^{-1}, a network remains relatively homogeneous compared to networks with lower $k_{t,A}$. 155

ABSTRACT

Mechanical forces play a crucial role in cell functions. Cells can generate force, change their shape, and sense external mechanical stimuli, which allows diverse cell functions such as cell migration, cytokinesis, and morphogenesis. Mechanics of cells mainly come from the molecular interactions between actin filaments and diverse actin-binding proteins in the actin cytoskeleton. Actin-crosslinking proteins connect actin filaments to form actin structures; myosin, a molecular motor, generates force on the actin filaments. Due to the complex geometry of the actin structures in non-muscle cells, it has not been well understood how the actin cytoskeleton generates force and remodels itself. To better understand the molecular interactions, many *in vitro* studies employed a minimal system composed of actin filaments, actin-crosslinking proteins, and myosin motors. For example, myosin motility assays have been used to understand the self-organization and collective behavior of actin filaments, which enable the formation of diverse actin structures in cells. Reconstituted actomyosin networks have been used to understand myosin-induced contraction of the cell cortex, which allow cell shape change. A computational model can give additional information that is critical for understanding the mechanics of the cytoskeleton which *in vitro* assay cannot offer, such as the location or force of each molecule. Most of the previous models lack some mechanical details that could potentially be critical in the mechanics of the actin cytoskeleton. In this study, we used an agent-based computational model based on Brownian dynamics for simulating the motility assay and actomyosin network. The model describes the detailed mechanics and dynamics, thus enabling the investigation of previously unexplored aspects of cytoskeleton mechanics.

In the first study, we investigated how the properties of actin filaments and motors affect gliding motions and the self-organization of actin filaments on the motility assay. We found that the length of actin filaments, the average spacing between neighboring motors, and the processivity of motors regulate the gliding speed of actin filaments. We also demonstrated that cross-linking proteins could lead to contractile behaviors of actin networks on the motility assay.

In the second study, we showed that volume-exclusion effects between actin filaments can induce self-organization and collective motion of actin filaments. Bands and ring-like patterns

were formed through self-organization; the patterns could be regulated by bending stiffness of filaments, actin concentration, and actin filament length.

In the third study, we sought to understand an alternative mechanism of contraction of actin networks by myosin motors. Previously, unbinding of cross-linkers and severing of actin-filaments by buckling have been identified as important regulators of actin network contraction. We investigated how F-actin fragmentation by stretching, which has not been studied but could potentially regulate contraction dynamics, contributes to the contraction of actin networks. In *in vitro* experiments, we observed that some actin filaments are indeed fragmented due to tensile forces. Using the computational model, we demonstrated that F-actin fragmentation is particularly important for the contraction of networks composed of long actin filaments with numerous motors, whereas cross-linker unbinding is more important for the contraction of networks with short actin filaments.

In the fourth study, we investigated how actin network remodeling by myosin activity regulates the motions of motors in turn. We demonstrated that myosin motions can be confined due to force generation or force transmission; we identified conditions where each of the two mechanisms is dominant. We also found that turnover of cross-linking proteins can trap motors and verified it in an *in vitro* experiment. On the other hand, turnover of actin filaments was shown to promote motor movement and inhibit confinement.

This study gives new biophysical insights into the self-organization, contraction, and transport in actin networks, which enable a more complete understanding of cellular processes regulated by the dynamics and mechanics of actin networks.

1. INTRODUCTION

1.1   Introduction

Cells' ability to reproduce, grow, move, and secrete hormones is essential for the everyday life of organisms. Almost all cell functions rely on the activity of actin, one of the most abundant protein in cells [1]. Actin forms diverse structures along with actin-binding proteins, which are called the actin cytoskeleton. The actin cytoskeleton has a remarkable ability to self-organize, reorganize, and generate force. This ability enables cellular processes which require dynamic cell shape change, such as migration, morphogenesis, and cell division. In addition, the actin cytoskeleton serves as an intracellular track on which motor proteins can transport cellular cargoes. Thus, understanding the dynamics of the cytoskeleton is crucial for understanding these cell functions.

For understanding the dynamics of the actin cytoskeleton, it is essential to investigate: (1) what molecules are involved in the cellular processes and (2) how these molecules interact with each other to drive the cellular processes. For investigating these two, three types of studies are performed by researchers: *in vivo*, *in vitro*, and computational. *In vivo* studies are essential to determine what molecules are involved in cellular processes. For example, an *in vivo* study found that formin and myosin II are important to form the contractile machinery of the cell cortex [2, 3]. Due to the dense structure of the cell cortex, only a surface of the cortex can be visualized in *in vivo* studies, making it not suitable for observing how molecules interact [4]. *In vitro* reconstituted systems are used to study the interaction between proteins since it has minimal components which can be easily visualized. Computational studies can give further insights on the interaction between proteins by enabling measurement of values that are not measurable in *in vitro* or *in vivo* experiments.

The goal of this research is to use a computational model of the actin cytoskeleton to explore and identify interactions between actin and actin-binding proteins that crucially govern the dynamics of the actin cytoskeleton. This research will give new insights into the understanding of cellular processes governed by the actin cytoskeleton.

1.2   Background

Actin filaments (F-actins) are filamentous protein that are composed of actin monomer, G-actin. G-actin polymerizes into actin filaments. Actin has a polarity, with one end called barbed end and the other end called pointed end. Actin filaments can assemble and disassemble at both ends, with assembly primarily occurs at the barbed end and disassembly primarily occurs at the pointed end. When actin has the same assembly and disassembly rate at the barbed and the pointed ends, respectively, it is called treadmilling, which aids remodeling of the actin cytoskeleton [1].

Numerous actin-binding proteins bind to actin filaments and regulate the mechanics and dynamics of the actin cytoskeleton. Motor protein is one of the important actin-binding proteins. The myosin family, a family of motor proteins ranging from Myosin I to Myosin XVIII is associated with the actin cytoskeleton [5]. Myosin II can walk on the filaments and generate contractile force that drives cell shape change and cell movement [5]. Myosin II is non-processive, meaning that the duty ratio is not big enough for a single motor to stay on filaments and move forward. Myosin II self-assembles into a thick filament, whose length varies depending on the cell type [5]. Unlike myosin II, Myosin V is processive. A single myosin V molecule can transport cellular cargo along F-actins without frequent unbinding [5].

Actin-crosslinking proteins (ACPs, cross-linkers) have two binding sites which can bind to F-actin, thus connecting F-actins pairs. Different kinds of ACPs differ in geometry and mechanical properties, thus leading to distinct actin structures depending on ACP types. α-actinin and small ACPs such as fimbrin, scruin, fascin, or espin tend to form bundles, whereas Arp 2/3 complex and larger ACPs such as filamin form networks [2, 6].

Understanding the interaction between actin-binding proteins and actin filaments is key to understand various cellular processes [2]. In this dissertation, we studied three cellular processes: self-organization of actin networks, contraction of actin networks by myosin, and myosin transport in actin networks.

1.2.1   Self-organization of actin structures

Self-organization is a process by which macroscopic order emerges from local interactions between components in a disordered system. Actin filaments and actin-crosslinking proteins form higher-ordered actin structures, such as cytokinetic rings, cortex, and lamellipodia, through self-

24

organization. What drives the self-organization of actin structures is the dynamics of and interactions between actin filaments and actin-binding proteins. Self-organizing actin structures at the correct time and place is crucial for cellular processes including cell migration and division [7].

An effective and widely used approach to study self-organization is a bottom-up approach: an approach of building a self-organized structure from several components of the structure [8]. *In vitro* motility assay is one of the bottom-up approaches that has been widely used to study self-organization of actin filaments [9]. In motility assay, actin filaments slide on motors that are fixed on the glass surface or lipid bilayer (Fig. 1.1A). It was originally used with low actin density where a single actin filament can be visualized, to measure the mechanochemistry of motors or mechanical properties of actin filaments [10]. More recent research observed that with a high enough density of actin, crowding effects induce collective behavior and self-organization of actins due to repulsive interaction between them [11]. Many diverse structures, including bands, flocks, and swirls, have been observed [9, 12] (Fig. 1.1B, C). When cross-linkers were added, contractile or ring-like structures were formed depending on the cross-linker type [13]. Motility assay is suitable for understanding the interactions among motors, actins filaments, and cross-linkers due to the easiness of visualizing patterns formed by the interactions.
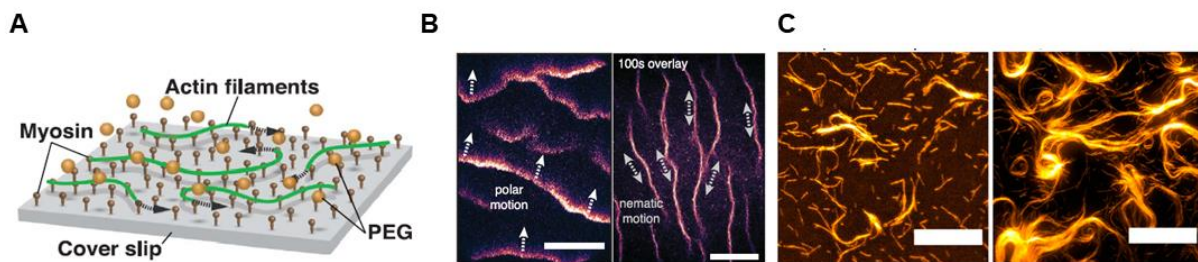
Figure 1.1. Myosin-based motility assay. (A) A schematic diagram showing motility assay. Myosin is fixed on the glass surface, and actin glides on myosin. Polyethylene glycol (PEG) is a crowding agent used to control repulsive interaction between filaments. (B) Formation of actin bands on motility assay on a glass surface. Scale bars, 100 µm. (C) Formation of transient bands (left) and ring-like structures (right) on a lipid bilayer. Scale bars, 20 µm. (A) and (B) are adopted from [9] and (C) is adopted from [12].

Simulation of *in vitro* motility assay is useful in that one can control and measure values that are not measurable in an experiment, such as repulsive interaction between filaments [14], to identify the physical origin of the interactions that leads to self-organization. A computational study found that repulsion between filaments promotes alignment between them, thus forming

structures such as bands and swirls depending on other parameters such as filament concentration [14]. Most computational studies simplified motors into force exerting on filaments, thus not considering unbinding and binding of motors to the filaments [14].

Possible importance of motor binding and unbinding is demonstrated by a microtubule motility assay. Studies have shown that dynein aligns microtubules, whereas kinesin cannot unless a crowding agent is added [15, 16]. With kinesin being processive (i.e. high duty ratio) and dynein non-processive, it was suggested that frequent unbinding and binding of dynein reorient the filaments [15, 16]. Thus, there is a need to use a computational model that explicitly describes motor unbinding and binding, which could offer additional information on the interaction between actin filaments and binding proteins during self-organization.

1.2.2   Contraction of actin structures

A cell dynamically changes its shape, and it is attributed to the force generation by myosin in the cell cortex, a thin actin network located underneath and adhere to the plasma membrane. Myosin II generates a tension gradient in the cell cortex due to the heterogeneity of the cortical architecture and myosin concentration within the cortex [4]. The gradient of tension induces contraction or rupture of the cell cortex [17] (Fig. 1.2). Such morphological change in the cell cortex drives diverse cell functions. Cell shape change driven by cortex rupture drives the amoeboid migration of cells [18]. During morphogenesis, contraction of the cell cortex induces cell intercalation and axis elongation, leading to tissue formation [19]. Moreover, cortex rupture was shown to drive angiogenesis [20].
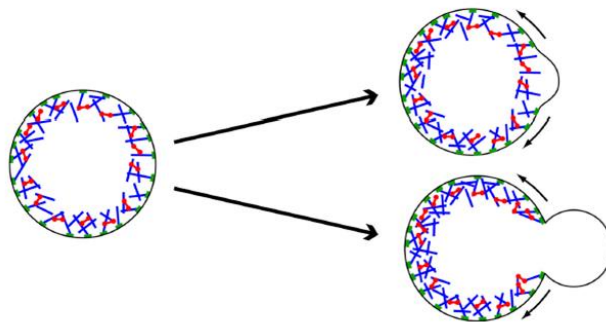
Figure 1.2. Rupture of cortex due to tension gradient generated by myosin. Cortical rupture can further induce blebbing of cells. Blue rods: actin filaments, red dumbbells: myosin, green dots: membrane adhesion. Adopted from [17].

Until recently, studying cortex contraction *in vivo* was difficult due to spatiotemporal limitation in imaging [21]. Thus, *in vitro* studies have been widely used to understand myosin-induced contraction of the actin networks (Fig. 1.3). Researchers found, in both *in vitro* and *in vivo*, that initial connectivity of actin networks, determined by actin filament length and cross-linker density, governs network contraction and tension generation [22, 23]. For contraction of an initially well-connected network, decreasing connectivity of the network is pivotal [24]. An *in vitro* study showed that myosin motors contract a crosslinked actin network into multiple clusters due to unbinding events of cross-linkers [24]. Actin filaments fragmentation by buckling has been identified to induce contraction of networks in both *in vitro* and computational studies [25-27]. Although there are two mechanisms by which filaments can be severed – buckling and stretching – no current *in vitro* or computational research addresses the latter. It was suggested that if one part of filaments is buckled, there is a part of filaments that is stretched [25]. Thus, to better understand cortical contraction, it is necessary to investigate how filament stretching affects the contraction of the actomyosin network.
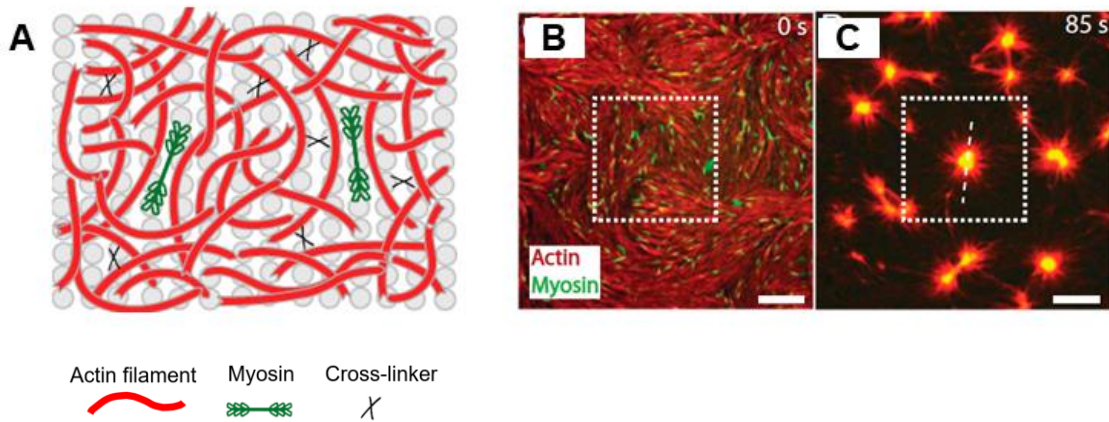
Figure 1.3. Contraction of *in vitro* actomyosin network due to myosin activity. (A) Schematic of a reconstituted actomyosin on lipid bilayer. (B) Initially homogeneous network contracts into (C) clusters due to myosin activity. Adapted from [25].

1.2.3 Transport along actin structures

Cellular cargoes, such as synthesized proteins, are transported within cells to the place where they are needed, which is called intracellular transport. Intracellular transport plays a pivotal role in organism functions, by allowing the delivery of proteins to organelles and secretion of hormones and neurotransmitters. Microtubules and actin filaments are involved in intracellular

transport. Kinesin and dynein transport cargoes on microtubules, whereas myosin V transport cargoes on the actin filaments in the cell cortex (Fig. 1.4). Transport inside the cell cortex has been suggested as an important step for secretion [28].
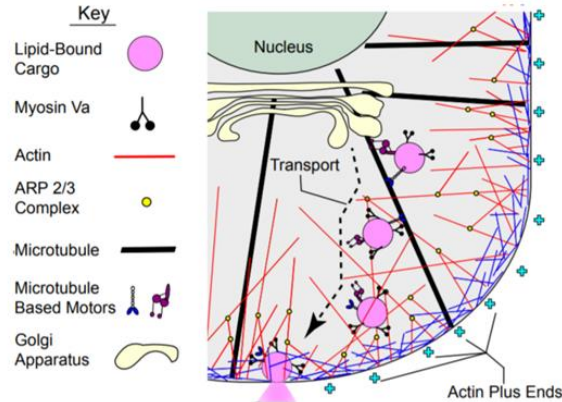
Figure 1.4. Schematic diagram of intracellular transport. Cellular cargoes are transported along microtubules and within actin network by molecular motors. Adopted from [29].

Due to the complex and dense structure of the cell cortex, it is not trivial to understand how transport is regulated in the cell cortex. One useful approach is single-particle tracking. From single-particle tracking, researchers can retrieve the trajectory of individual cargo from which they can infer interaction between cargo and environment [30]. For example, the slope (α) of the mean squared displacement (MSD) calculated from the trajectory shows if the cargo motion is subdiffusive ($\alpha<1$) or superdiffusive ($1<\alpha<2$). It was shown that subdiffusive motion indicates cargoes are trapped in the cytoskeleton [29], whereas superdiffusive motion indicates directed motion by molecular motors [31]. On microtubules, cargoes exhibited directed motion, whereas they showed subdiffusive behaviors on actin structures [32, 33].

Subdiffusive motion of cargoes in the actin cortex can be attributed to myosin V, which can bind to multiple filaments at once, termed tug-of-war [29]. Indeed, it was shown that unlike in bundles and networks with filaments of similar polarity, cargo motion was inhibited in bundles and isotropic networks where filaments have mixed polarity [29, 34]. There is a possibility that tug-of-war can remodel actin networks by force generation. In addition, myosin II can remodel the actin network due to its contractile activity. It is not clear how the remodeling of the actin network by myosin affects in turn the myosin-based transport.

If we understand how myosin transport is regulated by remodeling, it will enable ways to regulate remodeling and transport in situations where inefficient transport becomes a problem [35]. We sought to understand how feedback between cargo transport and cell cortex remodeling regulate the transport efficiency of cargoes.

1.3   Significance of the study

Cells are highly mechanical; they can generate force, remodel themselves, and sense mechanical stimuli. Mechanical behavior of cells come from the mechanics of the actin cytoskeleton [36], which is governed by the complex interplay of myosin, actin-crosslinking proteins, and actin filaments. Mutations in myosin and actin-crosslinking proteins have been associated with many types of diseases [19, 37-39]. There have been many studies on understanding the machinery of the actin cytoskeleton [4, 8]. While *in vivo* experiments are crucial for understanding how the cytoskeleton regulates whole cell behavior, they are not suitable for measuring mechanical parameters of individual proteins or interaction between them inside the cytoskeleton. *In vitro* experiments [8] and single-molecule experiments [40, 41] are more suitable for measuring mechanical parameters and observing interactions between proteins. A computational model can serve as a useful tool to predict cytoskeleton behavior when calibrated by data from *in vitro* or single-molecule studies. However, many computational models simplify important mechanical parameters or response that would crucially affect predicted cytoskeleton behavior [14, 42]. We bridge the gap by using a computational model that incorporates mechanics, dynamics, and geometry of the cytoskeleton in detail to unravel interactions that have not been identified in previous studies. Thus, this research contributes to a more complete understanding of the cellular processes that rely on the mechanical and dynamical aspects of the actin cytoskeleton.

1.4   Dissertation objectives

To understand cellular processes governed by the actin cytoskeleton, we investigate how proteins interact during the morphological change of the actin network and how the remodeling of actin networks governs the transport of motors. The following specific aims will be addressed:

1. To understand how actin filaments self-organize into diverse structures in myosin-based motility assay

2. To understand how force generation by myosin governs contraction and fracture of cortex-like actin networks

3. To understand how remodeling of cortex-like actin networks governs transport by myosin

1.5   Methods

In this dissertation, we use an agent-based model that faithfully incorporates dynamics and mechanics of actin filaments and actin-binding proteins which are modeled as elastic cylindrical segments with extension and bending stiffness [43]. The position of each segment is updated by the Langevin equation. Dynamic events such as actin treadmilling, actin severing, cross-linker unbinding, and motor walking were incorporated. Details of the model and parameter values are included in each chapter of the dissertation.

1.6   Organization of the dissertation

This dissertation is composed of four studies. In the first study (Chapter 2), parameters in motility assay that are important for gliding speed and self-organization of actin filaments were identified. In the second study (Chapter 3), self-organization of actin structures in the motility assay depending on repulsive force, bending stiffness of actin, actin concentration, and filament length was investigated. We identified parameter values that lead to different patterns formed by actin filaments, including flocks, bands, and swirls. In the third study (Chapter 4), we evaluated the effects of filament stretching in the contraction of the actomyosin network. In the fourth study (Chapter 5), we investigated the effects of actin network remodeling on myosin-based transport in cortex-like networks. We identified three mechanisms by which motors can be trapped.

2. COLLECTIVE AND CONTRACTILE FILAMENT MOTIONS IN THE MYOSIN MOTILITY ASSAY

The work described in this chapter has been published in [44].

2.1 Introduction

The actin cytoskeleton within animal cells is responsible for a variety of functions. Interactions between F-actin, actin cross-linking protein (ACP), and molecular motors within the cytoskeleton generate mechanical forces that regulate physiological functions, such as cell migration, cytokinesis, wound healing, and morphogenesis [45, 46]. It is known that F-actins in cells carry tensile forces that are generated due to myosin motor proteins interacting with the F-actins. Dimers of myosin II assemble themselves into thick filaments. These thick filaments then walk toward the barbed end of the F-actin by using their motor heads [47]. This walking is often explained by the cross-bridge cycle with multiple states[48]. The transitions between these states are described by their mechanochemical rates[48].

In vitro myosin motility assays have been used in the past to better study the interactions between F-actin and myosins. In these motility assays, F-actins move along a surface covered with immobilized myosin motor heads [11, 49]. When F-actin density is high in the presence of strong crowding effects, ordered motions of F-actins were observed. This is attributed to severe volume-exclusion effects between F-actins [50-54]. Above critical F-actin density, F-actins moved together as clusters, interconnected bands, and swirls. When ACPs were present, these motions became more or less collective [13, 55, 56]. For example, inclusion of fascin in the motility assay resulted in formation of rings, elongated fibers, and polar structures depending on conditions. However, α-actinin led to contractile patches, and filamin A induced formation of a more stable network. Other ACPs, such as α-EPLIN, cortexillin, and anillin, also induced formation of unique structures. Some of these studies suggested hypotheses about how interactions between F-actin, ACP, and myosin motors facilitate collective motions at both filament and network levels.

To provide more insights into understanding of microscopic origins, myosin motility assays have been also studied via computational and theoretical models. One study employed a stochastic model to show how twirling motions of F-actins are caused by myosin motors [57]. An

agent-based model based on Brownian dynamics was developed to determine an expression that can accurately predict how long gliding F-actins remain bound to myosin motors before dissociation [58]. Another model based on Brownian dynamics modeled F-actins as worm-like chains and cross-linkers and motors as springs with force-dependent kinetics [59]. This model demonstrated that the persistency and velocity of a gliding filament increase as a larger number of motors are bound to the filament due to an increase in either motor density, motor duty ratio, or filament length. In addition, a bead-rod model was employed to simulate single F-actin interacting with stationary motors simplified by springs [60]. This model demonstrated that higher ATP concentration leads to faster F-actin movement, whereas a change in motor density does not affect F-actin speed. Also, this study demonstrated that the gliding motion can be guided by chemical cues at probability directly affected by processivity of myosin motors. However, most of the previous models had limitations. For example, to reduce computational costs, the mechanics of F-actin was drastically simplified, or motors were considered implicitly by directly applying propelling forces to F-actin. In studies with explicit consideration of motors, gliding motion of only one F-actin was simulated, or mechanochemical cycles of myosin were not incorporated in a rigorous manner. Due to these critical limitations, it is difficult to rigorously investigate collective and contractile behaviors of multiple F-actins or how they emerge from molecular interactions between motors and F-actins.

To overcome these hurdles, we employed a well-established agent-based computational model based on Brownian dynamics with the Langevin equation [61, 62]. First, we ran simulations in the absence of ACPs and volume-exclusion effects between F-actins to focus on pure gliding motions of individual F-actins as a base study. We evaluated effects of a variation in the average length of F-actin and the density and mechanochemical rate of motors. Then, we investigated influences of volume-exclusion effects between F-actins on behaviors of F-actins by varying the strength of volume-exclusion effects acting between neighboring F-actins. Lastly, we added ACPs with a wide range of density and unbinding rates to identify the effects of ACPs on contractile behaviors of F-actins in the motility assay.

2.2 Methods

2.2.1 Model overview

We used an agent-based computational model based on Brownian dynamics, as in our previous studies [27, 61-63]. F-actin, ACP, and motor are coarse-grained by cylindrical segments (Fig. 2.1A). F-actin is simplified by cylindrical segments of 140 nm in length with polarity (i.e. barbed and pointed ends) serially connected by elastic hinges. Note that the length of the actin cylindrical segment is determined with consideration of both computational efficiency and realistic description of bending deformation of F-actins as in our previous studies [61, 63, 64]. Each ACP consists of two arms connected at its center point by elastic hinges. In this chapter, one-arm motor, which can bind to only one F-actin was used. All parameter values are listed in Tables 2.1 and 2.2. Most of the parameter values are inherited from our previous models that successfully recapitulated various mechanical and dynamic behaviors of actin networks [27, 61-63].

2.2.2 Brownian dynamics via the Langevin equation

Displacement of each cylindrical segment constituting actin, motor, and ACP is governed by the Langevin equation with inertia neglected:

$$\mathbf{F}_i - \zeta_i \frac{d\mathbf{r}_i}{dt} + \mathbf{F}_i^{\mathrm{T}} = 0 \tag{2.1}$$

where $\mathbf{F}_i$ is a net deterministic force, ζ_i is a drag coefficient, $\mathbf{r}_i$ is a position, t is time, and $\mathbf{F}_i^{\mathrm{T}}$ is a stochastic force satisfying the fluctuation-dissipation theorem [65]:

$$\left\langle \mathbf{F}_i^{\mathrm{T}}(t)\mathbf{F}_j^{\mathrm{T}}(t) \right\rangle = \frac{2k_{\mathrm{B}}T\zeta_i\delta_{ij}}{\Delta t}\boldsymbol{\delta} \tag{2.2}$$

where δ_{ij} is the Kronecker delta, $\Delta t = 1.5\times10^{-5}$ s is a time step, and $\boldsymbol{\delta}$ is a unit second-order tensor. ζ_i is calculated by the approximate equation for a cylindrical object [66]:

$$\zeta_i = 3\pi\mu r_{c,i} \frac{3 + 2r_{0,i}/r_{c,i}}{5} \tag{2.3}$$

33

where μ is viscosity of the medium, and $r_{c,i}$ and $r_{0,i}$ are the diameter and length of a segment, respectively. At each time step, position of each segment is updated using the Euler integration scheme:

$$\mathbf{r}_i(t+\Delta t) = \mathbf{r}_i(t) + \frac{d\mathbf{r}_i}{dt}\Delta t = \mathbf{r}_i(t) + \frac{1}{\zeta_i}\left(\mathbf{F}_i + \mathbf{F}_i^{\mathrm{T}}\right)\Delta t \tag{2.4}$$

2.2.3 Deterministic forces

The deterministic force, $\mathbf{F}_i$, includes extensional, bending, and repulsive forces. Extensional and bending forces involved with F-actin, ACP, and motor are calculated based on harmonic potentials:

$$U_{\mathrm{s}} = \frac{1}{2}\kappa_{\mathrm{s}}(r-r_0)^2 , \; U_{\mathrm{b}} = \frac{1}{2}\kappa_{\mathrm{b}}\left(\theta-\theta_0\right)^2 \tag{2.5}$$

where κ_{s} and κ_{b} are extensional and bending stiffness, respectively, r is length of a segment, θ is an angle formed by segments, and the subscript 0 represents an equilibrium value. Extensional ($\kappa_{\mathrm{s,A}}$) and bending stiffness ($\kappa_{\mathrm{b,A}}$) of F-actin maintain the length of each actin segment at an equilibrium length ($r_{0,\mathrm{A}}$) and an angle between adjacent actin segments at an equilibrium angle ($\theta_{0,\mathrm{A}}$), respectively. Similarly, extensional ($\kappa_{\mathrm{s,ACP}}$) and bending stiffness ($\kappa_{\mathrm{b,ACP}}$) of ACPs maintain the length of each ACP arm and an angle formed by two ACP arms at their equilibrium values ($r_{0,\mathrm{ACP}}$ and $\theta_{0,\mathrm{ACP}}$), respectively. Extensional stiffness of motors ($\kappa_{\mathrm{s,M}}$) maintains an equilibrium length of the motor arm ($r_{0,\mathrm{M}}$). Forces exerted on binding sites of an actin segment by motors and ACPs are distributed to two end points of the segment as explained in our previous work [61].

Repulsive forces between actin segments located closely are calculated based on the harmonic potential:

$$U_{\mathrm{r}} = \begin{cases} \dfrac{1}{2}\kappa_{\mathrm{r}}\left(r_{12}-r_{\mathrm{c,A}}\right)^2 & \text{if} \quad r_{12} < r_{\mathrm{c,A}} \\ 0 & \text{if} \quad r_{12} \geq r_{\mathrm{c,A}} \end{cases} \tag{2.6}$$

where r_{12} is a minimum distance between a pair of actin segments, and κ_r is strength of the repulsive force.

2.2.4 Dynamics of F-actin

Formation of F-actin is initiated by appearance of one cylindrical segment occurring at a given nucleation rate ($k_{n,A}$). The segment is quickly elongated into a filament by addition of cylindrical segments to the barbed end at a given assembly rate ($k_{+,A}$). Depolymerization of F-actin is simulated by removal of cylindrical segments from the pointed end at a given disassembly rate ($k_{-,A}$). In cases without F-actin turnover, $k_{-,A}$ is zero, so F-actins do not undergo any dynamic event after all actin segments are consumed for formation of F-actins. By contrast, in cases with F-actin turnover, $k_{-,A}$ is equal to $k_{+,A}$, leading to treadmilling with a balance between polymerization at the barbed end and depolymerization at the pointed end. Thus, the average length of F-actin does not change over time after the number of free actin segments reaches a steady state. An actin turnover rate, $k_{t,A}$ ($= k_{-,A} = k_{+,A}$), indicates how fast the treadmilling takes place.

2.2.5 Dynamic behaviors of ACPs

ACPs bind to binding sites located on actin segments without preference of a contact angle. We modeled both permanent and transient ACPs. Permanent ACPs do not unbind after binding to F-actins, which mimic kinetic behaviors of ACPs like scruin [36]. Transient ACPs can unbind from F-actins in a force-dependent manner, following Bell's law [67]:

$$k_{u,ACP} = \begin{cases} k_{u,ACP}^0 \exp\left(\dfrac{\lambda_{u,ACP}\left|\vec{F}_{s,ACP}\right|}{k_B T} \right) & \text{if } r \geq r_{0,ACP} \\ k_{u,ACP}^0 & \text{if } r < r_{0,ACP} \end{cases} \tag{2.7}$$

where $k_{u,ACP}^0$ is a zero-force unbinding rate constant, $\lambda_{u,ACP}$ represents sensitivity to the magnitude of applied spring force ($\left|\vec{F}_{s,ACP}\right|$), and $k_B T$ is thermal energy. Note that we employed a positive value for $\lambda_{u,ACP}$ to mimic the response of a slip bond, so $k_{u,ACP}$ exponentially increases with a

higher applied force. The reference values of $k_{u,ACP}^0$ and $\lambda_{u,ACP}$ are determined based on those of filamin A [68].

Table 2.1. List of parameters employed in the model.

Symbol	Definition	Value
$r_{0,A}$	Length of an actin segment	1.4×10^{-7} [m]
$r_{c,A}$	Diameter of an actin segment	7.0×10^{-9} [m][69]
$\theta_{0,A}$	Bending angle formed by adjacent actin segments	0 [rad]
$\kappa_{s,A}$	Extensional stiffness of F-actin	1.69×10^{-2} [N/m]
$\kappa_{b,A}^*$	Reference bending stiffness of F-actin	2.64×10^{-19} [N·m][70]
$r_{0,ACP}$	Length of an ACP arm	2.35×10^{-8} [m][71]
$r_{c,ACP}$	Diameter of an ACP arm	1.0×10^{-8} [m]
$\theta_{0,ACP}$	Bending angle formed by two ACP arms	0 [rad]
$\kappa_{s,ACP}$	Extensional stiffness of ACP	2.0×10^{-3} [N/m]
$\kappa_{b,ACP}$	Bending stiffness of ACP	1.04×10^{-19} [N·m]
$r_{0,M}$	Length of a motor arm	1.35×10^{-8} [m]
$r_{c,M}$	Diameter of a motor arm	1.0×10^{-8} [m]
$\kappa_{s,M}$	Extensional stiffness of a motor arm	1.0×10^{-3} [N/m]
k_{20}^*	Reference ATP-dependent unbinding rate of myosin heads	20 [s^{-1}]
N_h	Number of heads represented by a motor arm	8
N_a	Number of arms in a motor	1
$k_{n,A}$	Nucleation rate of actin	$0.000125 - 1$ [μM^{-1}s^{-1}]
$k_{+,A}$	Polymerization rate of actin at the barbed end	60 [μM^{-1}s^{-1}]
$k_{u,ACP}^{0*}$	Reference zero-force unbinding rate constant of ACP	0.115 [s^{-1}][68]
$\lambda_{u,ACP}$	Sensitivity of ACP unbinding to an applied force	1.04×10^{-10} [m]
$\kappa_{r,A}^*$	Reference strength of a repulsive force	1.69×10^{-3} [N/m]
Δt	Time step	1.15×10^{-5} [s]
μ	Viscosity of surrounding medium	8.6×10^{-1} [kg/m·s]
$k_B T$	Thermal energy	4.142×10^{-21} [J]
C_A	Actin concentration	$15 - 240$ [μM]
R_M	Motor density (= Ratio of motor concentration to C_A)	$0.008 - 0.8$
R_{ACP}	ACP density (= Ratio of ACP concentration to C_A)	$0 - 0.1$
$<L_f>$	Average length of F-actins	$0.62 - 5.06$ [μm]

Table 2.2. List of parameter values used for adopting "parallel cluster model." [72, 73]

Symbol	Definition	Value
k_{01}	A rate from unbound to weakly bound state	40 [s^{-1}]
k_{10}	A rate from weakly bound to unbound state	2 [s^{-1}]
k_{12}	A rate from weakly bound to post-power-stroke state	1000 [s^{-1}]
k_{21}	A rate from post-power-stroke to weakly bound state	1000 [s^{-1}]
k_{20}	A rate from post-power-stroke to unbound state	5-640 [s^{-1}]
F_0	Constant for force dependence	5.04×10^{-12} [N]
E_{pp}	Free energy bias toward the post-power-stroke state	-60×10^{-21} [J]
E_{ext}	External energy contribution	0 [J]
d	Step size	7×10^{-9} [m]
k_m	Spring constant of the neck linkers	1.0×10^{-3} [N/m] ($= \kappa_{s,M}$)

2.2.6 Dynamic behaviors of motors

In this model, it is assumed that a motor arm represents cooperative behaviors of a small number of myosin heads in terms of kinetic behaviors. To avoid confusion, we name it one-arm motors rather than one-headed motors. Each motor arm can bind only to one binding site on actin segments at a rate of $40 N_h$ s^{-1}, where N_h is the number of myosin heads represented by each motor arm. We assume $N_h = 8$, resulting in slightly more processive motors and higher stall forces, as opposed to one myosin head in general. Walking ($k_{w,M}$) and unbinding rates ($k_{u,M}$) of the motor arms are determined by the parallel cluster model (PCM) to reflect the mechanochemical cycle of myosin motors [72, 73]. In the PCM, three mechanochemical states are defined, and there are five mechanochemical rates between the states (Table 2.2). Details of implementation and benchmarking of the PCM in our model were explained in detail in our previous study [61]. We vary one of the mechanochemical rates, ATP-dependent unbinding rate of myosin heads (k_{20}), to probe its influences. $k_{w,M}$ and $k_{u,M}$ generated by PCM are proportional to k_{20} and lower with higher applied force, regardless of k_{20}, which corresponds to the catch-bond behavior of myosin motors. The stall force is inversely proportional to k_{20}. Although we used the value of N_h higher than 1, the ranges of $k_{w,M}$, $k_{u,M}$, and stall force explored in this study enable us to account for more or less processive motors. With the reference value of $k_{20} = 20$ s^{-1}, the unloaded walking velocity of motors is 140 nm/s. This value is similar to the walking velocity of non-muscle myosin II [74, 75], whereas

37

it is ~2 μm/s with the highest value of k_{20} used in this study, which is larger than the walking velocity of smooth muscle myosin II [74, 76].

2.2.7 Initial simulation setup

We used a thin computational domain (10×10×0.1 μm) with a periodic boundary condition in the x and y directions (Fig. 2.1). F-actins are formed by the self-assembly of actin segments located at the same z position. ACPs are included only in a portion of the simulations. ACPs bind to F-actin to form functional cross-links between pairs of F-actins. Motors are distributed at random x and y coordinates at the same z position. A difference between z positions of F-actins and motors corresponds to the equilibrium length of motor arms (= 13.5 nm). Therefore, binding of a motor arm to F-actin is possible if they are located at similar x and y coordinates. While F-actins are assembled, a fraction of the motor arms binds to F-actin with no walking motion. After all F-actins are assembled, motors start walking toward the barbed ends of F-actins.
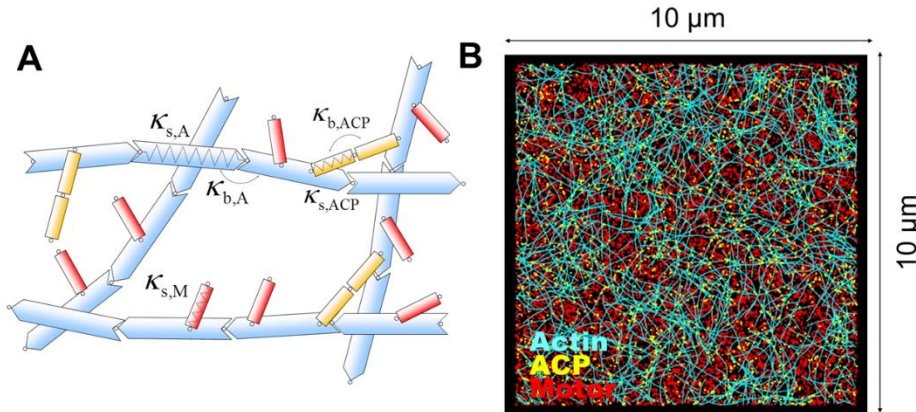
Figure 2.1. Agent-based computational model used for simulations in this study. (A) A schematic diagram showing a network consisting of F-actin (cyan), actin cross-linking protein (ACP, yellow), and motor (red). Each element is simplified by cylindrical segments. Bending (κ_b) and extensional stiffnesses (κ_s) maintain equilibrium angles formed by adjacent cylindrical segments (indicated by bent arrows) and equilibrium lengths of cylindrical segments (indicated by springs), respectively. (B) An example of networks formed by self-assembly of the three elements in a very thin computational domain (10×10×0.1 μm) with a periodic boundary condition in x and y directions.

2.2.8 Quantification of F-actin motions

Velocities of endpoints of all actin segments, $\mathbf{v}_{i,A}(t)$, are calculated every two seconds. We quantified the distribution of $|\mathbf{v}_{i,A}|$ measured at all time points to show speed distribution of all F-actins. To evaluate how fast F-actins are displaced by motors on average, the average speed of F-actins for each simulation is obtained by averaging $|\mathbf{v}_{i,A}|$ over all endpoints and all time points.

In addition, persistency of motions of F-actins is evaluated by calculating the average of autocorrelation of velocity vectors:

$$\langle\cos\phi(\tau)\rangle = \left\langle \frac{2}{T-\tau} \sum_{t=0}^{(T-\tau)/2} \frac{\mathbf{v}_{i,A}(2t)\cdot\mathbf{v}_{i,A}(2t+\tau)}{\left|\mathbf{v}_{i,A}(2t)\right|\left|\mathbf{v}_{i,A}(2t+\tau)\right|}\right\rangle \tag{2.8}$$

where T is the duration of simulations, and τ is time lag. If F-actins hardly change a direction during displacement for τ, $\langle\cos\phi(\tau)\rangle$ is close to 1. In cases with F-actins propelled only by motors, $\langle\cos\phi(\tau)\rangle$ exponentially decays.

We also evaluated the extent of collective motions by measuring a correlation between velocities of endpoints located on neighboring F-actins. As shown in previous studies, F-actins can exhibit collective motions by aligning with each other if there is a volume-exclusion effect between neighboring F-actins. During such collective motions, F-actins tend to move in a parallel or anti-parallel manner to avoid frequent collisions. For this calculation, we identify all pairs of endpoints on F-actins located at a distance between r and $r + \Delta r$ and then calculate the average of correlations between velocities of all pairs:

$$\langle\cos\alpha(r,t)\rangle = \left\langle \frac{\mathbf{v}_{i,A}(t)\cdot\mathbf{v}_{j,A}(t)}{\left|\mathbf{v}_{i,A}(t)\right|\left|\mathbf{v}_{j,A}(t)\right|}\right\rangle \tag{2.9}$$

where α is an angle between two velocity vectors, and the pair of endpoints i and j satisfies $r \leq \left|\mathbf{r}_{i,A}(t)-\mathbf{r}_{j,A}(t)\right| < r+\Delta r$, and they should not belong to the same F-actin. This calculation is performed for different r and t to measure the extent of collective motions of F-actins as a function of distance and time. Then, we calculated the time-averaged value of $\langle\cos\alpha(r,t)\rangle$ to plot

$\langle \cos \alpha(r) \rangle$. To account for collective motions which emerge later in simulations, the time-averaging was done for last 50 s. We set Δr to 0.2 μm, and a maximum distance that we considered for the calculation is 1 μm.

2.2.9   Quantification of F-actin curvature

Persistence length of F-actin can be calculated directly using the following relationship:

$$l_{\mathrm{p}} = \frac{\kappa_{\mathrm{b,A}} r_{0,\mathrm{A}}}{k_{\mathrm{B}} T} \qquad (2.10)$$

where $\kappa_{\mathrm{b,A}}$ is the bending stiffness of F-actin in N·m. However, F-actins interacting with motors can have a curvature leading to a different persistence length. We evaluated the actual curvature of F-actin by measuring a correlation between unit tangential vectors along the contour of F-actin, u(s):

$$\langle \cos \theta \rangle = \langle \mathbf{u}(s) \cdot \mathbf{u}(s + \Delta s) \rangle \qquad (2.11)$$

where s is a position along the contour of F-actin, and Δs is a distance between two positions where the correlation is calculated. This measurement is often used for evaluating the persistence length of polymers. $\langle \cos \theta \rangle$ is plotted as a function of Δs to evaluate the curvature of F-actins. A faster decrease in $\langle \cos \theta \rangle$ is indicative of F-actins with a higher curvature.

2.2.10 Evaluation of network morphology

We evaluated heterogeneity of network morphology by measuring spatial distribution of F-actins. For the measurement, the computational domain is divided into $N_{\mathrm{G}} \times N_{\mathrm{G}}$ grids in the x and y directions, where N_{G} represents the number of grids in each direction. Each grid has its own coordinate, (i, j). We measured the number of actin segments located in each grid, $\rho_{\mathrm{A}}^{i,j}$. Then, the standard deviation of $\rho_{\mathrm{A}}^{i,j}$ is calculated over grids with constant i or j (i.e. in x or y direction). By averaging all the standard deviations, heterogeneity of F-actin, Q_{A}, is calculated like the following:

$$Q_{\mathrm{A}} = \frac{1}{2N_{\mathrm{G}}} \left[\sum_{i=1}^{N_{\mathrm{G}}} \mathrm{std}\left(\rho_{\mathrm{A}}^{i,j} \Big|_{j=1..N} \right) + \sum_{j=1}^{N_{\mathrm{G}}} \mathrm{std}\left(\rho_{\mathrm{A}}^{i,j} \Big|_{i=1..N} \right) \right] \qquad (2.12)$$

Since the heterogeneity calculated in this method depends on the choice of N_{G}, we carefully determined the optimal value of N_{G} at 20. We also calculated the time-average of Q_{A} for last 50 s to account for network morphology at later times.

In addition, using 30×30 grids, we evaluated how network morphology evolves over time in each simulation. We calculated a correlation between $\rho_{\mathrm{A}}^{i,j}$ in grids at the end of a simulation and $\rho_{\mathrm{A}}^{i,j}$ in grids at each time point. If network morphology quickly reaches a steady state and does not vary significantly at later times, the correlation also increases fast and then remains near 1 till the end. If network morphology keeps changing over time, the correlation increases gradually. To quantify how dynamically a network changes its morphology, we calculated duration which the correlation is larger than 0.5. Larger duration indicates more static or "frozen" network morphology.

2.2.11 Analysis of forces on F-actins and motors

We calculated the average of spring forces acting on all chains of F-actins at each time point. It has been shown previously that motor activities induce tensile forces on F-actins because the compressive forces are relaxed due to buckling. Thus, dominance of tensile forces on F-actins can be an indicator for contractile (i.e. tensile) stress on networks. To show a correlation between local stress and network morphology, we calculated the distribution of spring energy density in a network at the end of a simulation. We divided a computational domain into 30×30 grids in the x and y directions. In each grid, we calculated the sum of spring energy of all actin segments and divided the sum by the volume of each grid to obtain spring energy density of each grid in J/m^3. Since most of the F-actins are subjected to tensile forces, the contribution from F-actins under compression to spring energy is negligible. The distribution of spring energy density is visualized using heat maps with color scaling.

In addition, forces exerted by motor arms that are interacting with F-actins were monitored. The average of the forces was calculated over time to estimate how much force motors generated at each time point on average.

2.2.12 Volume-exclusion effects between F-actins

Repulsive force between F-actins depends on the distance between actin segments and represented by a harmonic potential:

$$U_r = \begin{cases} \dfrac{1}{2}\kappa_{r,A}\left(r_{12} - r_{c,A}\right)^2 & \text{if} \quad r_{12} < r_{c,A} \\ 0 & \text{if} \quad r_{12} \geq r_{c,A} \end{cases} \tag{2.13}$$

where $\kappa_{r,A}$ is strength of the repulsive force, r_{12} is a minimum distance between two actin segments, and $r_{c,A}$ is the diameter of an actin segment.

2.3   Results

2.3.1   Effects of properties of F-actin and motor

Before investigating roles of volume-exclusion effects and ACPs, it is necessary to determine more basic properties of F-actin and motor. Thus, we tested effects of three parameters in the absence of ACPs (i.e. zero ACP density, $R_{ACP} = 0$) and volume-exclusion effects ($\kappa_{r,A} = 0$): average length of F-actin ($<L_f>$), motor density (R_M), and ATP-dependent unbinding rate of motors (k_{20}). Note that without ACPs and volume-exclusion effects, F-actins move independently without physical interactions with other F-actins. For a reference condition, $<L_f>$ is ~1.5 μm, R_M is 0.8, and k_{20} is 20 s^{-1}. Under the reference condition, F-actins move relatively fast and quite persistently as observations in the myosin motility assay experiments. We varied one of the three parameters with others fixed in order to evaluate the influences of each parameter.

First, we changed R_M between 0.008 and 0.8. Note that it is hard to evaluate the dependence of F-actin behaviors on R_M if models consider motors in an implicit manner. With fewer motors, F-actins move slower and change their directions more often (Figs. 2.2 and 2.3). If motors are sparsely distributed in space, it is much harder for F-actins to maintain connection to motors. Therefore, there are a larger portion of F-actins diffusing without connection to any motor and F-actins bound to only one motor at lower R_M, resulting in much lower speed and persistency (Fig. 2.2). In addition, with fewer motors, a correlation between unit tangential vectors measured along the contour of F-actins deviates more from that corresponding to their persistence length because F-actins may need to bend more to bind to sparsely distributed motors (Fig. 2.3B). Spatial distribution of F-actins is homogeneous regardless of R_M (Figs. 2.3C-D).
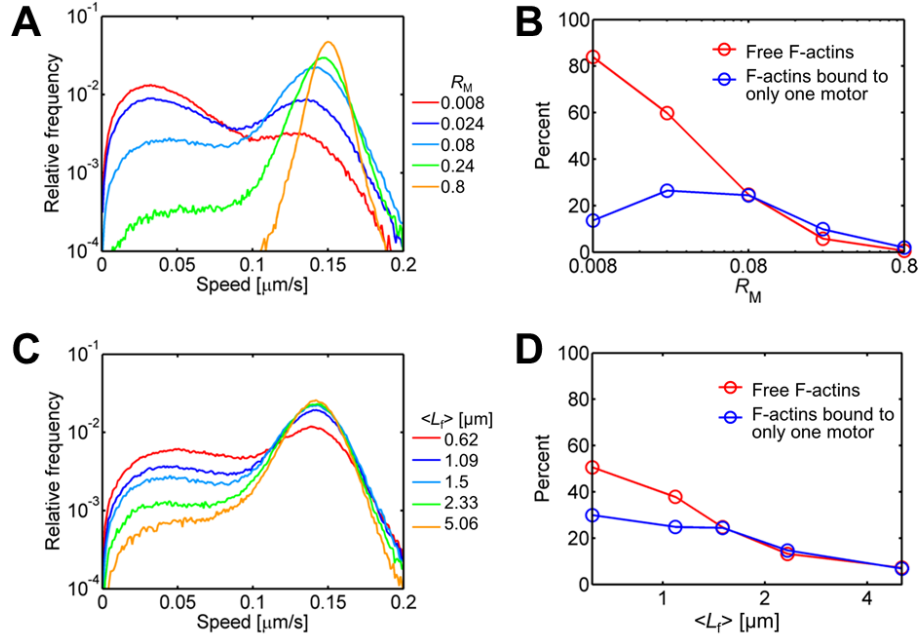
Figure 2.2. Motor density (R_M) and average length of F-actins ($<L_f>$) affect the gliding speed of F-actins. (A, C) Distribution of speed of F-actins. (B, D) Fraction of F-actins that are bound to only one motor or not bound to any motor. In these cases, volume-exclusion effects between F-actins were not incorporated. With smaller R_M or $<L_f>$, speed of F-actin tends to be lower due to a larger number of free F-actins and F-actins bound to only one motor. If F-actins are long enough compared to average spacing between adjacent motors determined by R_M, most F-actins can keep moving at speed close to the unloaded walking speed of motors (~0.14 µm/s).
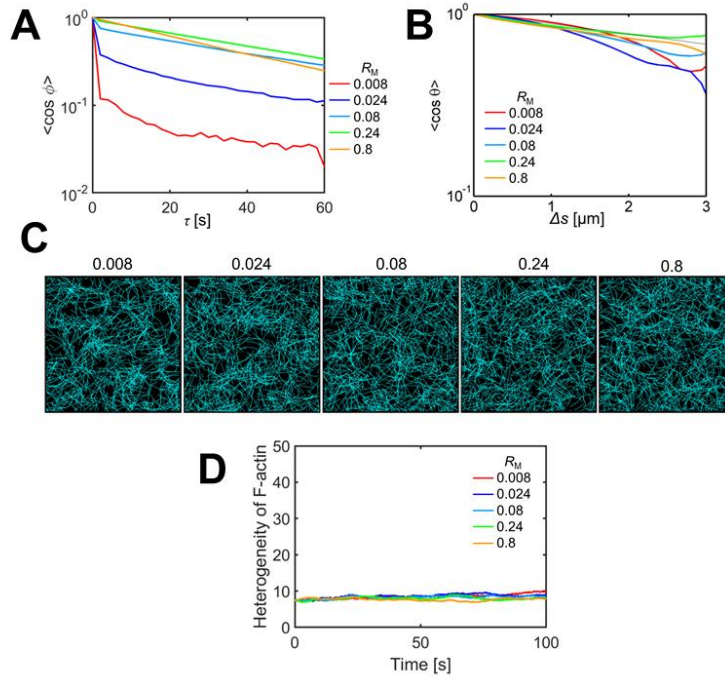
Figure 2.3. Effects of motor density (R_M). (A) Autocorrelation of velocities of F-actins with various R_M. With smaller R_M, persistency of F-actin movement tends to be lower due to a larger number of free F-actins and F-actins bound to only one motor. (B) A correlation between unit tangential vectors along contour of F-actins. A dotted line indicates the correlation corresponding to the persistence length of F-actin. (C) Morphology of networks with different R_M at the last time point, $t = 100$ s. (D) Heterogeneity of F-actin spatial distribution (Q_A). R_M hardly affects the heterogeneity.

Second, we altered $<L_f>$ between 0.62 μm and 5.06 μm. In these cases, we used $R_M = 0.08$ which is 10-fold smaller than the reference condition because we found that effects of $<L_f>$ with $R_M = 0.8$ are not significant. With larger $<L_f>$, the frequency of F-actins moving faster increases (Fig. 2.2C). Short F-actins are more likely to lose all connections to motors. Then, more F-actins diffuse in space with lower $<L_f>$ (Fig. 2.2D). In addition, the number of F-actins bound to only one motor that can move slower due to possible rotation also increases. These F-actins result in tails at low speed in the speed distribution. The range of $<L_f>$ for being these F-actins is determined largely by average distance between adjacent motors fixed in space. With lower R_M, the average distance increases, so more F-actins move slower. If F-actins are long, they can maintain connectivity to more than one motor despite a long distance between adjacent motors, so the speed can be relatively faster. By contrast, if motors are located very densely, effects of $<L_f>$ become negligible. Longer F-actins tend to be more curved since such F-actins are bound to many

44

of the sparsely distributed motors via bending (Fig. 2.4B). Despite their higher curvature, longer F-actins tend to move more persistently in one direction at a short timescale because very short F-actins can rotate due to lack of connectivity to motors (Fig. 2.4A). Regardless of $<L_f>$, F-actins show quite homogeneous distribution overall (Figs. 2.4C-D).
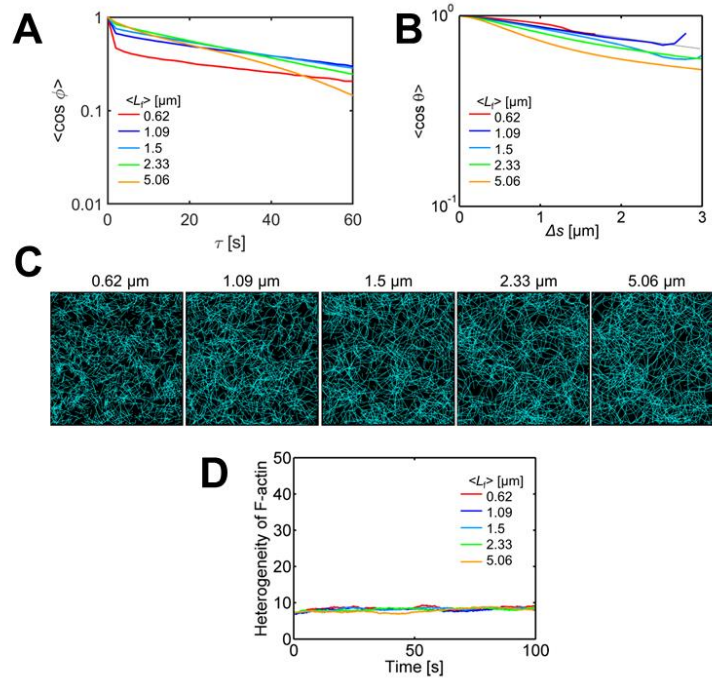
Figure 2.4. Influences of average length of F-actins ($<L_f>$). (A) Autocorrelation of velocities of F-actins. (B) A correlation between unit tangential vectors along contour of F-actins. A dotted line indicates the correlation corresponding to the persistence length of F-actin. With lower $<L_f>$, F-actins are less curvy because of a larger number of free F-actins and F-actins bound to only one motor. (C) Morphology of networks with various $<L_f>$ at the last time point, $t = 100$ s. (D) Heterogeneity of spatial distribution of F-actins (Q_A). In all cases, networks are very homogeneous.

Lastly, we varied k_{20} between 5 s^{-1} and 640 s^{-1}. As k_{20} increases, both unbinding and walking rates of motors measured in simulations are higher, consistent with imposed walking ($k_{w,M}$) and unbinding rates ($k_{u,M}$) of motors (Fig. 2.5A). The enhanced walking rate increases speed of F-actins in general (Fig. 2.5B). In addition, due to significantly higher unbinding rate, connections between F-actins and motors become very unstable. A higher unbinding rate leads to a lower number of active motors bound to F-actins at equilibrium (Fig. 2.5C), and F-actins frequently change their directions during movement (Fig. 2.5D). However, the curvature of F-actin and the heterogeneity of F-actin spatial distribution are not affected by k_{20} (Figs. 2.6A-C). F-actins

experience slightly larger tensile forces only at lower k_{20} because motors with high k_{20} mostly walk at unloaded velocity due to their high unbinding rate (Figs. 2.5A and 2.6D).
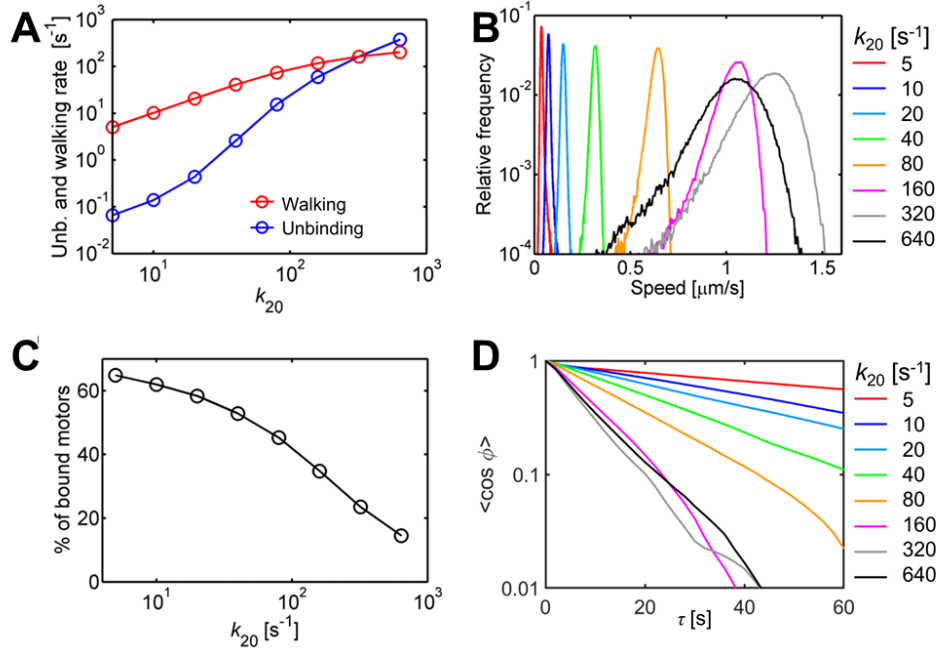
Figure 2.5. A mechanochemical rate in the cross-bridge cycle of myosin motors has a great effect on gliding motions of F-actins. We varied one of mechanochemical rates of myosin heads employed in the parallel cluster model, the ATP-dependent unbinding rate of motors (k_{20}). In these cases, volume-exclusion effects between F-actins were not included. (A) Unbinding and walking rates of motors measured from simulations. (B) Distribution of speed of F-actins. (C) Fraction of active motors that are bound to F-actins. With higher k_{20}, F-actins tend to move faster, but the speed is reduced at the highest k_{20} because the unbinding rate of motors is too high for the motors to walk stably on F-actins. (D) Autocorrelation of velocities of F-actins with various k_{20}. F-actins propelled by motors with higher k_{20} move much faster and therefore change directions more frequently during the same time interval.
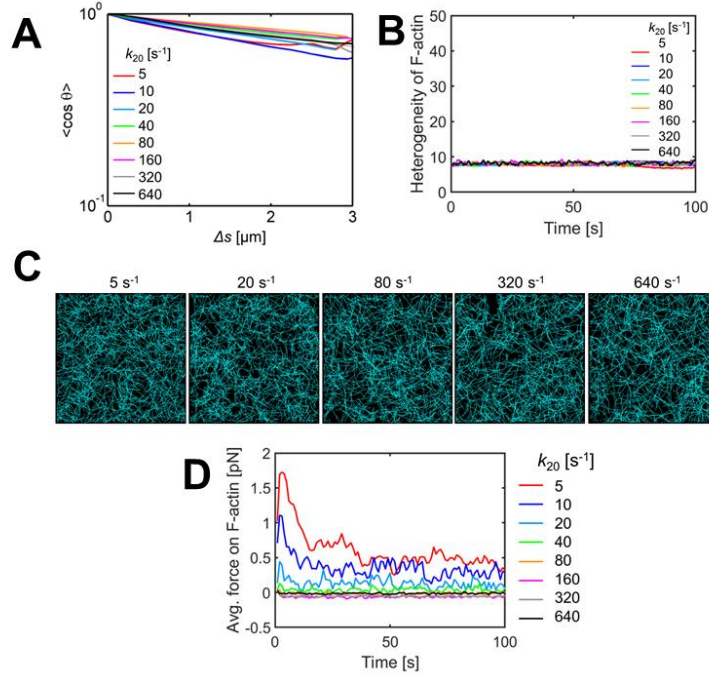
Figure 2.6. Influences of one of mechanochemical rates of myosin heads employed in the parallel cluster model, the ATP-dependent unbinding rate of motors (k_{20}). (A) A correlation between unit tangential vectors along contour of F-actin. A dotted line indicates the correlation corresponding to the persistence length of F-actin. (B) Heterogeneity of F-actin spatial distribution (Q_A). (C) Morphology of networks with various k_{20} at the last time point, $t = 100$ s. Networks are quite homogeneous, regardless of k_{20}. (D) Average tensile force exerted on F-actins. Motors with lower k_{20} exert slightly larger forces on F-actins due to higher stall force.

2.3.2 Collective behaviors of F-actins in the presence of volume-exclusion effects

In simulations described above, we ignored volume-exclusion effects to focus only on interactions between F-actins and myosin motors. However, in the motility assay experiments, F-actins can feel the existence of other F-actins via their physical volumes because F-actins are located at similar height. The degree of volume-exclusion effects between F-actins can be varied by altering crowding effects that push F-actins down toward a surface coated with myosin motors. Several motility assay experiments have demonstrated the emergence of collective behaviors of F-actins in the presence of strong volume-exclusion effects [50-54, 56].

We investigated roles of volume-exclusion effects between F-actins in gliding behaviors of F-actins by imposing high repulsive forces ($\kappa_{r,A} = \kappa^*_{r,A}$). It was observed that most of F-actins are aligned with each other when they collide, but they can still cross over each other if they encounter with a very large contact angle. With the reference actin concentration ($C_A = 60$ µM),

F-actins form thin bundles soon after they start moving (Fig. 2.7A). These bundles are merged into thicker bundles over time, and some of the bundles form ring-like structures. Some of the ring-like structures last till the end of simulations, whereas the others disappear after some time.
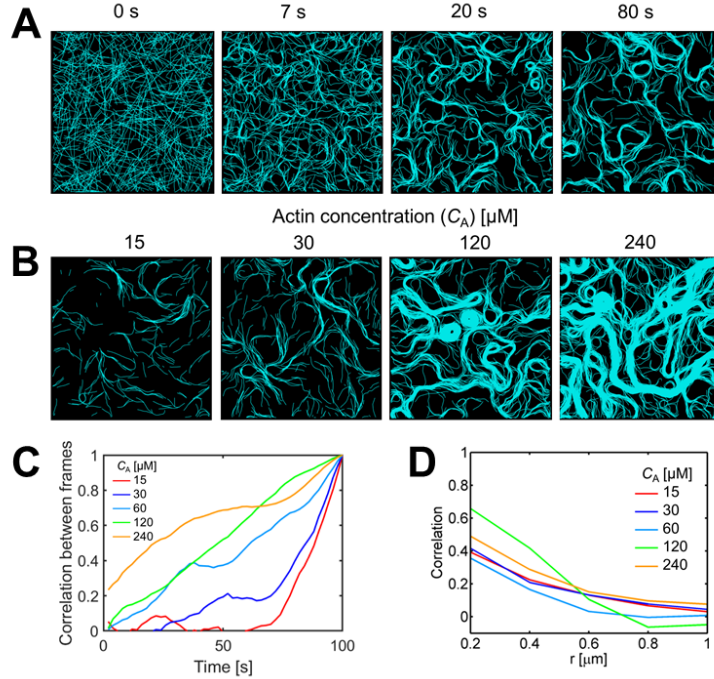
Figure 2.7. Volume-exclusion effects between F-actins lead to collective motions of F-actins. Actin concentration (C_A) is varied with reference strength of repulsive forces ($\kappa_{r,A} / \kappa^*_{r,A} = 1$). (A) Time evolution of network morphology with $C_A = 60$ μM. Thin bundles emerge first, and then thick bundles and ring-like structures are formed later. (B) Final network morphology with different C_A. (C) A correlation between network morphology at the end of simulations (100 s) and that at each time point. For example, a correlation value at 50 s represents a correlation between network morphology at 50 s and that at 100 s. Higher correlation values at later times in cases with large C_A indicate that network morphology does not change significantly near the end. (D) A correlation between velocities of pairs of endpoints on F-actins located at a distance r, which is averaged for last 50 s.

When C_A is reduced, ring-like structures emerge less frequently, and F-actins move in a more persistent manner and show less curvature because collisions between F-actins occur less frequently at lower C_A (Figs. 2.7B and 2.8A-B). At the lowest C_A (15 μM), ring-like structures are not formed anymore, whereas transient formation of bundles still takes place. By contrast, as C_A increases, thick and long bundles are formed over time. Persistency of F-actin motions decreases, and the curvature of F-actins increases (Figs. 2.7B and 2.8A-B). In all cases, there is no significant temporal change in the ensemble average of F-actin speed, indicating consistent motions of F-

actins regardless of the frequency of collision events (Fig. 2.8C). Heterogeneity of network morphology gradually increases and reaches a plateau to a different extent (Fig. 2.8D). With high C_A, network morphology does not vary much at later times (Fig. 2.7C). This observation is quite interesting in that the network forms a time-invariant frame along which F-actins can glide dynamically. Due to collision events, it is expected that neighboring F-actins move in a parallel manner in all cases. Indeed, we found that F-actins glide in a collective fashion by measuring a correlation between velocities of neighboring F-actins (Fig. 2.7D). Interestingly, the correlation at a distance smaller than 0.5 µm is maximal in a case with 120 µM. In this case, two large, thick ring-like structures are formed by behaving like a "sink" for F-actins; a number of F-actins are sucked into these structures and then trapped. In addition, distances between thick bundles and ring-like structures are relatively long. Thus, the correlation becomes very large in this case. With $C_A = 240$ µM, the distances become smaller, so the correlation includes many pairs of F-actins located within different bundles or ring-like structures. These F-actins do not necessarily move in the same direction, resulting in a lower correlation than that with $C_A = 120$ µM.
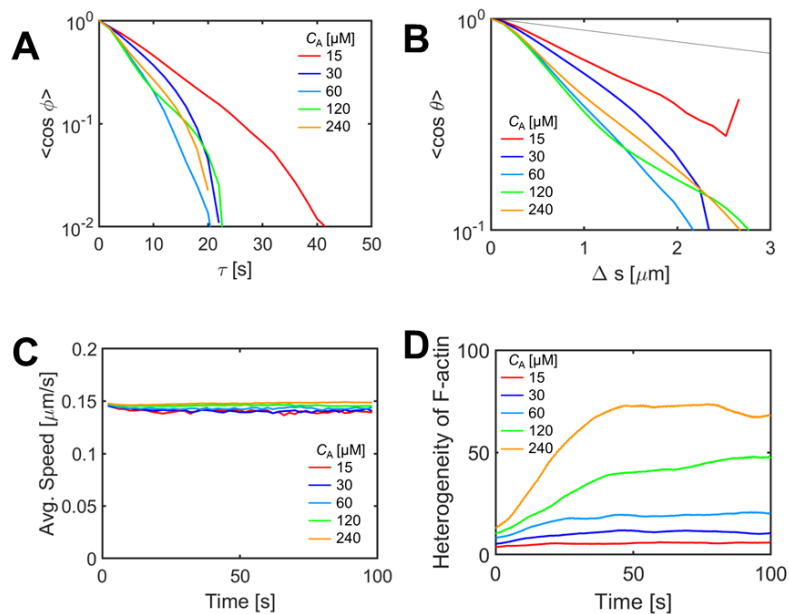
Figure 2.8. Effects of actin concentration (C_A) on motions of F-actins and network morphology in the presence of volume-exclusion effects ($\kappa_{r,A} = \kappa^*_{r,A}$). (A) Autocorrelation of velocities of F-actins with various C_A. (B) A correlation between unit tangential vectors along contour of F-actins. A dotted line indicates the correlation corresponding to the persistence length of F-actin. (C) Average speed of F-actins. (D) Heterogeneity of F-actin spatial distribution (Q_A).

We also probed influences of the extent of volume-exclusion effects on motions of F-actins with high C_A (= 120 µM) by varying the strength of repulsive forces acting between neighboring pairs of F-actins ($\kappa_{r,A}$). With 3-fold lower $\kappa_{r,A}$, ring-like structures are not formed anymore (Fig. 2.9A). Bundle-like structures still emerge, but bundle formation is not as clear as that in the reference case. With 10-fold lower $\kappa_{r,A}$, bundle formation is not obvious, becoming closer to cases without volume-exclusion effects shown earlier. By contrast, with 3-fold higher $\kappa_{r,A}$, a large number of ring-like structures are formed. Thus, with higher $\kappa_{r,A}$, network morphology tends to be more heterogeneous (Figs. 2.9A-B and 2.10A). The frozen network morphology emerging at later times is more apparent with higher $\kappa_{r,A}$ (Figs. 2.9C and 2.10B). At $C_A \leq 60$ µM, the correlation between velocities of neighboring F-actins is higher with larger $\kappa_{r,A}$, meaning that collective behaviors of F-actins are determined by the extent of volume-exclusion effects at lower actin concentration (Figs. 2.10C-D). However, at C_A = 120 µM, the correlation becomes maximal with the reference value of $\kappa_{r,A}$. Thick bundles and large ring-like structures in the case explained above lead to a higher correlation than many of smaller ring-like structures.
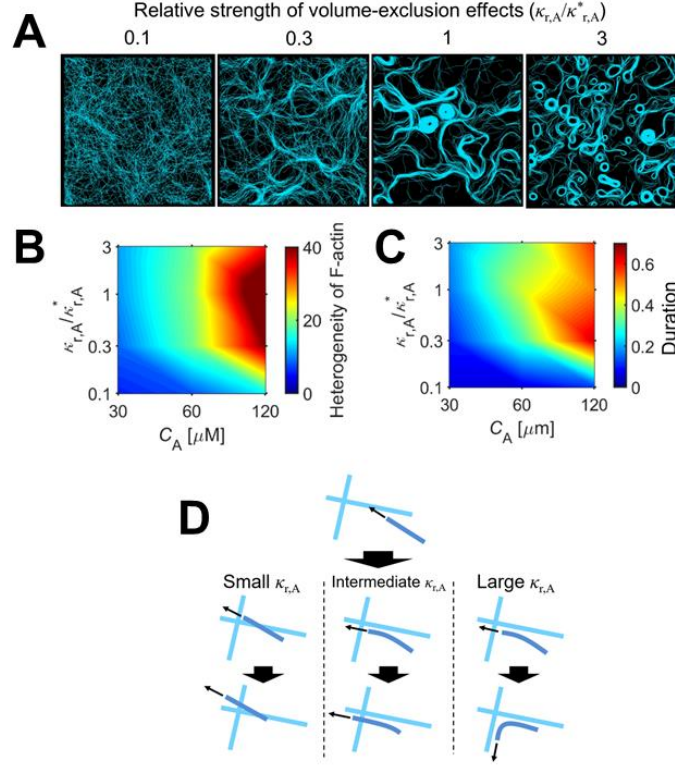
Figure 2.9. The extent of volume-exclusion effects between F-actins highly affects network morphology. The strength of repulsive forces ($\kappa_{r,A}$) is varied. (A) Final network morphology with different $\kappa_{r,A}$ at $C_A = 120$ μM. With stronger volume-exclusion effects, more ring-like structures appear. (B) Heterogeneity of final network morphology, (C) Duration during which a correlation between final network morphology and morphology at a time point is larger than 0.5, depending on C_A and $\kappa_{r,A}$. With larger $\kappa_{r,A}$, network morphology becomes more heterogeneous and does not change much at later times. Effects of $\kappa_{r,A}$ are weaker if C_A is smaller. (D) A schematic diagram showing differences in behaviors of F-actins after collisions with other F-actins. If volume-exclusion effects are very weak, F-actins cross over each other easily. If volume-exclusion effects are relatively strong, F-actins can align with each other if a contact angle at the moment of collision is small. However, they cross over each other if the angle is large. This behavior results in formation of thick, large bundles. With very strong volume-exclusion effects, F-actins cannot cross over each other regardless of whether the contact angle is large or small. Such a frequent change in the direction leads to formation of many, small ring-like structures.

Figure 2.10. Impacts of the extent of volume-exclusion effects on network morphology and collective motions of F-actins with three different actin concentrations (C_A = 30, 60, and 120 µM). (A) Heterogeneity of F-actin spatial distribution (Q_A). (B) A correlation between final network morphology at 100 s and morphology at each time point, t. (C-D) A correlation between velocities of two points on different F-actins located (C) near a distance r or (D) within 0.2 µm. The correlation values are averaged for last 50 s.

The dependence of F-actin motions and network morphology on volume-exclusion effects can be explained by what happens to F-actins when they encounter at a large or small contact angle. If volume-exclusion effects are very weak, F-actins cross over each other with a slight change in their gliding direction caused by weak repulsive forces (Fig. 2.9D, left). With relatively strong volume-exclusion effects, F-actins can align with each other if they encounter with a small contact

angle, but they cross over each other if the angle is large (Fig. 2.9D, center). This behavior can lead to the formation of thick, large bundles by allowing F-actins to move at longer distances until they encounter other F-actins with similar orientations. If the volume-exclusion effects are very strong, F-actins cannot cross over each other regardless of the contact angle (Fig. 2.9D, right). This results in a frequent change in their gliding directions and higher curvature, leading to the formation of ring-like structures.

2.3.3 Impacts of the density and unbinding rate of ACPs

Most of the traditional motility assay experiments were performed without ACPs that cross-link pairs of F-actins. More recently, several experiments demonstrated how different types of ACPs lead to distinct network morphology and F-actin movements at very high actin concentration (C_A) [13, 55, 56]. In addition, a myriad of experimental and computational studies have demonstrated that the amount of ACPs highly affects the contraction of actomyosin networks with myosin thick filaments (i.e. mobile motors) [22, 63, 77]. It is expected that even with lower C_A and immobile motors, the density and property of ACPs will still regulate contractile behaviors of networks. Among various ACP properties, we focus on the unbinding rate of ACPs that is expected to vary, depending on types of ACPs. For example, while scruin is known to form permanent cross-links between F-actins [36], most of the ACPs unbind from F-actins at distinct force-dependent rates [68]. We evaluated effects of density (R_{ACP}) and zero-force unbinding rate constant ($k_{u,ACP}^0$) of ACPs by varying them over wide ranges: $0.001 \leq R_{ACP} \leq 0.1$ and $0 \leq k_{u,ACP}^0 /$ $k_{u,ACP}^{0*} \leq 10$, where $k_{u,ACP}^{0*} = 0.115$ s^{-1} is a reference value of $k_{u,ACP}^0$. We did not include repulsive forces between F-actins in these simulations.

We observed that F-actins move slower and change their directions more frequently with higher R_{ACP} than those with lower R_{ACP} (Figs. 2.11A and 2.12A-B). This suggests that ACPs prevent F-actins from persistently moving via formation of cross-linking points between F-actins. If $k_{u,ACP}^0$ is increased with R_{ACP} fixed, the fraction of ACPs in an active state (i.e. bound to a pair of F-actins) is reduced (Fig. 2.13A), and also it becomes much easier for motors to displace F-actins because each cross-linking point exerts lower effective friction to F-actin due to more frequent unbinding events. Because of these two effects, F-actins move faster and more

persistently with higher $k_{u,ACP}^0$ (Figs. 2.11A and 2.12A-B). In addition, in a case with $R_{ACP} = 0.03$ and $k_{u,ACP}^0 = 0$, the average speed of F-actins is nearly zero (Fig. 2.11A), indicating that ACPs corresponding to ~3% of actins are sufficient enough to cross-link all F-actins into a network at $C_A = 60$ μM.
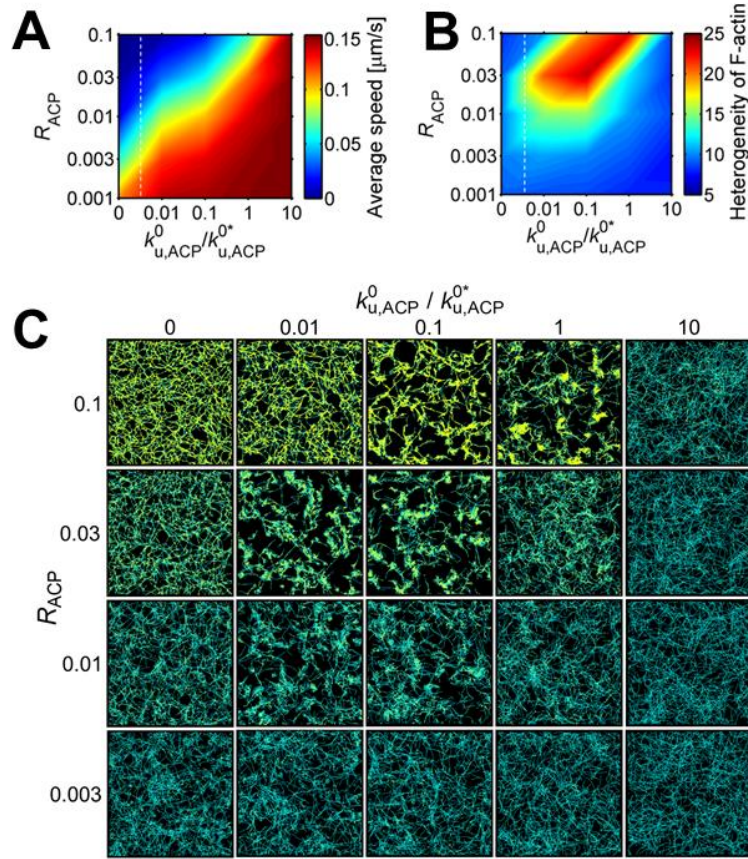
Figure 2.11. Motions and properties of F-actins drastically change depending on density (R_{ACP}) and zero-force unbinding rate constant ($k_{u,ACP}^0$) of ACPs. (a) Average speed of F-actin averaged for last 50 s. (b) Heterogeneity of F-actin spatial distribution and (c) network morphology measured in all cases at the last time point, $t = 100$ s. F-actins and ACPs are visualized by cyan and yellow, respectively. White dashed lines in (a-b) are drawn to include cases with $k_{u,ACP}^0 = 0$ in a log scale, so there is a discontinuity between the cases separated by the white dashed line.

Figure 2.12. Influences of density (R_{ACP}) and zero-force unbinding rate constant ($k_{u,ACP}^0$) of ACPs. (A) Speed distribution of F-actins. (B) Autocorrelation of velocities of F-actins. A spike at low τ in some curves originates from severe confinement of F-actins. (C) Heterogeneity of F-actin spatial distribution (Q_A). (D) Time evolution of average tensile force acting on F-actins. (E) A correlation between unit tangential vectors along contour of F-actins. Dotted lines indicate the correlation corresponding to the persistence length of F-actin.

Network morphology exhibits interesting dependence on R_{ACP} and $k_{u,ACP}^0$ (Figs. 2.11B-C and 2.12C). If there is no ACP unbinding ($k_{u,ACP}^0 = 0$), the heterogeneity of network morphology is slightly higher at $R_{ACP} = 0.003$-0.03. In addition, at this range of R_{ACP}, F-actins experience the largest tensile force (Figs. 2.12D and 2.13B). If ACPs form permanent cross-linking points, two populations of F-actins exist: cross-linked population and free population. Note that the latter

hardly affects heterogeneity of network morphology because they do not aggregate as shown earlier in cases without ACPs. Due to the absence of unbinding, there is no change in states of F-actins over time. Thus, in this case, R_{ACP} determines the number of F-actins in the two populations. If a network is cross-linked too loosely (R_{ACP} = 0.001), most F-actins glide on motors freely at speed close to the unloaded walking speed of motors (Fig. 2.11A), leading to homogeneous F-actin spatial distribution (Fig. 2.11B). Accordingly, tensile forces acting on F-actins and those exerted by motors are quite low (Figs. 2.12D and 2.13B-C). By contrast, if F-actins in a network are cross-linked too heavily (R_{ACP} > 0.01), most of F-actins cannot move far from their initial locations as seen in nearly zero average speed (Fig. 2.11A), resulting in relative homogeneous morphology (Figs. 2.11B-C). In addition, although forces generated by motors are similar in all cases with R_{ACP} > 0.001, net tensile forces acting on F-actins are smaller with R_{ACP} = 0.1 since much larger motor forces are required for buckling of short segments between numerous cross-linking points (Figs. 2.12D and 2.13B-C). Thus, under these two extreme conditions with high and low R_{ACP}, motors are not able to aggregate F-actins or generate large net tensile forces on F-actins. However, at intermediate level of R_{ACP}, motors can deform a network consisting of F-actins cross-linked relatively well by generating larger tensile forces originating from F-actin buckling.
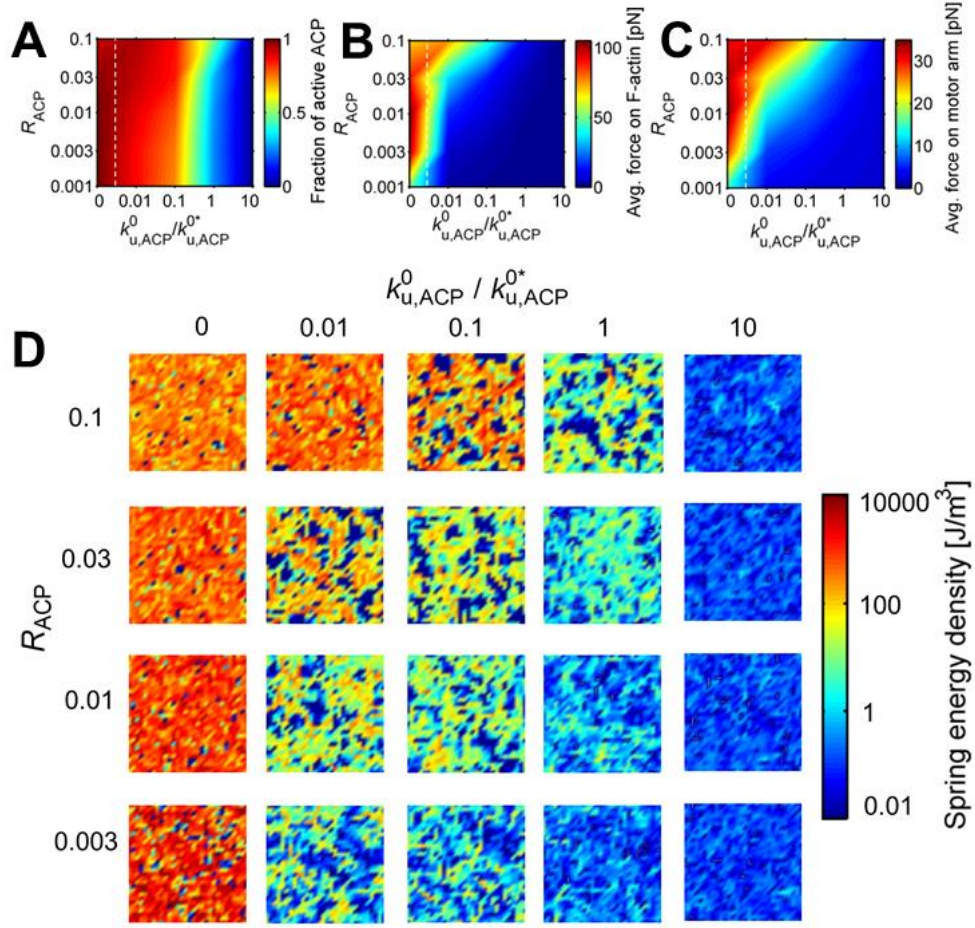
Figure 2.13. Effects of the density (R_{ACP}) and zero-force unbinding rate constant ($k_{u,ACP}^0$) of ACPs. (a) The fraction of active ACPs, which are ACPs that are bound to two F-actins. The fraction was averaged for last 50 s. (b) Tensile force acting on F-actins averaged for last 50 s. (c) Force exerted by motor arms averaged for last 50 s. White dashed lines in (a-c) are drawn to include cases with $k_{u,ACP}^0 = 0$ in a log scale, so there is a discontinuity between the cases separated by the white dashed line. (d) Visualization of spatial distribution of spring energy density in networks measured at $t = 100$ s via color scaling.

If ACPs can unbind from F-actins (i.e. $k_{u,ACP}^0 > 0$), highly heterogeneous networks with several clusters are observed because F-actins can be displaced significantly (Figs. 2.11B-C, 2.12C). Such high heterogeneity appears at a specific range of density of active ACPs, ~0.005 ≤ R_{ACP}^{active} ≤ ~0.05 (Fig. 2.13A), where R_{ACP}^{active} is the density of active ACPs, equal to the fraction of active ACPs times R_{ACP} (Fig. 2.13A). Interestingly, the average tensile force exerted on F-actins tends to

be proportional to R_{ACP}, unlike cases without ACP unbinding (Figs. 2.12D and 2.13B). Only one case (R_{ACP} = 0.1 and $k_{u,ACP}^0 / k_{u,ACP}^{0*}$ = 0.01) that exhibits less heterogeneous F-actin spatial distribution shows sustainable tensile force on F-actins (Figs. 2.12C-D). This is attributed to small loads on each ACP and stable cross-linking points with large effective friction. This implies that tensile stress in the presence of ACP unbinding is generated and sustained only in these networks when most of F-actins are cross-linked stably. By contrast, in all other cases, average tensile forces acting on F-actins reach a peak and then relax to non-zero asymptote. Both peak and equilibrium levels are inversely proportional to $k_{u,ACP}^0$.

Spring energy density in networks tends to be proportional to R_{ACP} but inversely proportional to $k_{u,ACP}^0$ in general (Fig. 2.13D), which is consistent with our previous study [63]. If $k_{u,ACP}^0$ is very small, and if R_{ACP} is very high, similar levels of spring energy emerge across the network because almost all F-actins are cross-linked stably throughout the network as seen in very homogeneous network morphology (Figs. 2.11B-C). By contrast, in cases where a network aggregates into clusters, high spring energy is concentrated mostly on the clusters since the clusters are not connected to each other (Figs. 2.11C and 2.13D).

2.4   Discussion

Since the 1980s, the in vitro motility assay has been used to study interactions between F-actins and myosin motors. By measuring gliding motions of a few F-actins propelled by myosin motors fixed on a surface, several properties of myosin motors, such as duty ratio and mechanochemical cycles, have been estimated [76, 78]. The system of in vitro myosin motility assay has advanced recently. When F-actin concentration was significantly increased with strong crowding effects, interesting collective motions of F-actins were observed [49]. In addition, inclusion of different types of ACPs resulted in formation of distinct structures [13]. Compared to experimental efforts, the motility assay has not been studied very actively via a computational model although a rigorous model can provide more insights than experiments. In this study, we investigated motions of F-actins in the motility assay, using our well-established agent-based computational model.

First, we investigated motions of F-actins without ACPs and volume-exclusion effects between F-actins. We showed how the average length of F-actin and the density and mechanochemical rate of motors affect motions of F-actins. Morphology of the network was very homogeneous in all cases regardless of a change in those parameters. However, it was observed that F-actins may move with different speed, persistency, and curvature depending on the properties of F-actin and motor. In particular, if continuous interactions between motors and F-actins are hindered due to either large spacing between motors or short filament length, many of F-actins cannot glide at speed close to the unloaded walking velocity of motors (Fig. 2.2). Indeed, other in vitro study showed that F-actins move slower at low motor density [79], and a computational study also showed that the movement of F-actins is much slower and less persistent if motor density is too low because the number of myosin heads bound to F-actins at a given time becomes too low[59], By contrast, in experiments and simulations performed with long F-actins and high motor density (i.e. small spacing between motors), the dependence on motor density and F-actin length has not been observed. For example, an in vitro study showed that the gliding speed of F-actin hardly depends on the length of F-actin varied between ~1 μm and ~17 μm with motor density of ~600 motors/μm^2 [80]. If these motors are uniformly distributed on a surface, average spacing between them is ~42 nm. In addition, a computational study reported that F-actin motility is independent of motor density varied between ~1,500 and ~6,000 motors/μm^2 which corresponds to average spacing of ~ 13nm to ~26 nm [60]. Under such high motor density, spacing between motors is much shorter than F-actins, so F-actins are likely to be bound to several motors unless F-actins are extremely short. In contrast to these studies, we reduced motor density substantially and found that the gliding speed of F-actins can depend significantly on F-actin length with motor density corresponding to average spacing of ~0.33 μm (R_M = 0.08). We also observed that dependence of the gliding speed on F-actin length is much weaker if motor density is 10-fold higher (data not shown). It is anticipated that dependence of F-actin gliding speed on F-actin length will be also observed in experiments if motor density is lowered significantly.

We also found that the gliding speed of F-actin shows biphasic dependence on one of the mechanochemical rates, the ATP-dependent unbinding rate (Fig. 2.5). As the rate increases, motors walk on F-actin faster and are detached from F-actin more frequently. As long as walking takes place more frequently than detachment from F-actin, the gliding speed of F-actins also increases in proportion to an increase in the ATP-dependent unbinding rate. However, if the rate becomes

too high, detachment from F-actin dominates walking, resulting in lower net gliding speed of F-actin than walking speed of motors. It is expected that a discrepancy between the gliding speed of F-actins and walking speed will be less even with very high ATP-dependent unbinding rate if F-actins are very long, or if motor density is very high as in experiments. As long as F-actins can interact with a few motors at each time point, F-actins can keep moving without significant delay even with a small duty ratio. This is reminiscent of a strategy that a thick filament consisting of skeletal muscle myosin motors with a very small duty ratio employs to stay on F-actins [76]. Indeed, previous computational [60] and in vitro studies [75, 79] with high motor density showed that F-actin gliding speed increases with higher ATP concentration and reaches a plateau, rather than showing a biphasic dependence on ATP concentration. This can be attributed to higher motor density used in the previous experiments [79] (~150 motors /μm^2 which corresponds to average spacing of ~ 81 nm) and simulations [60] (~1,500 to ~6,000 motors /μm^2 which corresponds to average spacing of ~ 13- 26 nm) than that used in our simulation(R_M = 0.008 to R_M = 0.8 which corresponds to average spacing of ~0.11 μm to ~1.1 μm). In addition, longer F-actin used in the previous experiments and simulations can prevent the gliding speed from decreasing at high ATP concentration. If these simulations and experiments are repeated with much lower motor density and shorter F-actins, the biphasic dependence of F-actin speed on ATP concentration would emerge.

Then, we showed volume-exclusion effects between F-actins affect motions of F-actins in the motility assay, thus resulting in bundles or ring-like structures (Figs. 2.7 and 2.9). If F-actins are aligned only when they encounter other F-actin at a small contact angle due to low $\kappa_{r,A}$, large, thick bundles are formed at high actin concentration. If F-actins are aligned with other F-actin at most of the collision events regardless of a contact angle due to high repulsive force, small ring-like structures dominantly emerge. Once the bundles and ring-like structures are formed in our simulations, network morphology does not change significantly over time. However, the thick bundles are comprised of consistently moving F-actins that enter, leave, or stay within the structures. It means that the system reached a steady state at network level in terms of morphology, but it is still very dynamic at filament level. However, if actin concentration becomes lower, F-actins transiently form thin bundles, resulting in a dynamic change in network morphology over time.

Formation of bundles has been suggested in previous studies where volume-exclusion effects between F-actins were modulated by varying concentration of crowding agents, such as methylcellulose (MC) and polyethylene glycol (PEG). With higher MC concentration, F-actins showed collective motions and formed bundles and ring-like structures at larger length-scales [49, 80]. It was also shown that F-actins move in a bidirectional manner along bundles, implying a dynamic steady state [49, 80]. However, formation of small ring-like structures has not been observed in previous experiments. If motility assay experiments are performed with very strong crowding effects and lower motor density, small ring-like structure may emerge. Emergence of large-scale flow of numerous F-actins was shown in other experiments [50-54]. The flow is initiated from seeds with a few F-actins, and the seeds gradually increase in size over time, becoming clusters with the large-scale flow [53]. These clusters are also in a dynamic steady state, maintaining relatively constant size by continuously losing and recruiting F-actins [53]. Because we employed a small computational domain ($10 \times 10 \times 0.1$ μm) and short F-actins, it is not likely to recapitulate such large dynamics structures. It is feasible to simulate a large system with long F-actins for directly comparing simulation results with experimental observations, by imposing a more computational resource to each simulation. However, it is beyond the scope of this study. In a future study, we will attempt to simulate large-scale dynamic structures and analyze collective behaviors of F-actins in greater depth.

Interestingly, it was reported in a recent study that F-actins form steady-state thick bundle structures even without myosins if crowding effects are strong [49]. In this study, F-actins are displaced because they grow rapidly from a surface via formin activities. Similarity in results implies that F-actins at high density can form the thick bundles as long as they keep moving somehow in the presence of strong volume-exclusion effects. In addition, collective behaviors were observed in experiments performed in a different setup. The ring-like structures were shown in an experiment with ACPs called fascin, and they were named "frozen steady states" [56]. Note that we observed them in simulations without any ACP, but they are much smaller than those observed in the experiment that are as large as ~30 μm in radius. We would be able to reproduce large-scale rings with both volume-exclusion effects and ACPs that connect only parallel F-actins, but this is beyond the scope of the current study. A computational study demonstrated that volume-exclusion effects between microtubules result in ordered structures composed of bundles [81]. In

addition, formation of ring-like structures and large-scale collective behaviors of microtubule were observed due to physical interactions between microtubules [15, 16, 82].

Lastly, we showed that inclusion of ACPs in a network without volume-exclusion effects between F-actins can significantly enhance the spatial heterogeneity of network morphology (Fig. 2.11). If there are too many ACPs, or if the unbinding rate of ACPs is too low, motors cannot readily break cross-linking points, resulting in a homogenous network with frozen or slowly moving F-actins. By contrast, if there are only a few ACPs, or if ACPs unbind from F-actins very frequently, F-actins move mostly freely due to unstable cross-linking points that can break by applied loads, leading to a homogenous network. At intermediate density and unbinding rate of ACPs, networks become quite heterogeneous because both good connectivity between F-actins and deformability via breakage of cross-linking points are achieved. A fraction of the weak cross-linking points break due to applied forces while the other stable ones keep holding pairs of F-actins. Note that an increase in the amount of ACPs or a decrease in the unbinding rate of ACPs results in a larger number of active ACPs bound to two F-actins at dynamic equilibrium, but there is a difference between the two cases. Even if two systems have the same amount of active ACPs at dynamic equilibrium, F-actins in a system with higher ACP unbinding rate can move faster because more transient cross-linking points lead to lower effective friction between two cross-linked F-actins.

This overall observation is consistent with previous studies showing the highest contractility of networks at intermediate density of ACPs [13, 22, 27, 55, 83]. A network cross-linked by ACPs in our model became heterogeneous only above the critical amount of active ACPs that corresponds to a percolation threshold, as suggested by [24, 84]. If there are too many active ACPs, contraction was reduced because buckling of F-actin is suppressed, which is consistent with the importance of buckling for contraction suggested by previous studies [25, 85, 86]. In addition, emergences of clusters at lower ACP density and meshes at higher ACP density are consistent with results of previous simulations for cytokinetic rings although we did not observe ring formation at intermediate ACP density due to immobile motors [87].

In this study, we proposed a computational model designed for simulating myosin motility assays in a more rigorous fashion than previous models. The model successfully recapitulated previous experimental observations and also showed new interesting behaviors of F-actins under various conditions. We demonstrated effects of each parameter on behaviors of F-actins and

networks by varying values of many parameters beyond the capability of experiments. In particular, volume-exclusion effects and ACPs play a very important role in the motions of F-actins and network morphology. In the near future, we will simulate the motility assay system in the presence of both volume-exclusion effects and ACPs. In addition, using the power and flexibility of our model, we will simulate a larger system for direct comparison with in vitro experiments as well as a motility assay with microtubules and kinesin motors that were employed in many recent studies.

3. EMERGENCE OF DIVERSE PATTERNS DRIVEN BY MOLECULAR MOTORS IN THE MOTILITY ASSAY

3.1 Introduction

The actin cytoskeleton continuously reorganizes and generates forces in cells, driving various cellular processes including cell migration and cytokinesis [88]. The dynamic and mechanical behaviors of the actin cytoskeleton, such as contractile motions, force generation, and cortical flows, are facilitated partly by myosin which is a molecular motor protein that walks toward the barbed ends of actin filaments (F-actins) [89-91]. It has been extensively studied how myosin motors generate forces and drive a morphological change in the actin cytoskeleton [92, 93]. Various types of in vitro experiments using reconstituted actomyosin network have been popularly used as a handy tool because interactions between F-actins and myosin can be probed without influences of other actin-associated proteins [24, 94].

One of widely used in vitro experimental systems is the motility assay in which myosin motors are attached to a glass surface with F-actins gliding on the surface due to interactions with the myosin heads [9, 95, 96]. the walking velocity and mechanochemistry of myosin motors have been discovered [74, 76, 78]. It has been also shown that F-actins can move in a collective fashion due to steric interactions between neighboring F-actins. One study found that F-actins are aligned better when filaments are longer and denser [11]. It was also demonstrated that F-actins form clusters, density waves, and swirls when actin concentration is above critical level [52]. Another study found that collisions between two F-actins approaching each other with acute angles result in the formation of patterns, such as polar clusters, nematic/polar bands, and rings [54]. Interestingly, some of these patterns exhibited active steady states with hardly changing global patterns despite consistently gliding F-actins. For example, after emergence of ring-like structures, F-actins kept entering, exhibiting swirling motions, and then leaving although overall ring shapes were maintained for a long time. The strength of steric interactions between neighboring F-actins can be controlled by the concentration of crowding agents that lead to depletion forces, such as methylcellulose (MC) or polyethylene glycol (PEG). It was shown that adding more MC leads to more noticeable alignment of F-actins [49]. The addition of PEG induced a change in the direction

of bundle movement; with low PEG level, bundles tend to move in their transverse directions, whereas they move in their longitudinal direction with high PEG level [9].

Several computational studies have been employed to better understand how various factors govern the collective motions of filaments in the motility assay. For example, a model based on Brownian dynamics simulated semiflexible filaments gliding on a surface to show different patterns emerging depending on the magnitude of active forces exerted by motors and the persistence length of filaments [97]. Filaments exhibit the flow of bundles with higher persistence length and lower Péclet number, where the Péclet number represents the rate of advection (affected by active forces) to the rate of diffusion (affected by viscosity and thermal forces). By contrast, they form swirls and spirals with shorter persistence length and higher Peclet number. A more recent computational study showed the effects of strength of repulsive forces and the rigidity and density of filaments on the formation of patterns, such as isotropic networks, bundles, and rings [14]. They found that both repulsive forces and filament rigidity contribute to collective motions by enhancing collision-induced alignment and altering the persistence of filament orientations, respectively. Although these studies provided insights into understanding the influences of parameters on diverse pattern formation in motility assay, implicit description of myosin motors using a constant force applied to filaments may limit the physiological relevance of the insights and lead to artifacts in results. Indeed, an agent-based model with explicit description of motors demonstrated that a distance between motors highly affects the velocity and persistency of filaments [59].

In this study, we employed an agent-based computational model of the motility assay with explicit immobile motors interacting with filaments. We rigorously incorporated the kinetics of motors including the force-velocity relationship and the binding and unbinding behaviors. We evaluated the influences of the length, rigidity, and concentration of filaments and the strength of repulsive forces on collective movements and the formation of various patterns. We found that four types of structures – homogeneous networks, flocks, bands, and rings – emerge as a result of subsequent collisions between gliding filaments. The frequency and morphology of the structures and the curvature, alignment, and rotational motions of filaments were analyzed to understand when and how these structures were formed.

3.2 Methods

3.2.1 Model overview

We used the agent-based model built introduced in Chapter 2 and used in our previous studies [27, 61-63]. Model parameters are shown in Table 3.1 and 3.2.

Table 3.1. List of parameters employed in the model.

Symbol	Definition	Value
$r_{0,A}$	Length of an actin segment	1.4×10^{-7} [m]
$r_{c,A}$	Diameter of an actin segment	7.0×10^{-9} [m] [69]
$\theta_{0,A}$	Bending angle formed by adjacent actin segments	0 [rad]
$\kappa_{s,A}$	Extensional stiffness of F-actin	1.69×10^{-2} [N/m]
$\kappa_{b,A}^{*}$	Reference bending stiffness of F-actin	2.64×10^{-19} [N·m] [70]
$r_{0,ACP}$	Length of an ACP arm	2.35×10^{-8} [m] [71]
$r_{c,ACP}$	Diameter of an ACP arm	1.0×10^{-8} [m]
$\theta_{0,ACP}$	Bending angle formed by two ACP arms	0 [rad]
$\kappa_{s,ACP}$	Extensional stiffness of ACP	2.0×10^{-3} [N/m]
$\kappa_{b,ACP}$	Bending stiffness of ACP	1.04×10^{-19} [N·m]
$r_{0,M}$	Length of a motor arm	1.35×10^{-8} [m]
$r_{c,M}$	Diameter of a motor arm	1.0×10^{-8} [m]
$\kappa_{s,M}$	Extensional stiffness of a motor arm	1.0×10^{-3} [N/m]
k_{20}^{*}	Reference ATP-dependent unbinding rate of myosin heads	20 [s^{-1}]
N_h	Number of heads represented by a motor arm	8
N_a	Number of arms in a motor	1
$k_{n,A}$	Nucleation rate of actin	$0.000125 - 1$ [μM^{-1}s^{-1}]
$k_{+,A}$	Polymerization rate of actin at the barbed end	60 [μM^{-1}s^{-1}]
$k_{u,ACP}^{0*}$	Reference zero-force unbinding rate constant of ACP	0.115 [s^{-1}] [68]
$\lambda_{u,ACP}$	Sensitivity of ACP unbinding to an applied force	1.04×10^{-10} [m] [68]
$\kappa_{r,A}$	Strength of a repulsive force	1.69×10^{-3} [N/m]
Δt	Time step	1.15×10^{-5} [s] or 2.875×10^{-6} [s]
μ	Viscosity of surrounding medium	8.6×10^{-1} [kg/m·s]

Table 3.1 continued

$k_B T$	Thermal energy	4.142×10^{-21} [J]
C_A	Actin concentration	60 [μM]
R_M	Motor density (= Ratio of motor concentration to C_A)	0.008 – 0.8
R_{ACP}	ACP density (= Ratio of ACP concentration to C_A)	0 – 0.1
$<L_f>$	Average length of F-actins	0.69 – 3.02 [μm]

Table 3.2. List of parameter values used for adopting "parallel cluster model." [72, 73]

Symbol	Definition	Value
k_{01}	A rate from unbound to weakly bound state	40 [s^{-1}]
k_{10}	A rate from weakly bound to unbound state	2 [s^{-1}]
k_{12}	A rate from weakly bound to post-power-stroke state	1000 [s^{-1}]
k_{21}	A rate from post-power-stroke to weakly bound state	1000 [s^{-1}]
k_{20}	A rate from post-power-stroke to unbound state	5-640 [s^{-1}]
F_0	Constant for force dependence	5.04×10^{-12} [N]
E_{pp}	Free energy bias toward the post-power-stroke state	-60×10^{-21} [J]
E_{ext}	External energy contribution	0 [J]
d	Step size	7×10^{-9} [m]
k_m	Spring constant of the neck linkers	1.0×10^{-3} [N/m] (= $\kappa_{s,M}$)

In the model, filaments are modeled as serially connected cylindrical segments with polarity defined by pointed and barbed ends, and motors are modeled as one cylindrical segment whose end is fixed on the surface (Fig. 3.1). The other end of the motor segments binds to binding sites located on filaments and walks toward the barbed end, resulting in the gliding motions of filaments. The motors unbind from filaments when they walk beyond the barbed ends and can also unbind from anywhere on filaments in a force-dependent manner. The walking and unbinding rates of motors are determined by the parallel cluster model (Fig. 3.2). The displacements of filaments at each time step are calculated by the Langevin equation. For deterministic forces in the Langevin equation, we consider extensional and bending forces and repulsive forces acting between overlapping filaments.
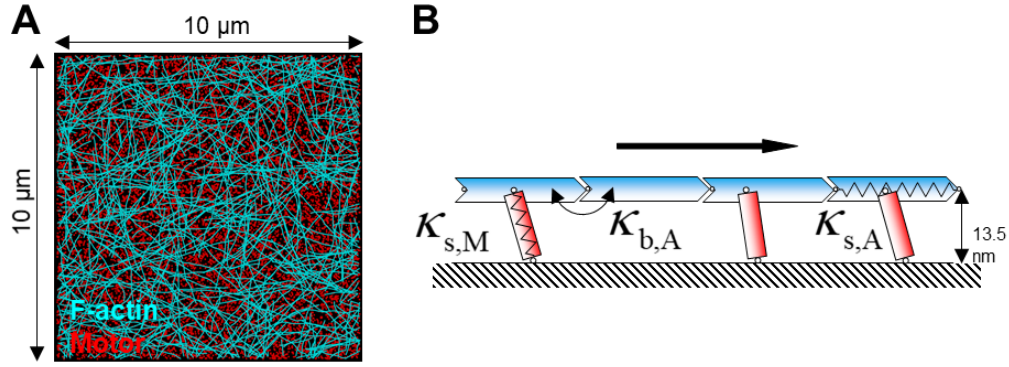
Figure 3.1. Schematic of Model Setup. (A) Computational domain of the model setup. (B) Representation of interactions between actin and myosin.
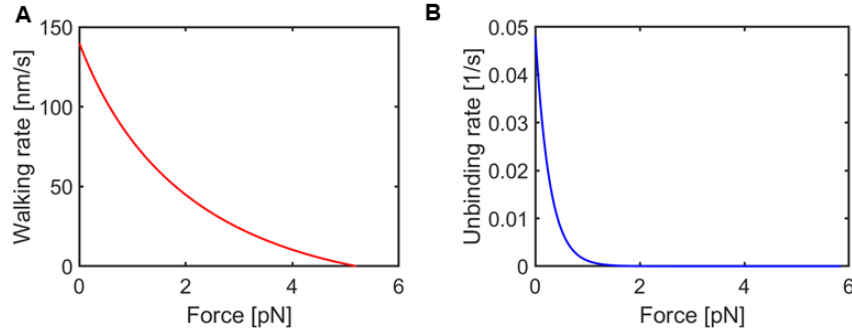
Figure 3.2. Myosin and Unbinding Rate depend on Force. (A) Walking rate of myosin heads in terms of the applied force. (B) Unbinding rate between myosin heads and f-actin in terms of the applied force.

We employed a thin three-dimensional computational domain ($10\times10\times0.1$ μm) with the periodic boundary condition in the x and y directions (Fig. 3.1A). Motors are allocated randomly on the x-y plane with one end located in the same z position ($z = 0$ μm). Filaments are formed by the nucleation and polymerization of cylindrical segments located in the same z position ($z = 13.5$ μm). The distance of 13.5 nm between filaments and motors corresponds to the equilibrium length of motor cylindrical segments. The nucleation event was simulated by the emergence of one filament segment in randomly selected x, y positions at a given nucleation rate. The polymerization event was simulated by adding segments to existing filament segments at a given polymerization rate. During filament assembly, some of the motors bind to filaments if they are proximal enough to bind to the filaments. After the completion of filament assembly, motors start walking toward

the barbed ends of filaments. We disabled fluctuation of filaments in the z-direction, meaning that all filaments stay in the same z-position throughout the simulation.

3.2.2 Evaluation of average speed and collective behaviors of filaments

First, the velocity of endpoints of all filament segments, $\mathbf{v}_{i,A}(t)$, is calculated every two seconds to minimize the influence of thermal fluctuation on velocity calculation. Then, the average speed of filaments is calculated by averaging $|\mathbf{v}_{i,A}|$ over all endpoints and all time points. As in our previous study [44], a correlation between the velocities of neighboring endpoints is quantified for evaluating the extent of collective motions of filaments:

$$\left\langle \cos\alpha(r,t) \right\rangle = \left\langle \frac{\left|\mathbf{v}_{i,A}(t) \cdot \mathbf{v}_{j,A}(t)\right|}{\left|\mathbf{v}_{i,A}(t)\right|\left|\mathbf{v}_{j,A}(t)\right|} \right\rangle \tag{3.1}$$

where i and j are the indices of two endpoints, and α is an angle between two velocity vectors. Only pairs of endpoints for last 20 s whose distance is smaller than 0.4 μm are considered for this calculation; collective behaviors tend to emerge at late times, and the threshold distance of 0.4 μm was selected because it results in quite different correlation values from distinct network morphology.

3.2.3 Quantification of ring formation

The extent of formation of ring-like structures was evaluated by manually counting the number and size of rings and by the curl of a velocity field representing filament motions. For the manual counting, we identified circle-shaped closed loops consisting of filaments as rings via ImageJ. Loops with raindrop shapes were not considered rings. The size of the rings corresponds to the longest distance that can be measured between any two points on the circumference of the rings.

The curl serves as a tool for indirectly estimating the extent of ring formation. To calculate the velocity field, the computational domain was first divided into $N_G \times N_G$ grids in the x and y directions. For filament concentration > 15 μM, N_G was set to 50, whereas for filament concentrations ≤ 15 μM, N_G was set to 40 because the number of filament segments in each grid is substantially lower. These values for N_G were carefully determined by comparing curl values

with various grid sizes (Fig. 3.3). Velocities of filament segments located within each grid are averaged to calculate for a velocity vector in the field. Then, the curl of the velocity field was calculated every 2 seconds using data for the last 50 s. The absolute value of each curl value for every grid was averaged across all time points. Larger average curl values are indicative of greater rotational motions of filaments.
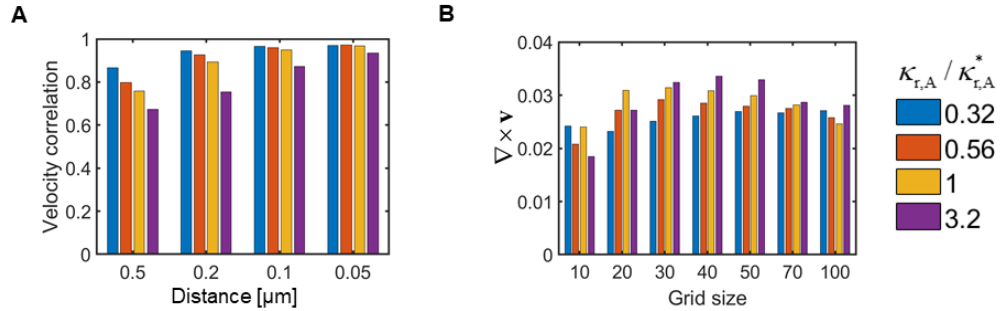
Figure 3.3. Velocity correlation and grid size at different radius and grid size, respectively, for various strength of volume-exclusion effects. (A) Velocity correlation found using F-actin within a different distance. (B) Curl found using different grid sizes for various strength of the volume-exclusion effect.

3.2.4 Apparent persistence length of filaments

The persistence length of filaments (l_p) is proportional to their bending stiffness or flexural rigidity:

$$l_p = \frac{\kappa_{b,A} r_{0,A}}{k_B T} \tag{3.2}$$

where $\kappa_{b,A}$ is the bending stiffness, $r_{0,A}$ is the equilibrium length of a filament segment, and $k_B T$ is thermal energy. However, filaments with identical bending stiffness may show a different curvature depending on inter-filament interactions or interactions between filaments and motors. To calculate "apparent" persistence length (l_{ap}) that represents the actual curvature of filaments, we first evaluated a correlation between unit tangential vectors defined along the contour of filaments, $\mathbf{u}(s)$:

$$\langle \cos \theta(\Delta s) \rangle = \langle \mathbf{u}(s) \cdot \mathbf{u}(s + \Delta s) \rangle \tag{3.3}$$

70

where s is a contour coordinate along filament contour. Apparent persistence length (l_{ap}) is calculated by fitting an exponentially decreasing function, exp ($-\Delta s/l_{ap}$) to $\langle \cos \theta(\Delta s) \rangle$.

3.2.5   Evaluation of network morphology

For evaluating network morphology, we divided the computational domain into $N_G \times N_G$ grids and then counted the number of filament segments in each grid ($\rho^{i,j}$), where (i, j) represents the x and y positions of each grid. First, we quantified how early a network reaches a steady state by calculating a correlation between a matrix comprised of $\rho^{i,j}$ at the end of simulations and that at each time point. We found duration for which the correlation is greater than 0.8. Longer duration means that network morphology reaches a steady state earlier.

In addition, as in our previous study [44], we quantified homogeneity of network morphology (Q) using the following:

$$Q = \frac{1}{2N_G}\left[\sum_{i=1}^{N_G} \text{std}\left(\rho^{i,j}\big|_{j=1..N_G} \right) + \sum_{j=1}^{N_G} \text{std}\left(\rho^{i,j}\big|_{i=1..N_G} \right) \right] \tag{3.4}$$

where std stands for standard deviation, and N_G is set to 30. For this calculation, we used data after Q reaches 0.8 to focus on network heterogeneity at a steady state.

3.2.6   Explicit and implicit motor description

Most of the previous computational models for the motility assay employed implicit motors, which means constant propulsion force is applied to filaments to mimic active forces exerted by motor activities. Such an approach has been popular because it can reduce the computational cost of simulations substantially. However, it is not clear whether implicit and explicit methods can produce similar results in the motility assay. To compare the effects of implicit and explicit motors, we ran a few simulations with implicit motors (Fig. 3.4). To determine the appropriate value of a propulsion force that represent the activities of implicit motors, we compared the average gliding speed of filaments in simulations with explicit and implicit motors (Fig. 3.4A). For this comparison, repulsive forces between filaments were not included in order to avoid a change in filament speed due to collisions between filaments. We found the propulsion

force that results in similar average gliding speed. When we ran simulations with the selected propulsion force, it was observed that filaments do not form rings unlike cases with explicit motors (Fig. 3.4C, D). In addition, it was noticeable that a larger fraction of filaments exhibits lower gliding speed in cases with implicit motors than those in cases with explicit motors (Fig. 3.4B). We explained the origins of different filament behaviors caused by implicit motors in Supplementary Text. Observation of such differences imply that our model with explicit motors can generate more rigorous results that may not be recapitulated by models with implicit motors.
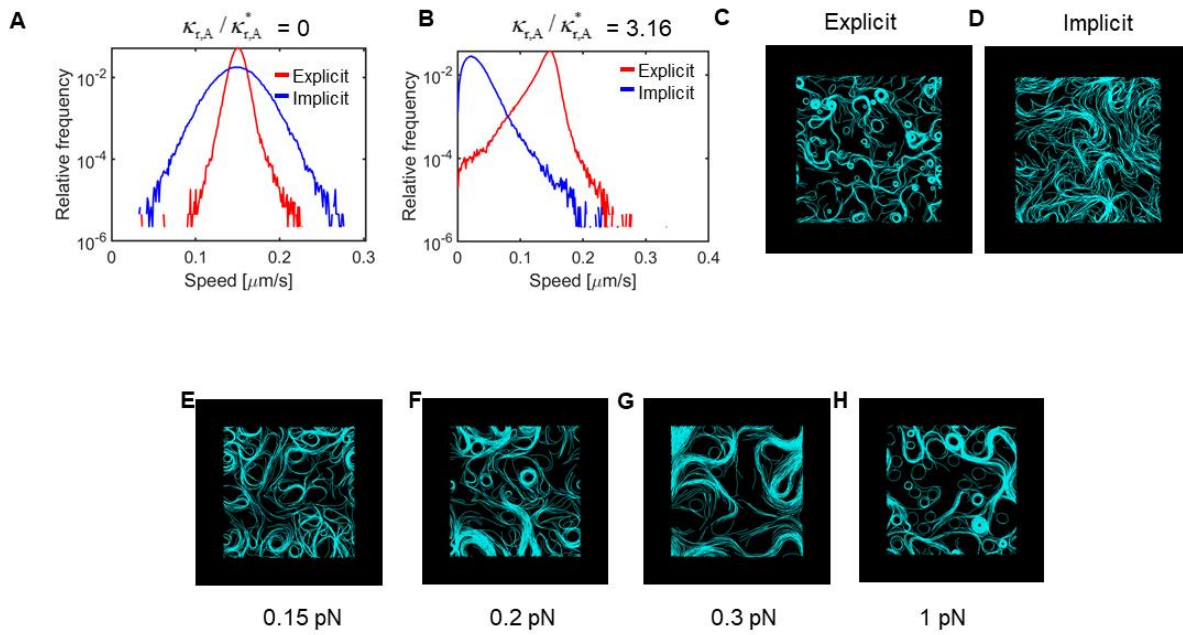
Figure 3.4. Difference between implicit and explicit motors on collective behavior of F-actin. (A-B) Distribution of f-actin speed with implicit and explicit motors with a low (A) and high (B) strength of the volume-exclusion effect. (C-D) Snapshots showing the collective behavior of f-actin with explicit motors (C) and implicit motors (D). (E-H) Snapshots showing the collective behavior of f-actin with implicit motors at force of 0.15 pN (E), 0.20 pN (F), 0.30 pN (G), and 1 pN (H).

3.3   Results

Previous in vitro studies have shown that collective motions of filaments are governed by i) the strength of repulsive forces between filaments, ii) bending stiffness, iii) filament concentration, and iv) average filament length [9, 12, 54]. In addition, a recent computational study showed that repulsive forces and bending stiffness affect pattern formation by enhancing or

reducing alignment between filaments [14]. We first validated the ability of our computational model to simulate the motility assay by probing effects of repulsive forces and bending stiffness. Then, we further investigated influences of filament concentration and length on the collective motions of filaments. With variations in the four parameters, we observed four types of patterns: homogeneous network, flocking, band, and ring. The homogeneous network indicates a structure with uniformly distributed filaments maintained for the entire duration of simulations. The flocking refers to loose, short bundles that keep disappearing after short time and appearing in different locations. The band means dense, thick bundles that are sustained till the end of simulations after formation. The ring represents closed loops within which filaments rotate.

3.3.1   Repulsive force and bending stiffness governed collective motions

First, we varied the strength of repulsive forces ($\kappa_{r,A}$) and bending stiffness ($\kappa_{b,A}$). With weak repulsive forces and high bending stiffness, homogeneous networks were formed without noticeable alignment of filaments (Figs. 3.5A, B); rigid filaments hardly change their gliding directions by weak repulsive forces from collision with other filaments. If the strength of repulsive forces increases or bending stiffness decreases, a transition from the homogeneous networks to flocks or bands occurs because filaments can change their gliding directions by repulsive forces under such a condition. The bands are formed when filaments can be bent enough to result in good alignment after collisions. The flocks arise when weak volume-exclusion effects cannot change their directions enough to form tight bands after collisions but enough to induce loose alignment of filaments. If filaments become softer and repulsive forces become stronger simultaneously, more rings with smaller size start emerging as a result of severe bending deformation and alignment of filaments (Figs. 3.2A, B). Rings always coexisted with bands because both of them originate from aligned motions of a large number of filaments. The average curvature of filaments was also greater with smaller bending stiffness and stronger repulsive forces (Fig. 3.2C). The curvature tends to decrease in the order of ring (largest), band, flock, and homogeneous network (smallest), so there is a correlation between the average curvature and the dominant types of structures. Structures formed by collective behaviors of filaments tended to last longer if they are rings and bands that resulted from alignment of numerous filaments (Fig. 3.2D). Overall

morphology was more heterogeneous with rings and bands, but if rings become very small, it became less heterogeneous (Fig. 3.2E).
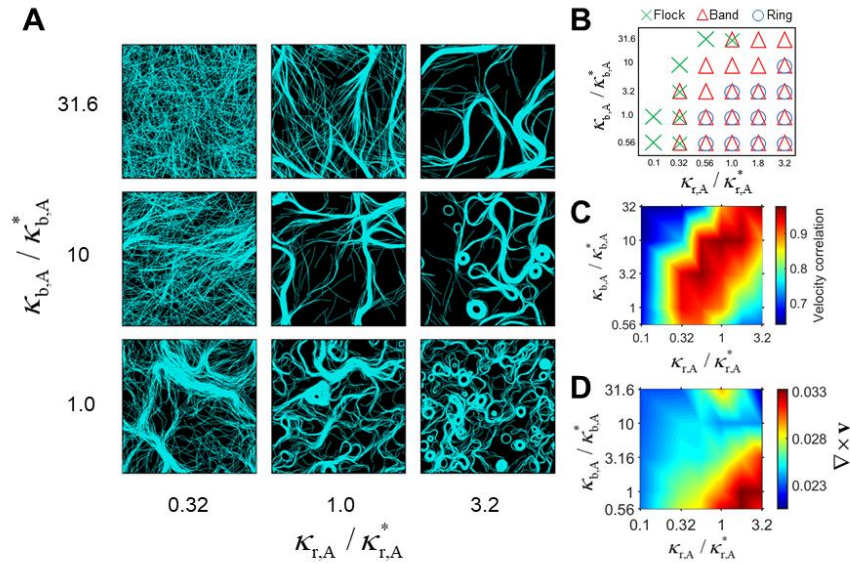
Figure 3.5. Collective behaviors of F-actins depending on bending stiffness ($\kappa_{b,A}$) and the strength of volume-exclusion effects ($\kappa_{r,A}$). (A) Snapshots taken at 100 s. (B) Emergence of different types of structures: rings (circles), bands (triangles), and swarms (crosses). (C) Correlation of velocities of neighboring F-actins averaged between 50 s and 100 s. Higher correlation values mean more collective motions of F-actins. (D) The curl of a velocity field calculated by averaging velocities of F-actins. The curl values indicate the extent of rotational movements. Larger curl values imply formation of more ring structures.

The extent of collective behaviors of filaments was quantified by calculating a correlation between velocities between neighboring filaments (Fig. 3.5C). The velocity correlation was the highest under conditions at which bands predominantly appear; in bands, a large number of filaments move in a parallel or anti-parallel manner, increasing the velocity correlation substantially. If there are many rings, filament bundles forming the rings were thinner, resulting in lower velocity correlation. The curl of the velocity field was also calculated to evaluate the degree of rotational motions of filaments. (Fig. 3.5D). It showed larger values when more rings were formed because filaments belonging to the rings rotate along the circular shape of the rings, leading to greater rotational motions on average.

3.3.2 High filament concentration significantly affected collective motions of filaments

It was shown that collective behaviors of filaments occur only above critical filament concentration [52]. Also, a previous computational study showed the emergence of different types of structures with various filament concentrations [14]. To better understand how the importance of volume-exclusion effects varies depending on the number of filaments, we ran simulations with various filament concentrations and repulsive force strength values. When the concentration of filaments decreased below the reference level (C_A < 60 µM), thick bands disappeared, and more flocks appeared (Figs. 3.6A, B). In addition, all of flocks, bands, and rings became thinner since the average number of filaments forming those structures was reduced. The number of rings decreased significantly. Interestingly, when the repulsive force was not weak ($\kappa_{r,A} / \kappa_{r,A}^{*} \geq 1$), the size of rings did not increase noticeably with lower filament concentration (Figs. 3.3A, B). We initially expected that lower filament concentration provides more space between filaments on average and thus would lead to formation of larger rings. However, based on these results, the strength of repulsive forces and bending stiffness are major governing factors for the ring size rather than filament concentration. The average curvature of filaments and the stability of structures tended to be greater under conditions where rings and bands were formed dominantly, so the decrease in the filament concentration reduced those quantities (Fig. 3.3C, D). Overall morphology was more heterogeneous when the number of filaments was reduced (Fig. 3.3E); in the sparse condition, structure formed by collective filament behaviors emerged in only a few locations, which contributes to substantial enhancement of heterogeneity. Velocity correlation was the highest when thick, tight bands were formed (Fig. 3.6C). The correlation was also high at the lowest filament concentration with repulsive forces equal to or stronger than the reference level because most of filaments were used for forming a few structures under the conditions. The range of repulsive force strength for high velocity correlation values was higher with lower filament concentration since it is hard to keep filaments together under a sparser condition. The curl of the velocity field showed the largest values when many rings were formed (Fig. 3.6D). The curl value was relatively high when flocking behaviors emerged with weak repulsive forces and filament concentration below the reference level. We observed that flocks showed rotational motions at larger scale under these conditions, which is reminiscent of a flock of bird circling around in sky. This large-scale rotational movement led to the large curl value.
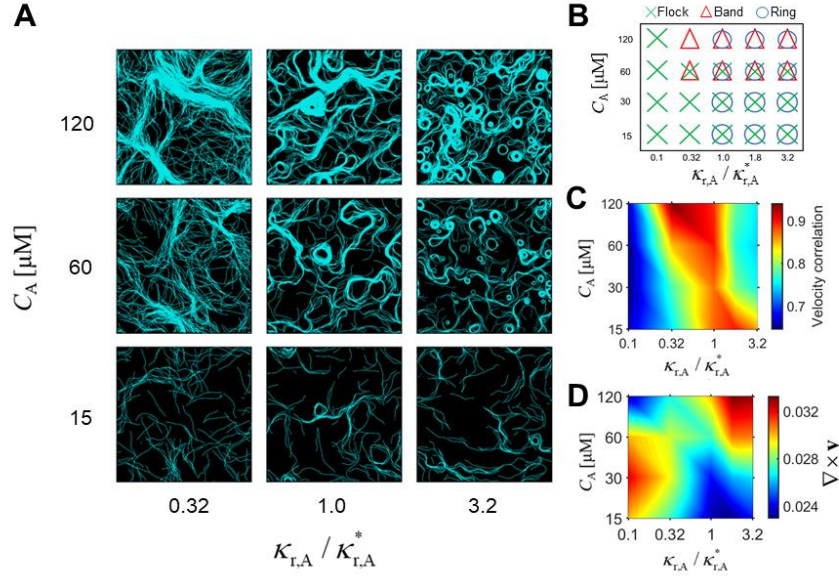
Figure 3.6. Effects of the strength of volume-exclusion effects ($\kappa_{r,A}$) at different actin concentration (C_A) on collective behaviors of F-actins. (A) Snapshots taken at 100 s. (B) Formation of different kinds of structures: rings (circles), bands (triangles), and swarms (crosses). (C) Velocities correlation of neighboring F-actins averaged between 50 s and 100 s. Larger correlation values indicate greater collective motions of F-actins. (D) The curl of a velocity field calculated using F-actin velocities. The curl values represent the degree of rotational motions. Higher curl values indicate the greater extent of ring formation.

In addition, we probed the significance of filament concentration depending on bending stiffness. In general, the effects of a change in the filament concentration are very similar to observations described above. Fewer filaments resulted in thinner structures. At the lowest concentration, structures became too thin to be categorized as bands, so they were considered as flocks (Figs. 3.7A, B). Interestingly, the velocity correlation tended to be higher with lower filament concentration (Fig. 3.7C). As the spatial distribution of filaments became sparser, a smaller number of filaments formed a few flocks, resulting in high velocity correlation. The curl of a velocity field showed high values under conditions with the formation of many, small rings (Fig. 3.7D).
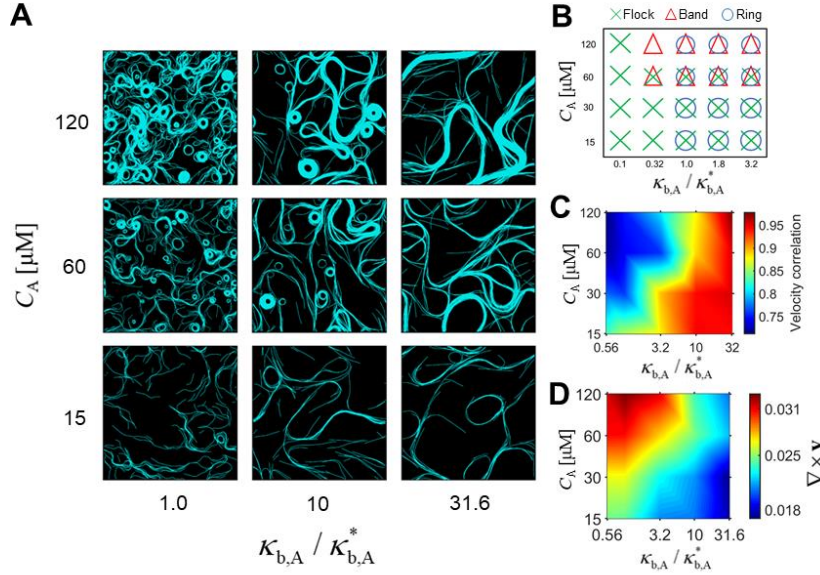
Figure 3.7. Influences of bending stiffness ($\kappa_{b,A}$) with different F-actin concentration (C_A) on collective motions of F-actins. (A) Snapshots taken at 100 s. (B) Appearance of distinct types of structures: rings (circles), bands (triangles), and swarms (crosses). (C) Correlation of velocities of adjacent F-actins averaged between 50 s and 100 s. Higher correlation values represent more collective motions of F-actins. (D) The curl of a velocity field calculated by averaging velocities of F-actins. The curl values indicate the extent of rotational movements. Larger curl values represent formation of more ring structures.

3.3.3   Longer filaments enhanced collective filament motions

Shorter filament length was shown to reduce filament alignment in previous in vitro motility assays [11]. Also, a former computational study investigated the effects of filament length on pattern formation [14]. Here, we evaluated how a variation in filament length affects pattern formation and collective filament behaviors, depending on repulsive force strength, bending stiffness, and filament concentration. We varied average filament length ($<L_f>$) between 0.5 μm and 4 μm.

First, we probed the effects of filament length with varied repulsive force strength. Overall, longer filaments induced the formation of rings and bands (Figs. 3.8A, B). The number of rings was proportional to the filament length. (Fig. 3.4A). When filaments were very short, flocks emerged instead of bands and rings. However, a change in the filament length hardly affected the

77

size of rings (Fig. 3.4B) The filament curvature was lower with shorter filaments in cases with strong repulsive forces although it hardly changed due to a change in the filament length with weaker repulsive forces (Fig. 3.4C). With shorter filaments, the stability of structures and the heterogeneity of morphology reduced because the short filaments are less likely to form tight bands or rings (Figs. 3.4D, E). The velocity correlation showed relatively high values at a wider range of repulsive force strength values when filaments were shorter (Fig. 3.8C); to form bands or rings leading to high velocity correlation, stronger volume-exclusion effects are necessary if filaments are shorter. The curl of the velocity field showed a tendency to decrease with shorter filaments due to formation of fewer rings (Fig. 3.8D).
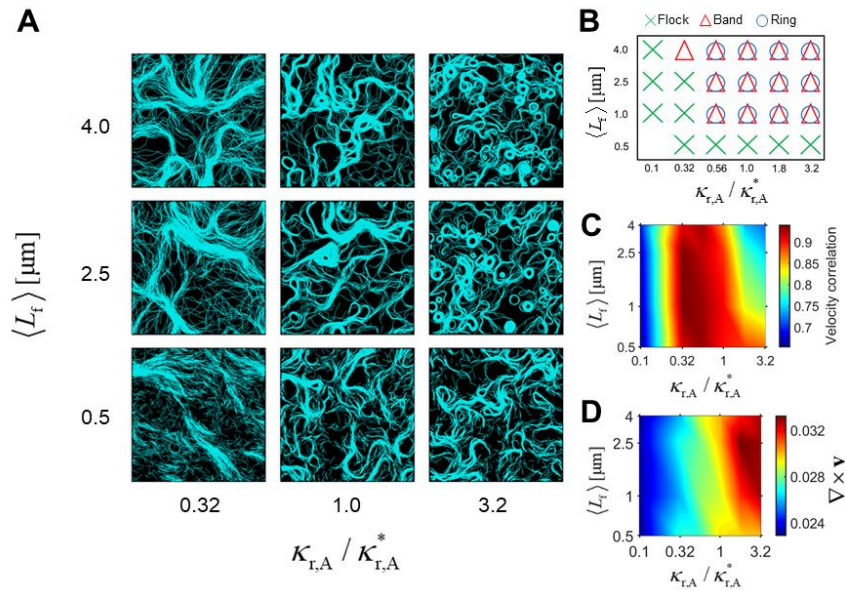
Figure 3.8. Collective motions of F-actins with different average F-actin lengths ($<L_f>$) and various strengths of the volume-exclusion effects ($\kappa_{r,A}$). (A) Snapshots taken at 100 s. (B) Emergence of different types of structures: rings (circles), bands (triangles), and swarms (crosses). (C) Correlation of velocities of neighboring F-actins averaged between 50 s and 100 s. Higher correlation values mean more collective motions of F-actins. (D) The extent of rotational movements indicated by the curl of a velocity field calculated from F-actin velocities. Higher curl values imply more ring formations.

Next, we evaluated the effects of a change in filament length with different bending stiffness values. For this part, we used repulsive force strength slightly higher than the reference level ($\kappa_{r,A} / \kappa_{r,A}^* = 3.2$) because the influences of filament length ware not obvious with the reference

strength. Like the cases explained above, a decrease in the filament length decreased the number of rings (Figs. 3.9A, B and 3.10A). By contrast, bands were observed in all tested cases. With shorter filaments, there was no noticeable change in the heterogeneity of morphology and the size of rings (Figs. 3.10B, E), but structures were less stable (Fig. 3.10D). The filament curvature tended to be smaller in cases with the shortest filaments because of less ring formation (Fig. 3.10C). Values of the velocity correlation showed a tendency to increase, and the curl of the velocity field showed lower values with shorter filament length because fewer rings and more bands were formed as filaments were shorter (Figs. 3.9C, D).
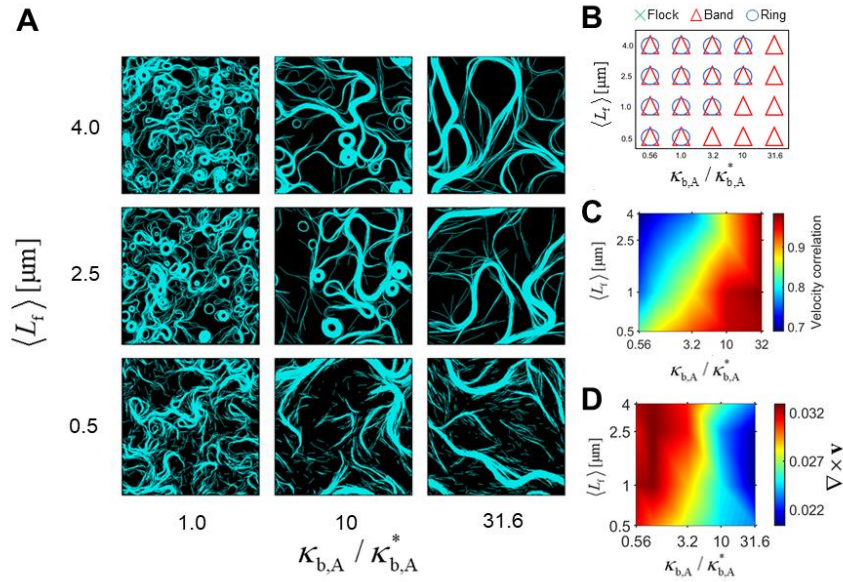
Figure 3.9. Effects of average F-actin length ($<L_f>$) and bending stiffness of F-actins ($\kappa_{b,A}$) on collective behaviors of F-actins. (A) Snapshots taken at 100 s. (B) Appearance of different kinds of structures: rings (circles), bands (triangles), and swarms (crosses). (C) Correlation of velocities of adjacent F-actins averaged between 50 s and 100 s. Larger correlation values represent greater collective behaviors of F-actins. (D) The curl of a velocity field calculated by averaging F-actin velocities. The curl values indicate the degree of rotational movements. Higher curl values imply formation of more rings.
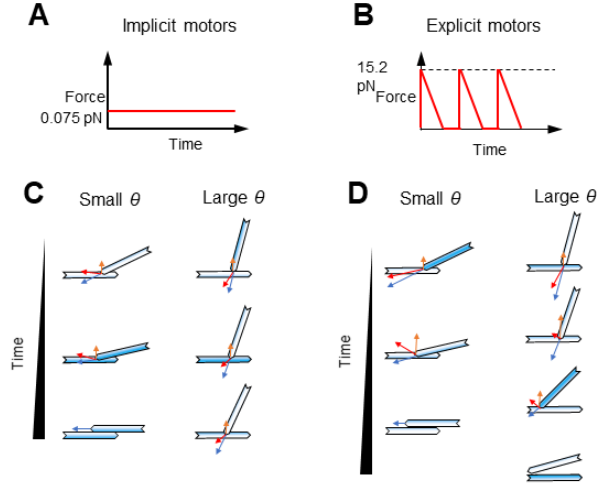
Figure 3.10. Schematic diagram of the force applied for implicit and explicit motors. (A-B) Force from myosin heads over time with implicit motors (A) and explicit motors (B). (C-D) Representation of a collusion between F-actin with implicit motors (C) and explicit motors (D).

Last, we varied filament length with various filament concentrations and slightly high repulsive force ($\kappa_{r,A} / \kappa_{r,A}^* = 3.2$). Effects of a change in the filament length was more conspicuous at low filament concentration; if average distance between filaments is long, longer filaments can have better interactions with other filaments than short filaments. As the filament length decreased, bands and rings disappeared more, and flocks emerged with an increase in the average filament curvature (Figs. 3.11A, B and 3.12A, C) although the ring size did not change noticeably (Fig. 3.12B). As results shown above, structures tended to be less stable with shorter filaments (Fig. 3.12D).
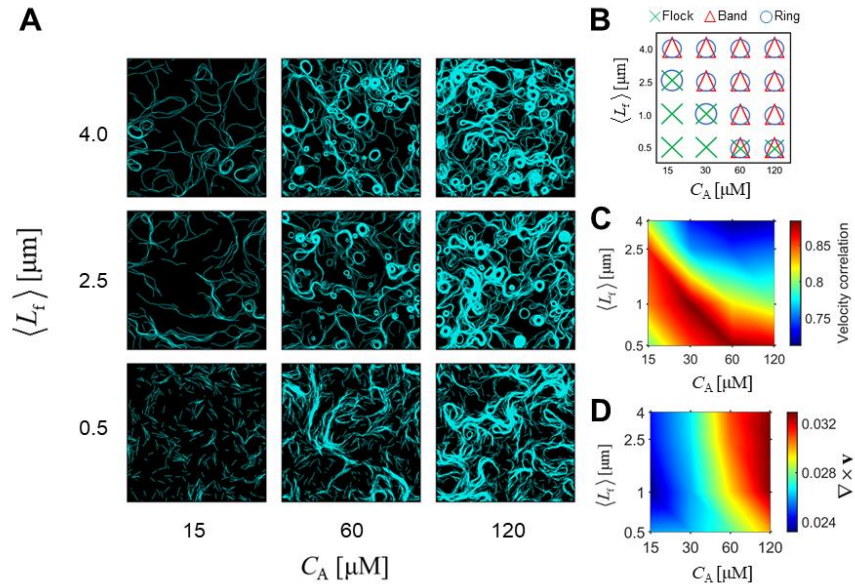
Figure 3.11. Influences of average F-actin length ($<L_f>$) and actin concentration (C_A) on collective motions of F-actins. (A) Snapshots taken at 100 s. (B) Formation of distinct types of structures: rings (circles), bands (triangles), and swarms (crosses). (C) Correlation of velocities of neighboring F-actins averaged between 50 s and 100 s. Higher correlation values mean more collective motions of F-actins. (D) The degree of rotational movements represented by the curl of a velocity field calculated by averaging F-actin velocities. Larger curl values indicate formation of more rings.
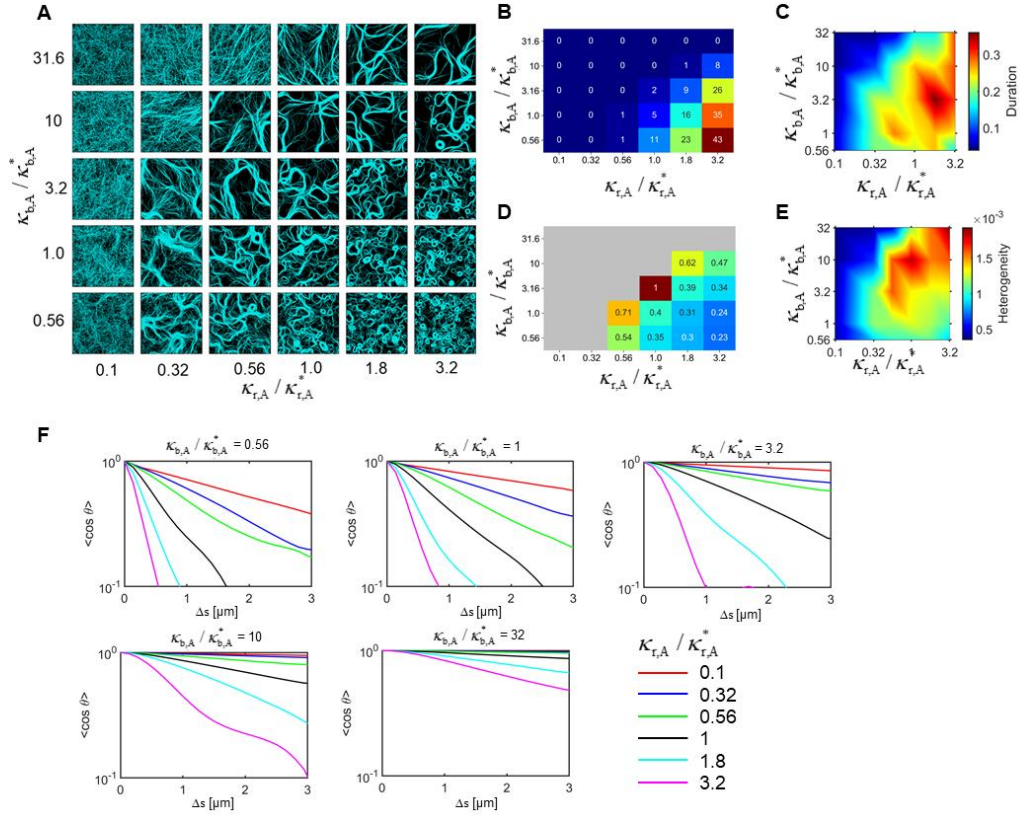
Figure 3.12. Collective behaviors of F-actin depending on bending stiffness ($\kappa_{b,A}$) and the strength of volume-exclusion effects ($\kappa_{r,A}$). (A) Snapshots taken at 100 s. (B-C) Discrete heatmap showing the number of rings that formed (B) and the normalized average ring diameter (C). (D) Heatmap showing the duration of f-actin. Higher duration values mean f-actin remain in bands longer (E) Heatmap showing the heterogeneity of f-actin. (F) Order parameter for various bending stiffness and strength of volume-exclusion effects.

3.4 Discussion

Emergence of patterns in motility assay has been widely studied in both in vitro and computational works [12, 14]. In this study, we observed all patterns observed in the previous studies, including flocks, bands, and rings. Unlike previous models [14, 97], we used explicit motors that can bind to, unbind from, and walk on filaments. We demonstrated that explicit motors can result in quite different collective behaviors of filaments from implicit motors. Using the model with explicit motors, we investigate how filaments propelled by explicit motors interact with other filaments under various conditions in order to show what governs collective behaviors. We varied two of the four parameters – the strength of repulsive forces and the bending stiffness, concentration, and length of filaments – with the other two fixed. Then, in all the possible two-

dimensional parametric spaces consisting of varied two parameters, we quantified the types, stability, and morphology of emerging structures and the curvature, velocity correlation, and rotational movements of filaments.

We found that all four parameters highly affected the extent of collective behaviors of filaments and pattern formation in different manners. The strength of repulsive forces governs how strongly filaments will be pushed away after collisions or how frequently they will cross over each other. The bending stiffness determines how easily filaments will be bent by collisions with other filaments as well as the length scale of structures. Filament concentration controls average distance between filaments, so lower concentration reduces the frequency of collision events. Filament length can make a difference in collective behaviors and pattern formation if it is very low. If filaments are too short compared to the average distance between filaments, they cannot make collisions well. In addition, with such short filaments, loop structures or long bundles are hardly formed even if filaments are aligned. Overall, it was observed that the relative importance and role of one parameter varies depending on the values of other parameters.

We found that rings and bands are formed when long filaments at high concentration experience enough volume-exclusion effects to divert them after collisions. The bands consist of a large number of tightly aligned filaments moving in a parallel or anti-parallel manner, so cases with many thick bands tended to show high velocity correlations and heterogeneous morphology. It was observed that more, smaller rings appeared when the collision-induced diversion of filaments was more severe due to either strong repulsive force or low filament rigidity. High filament concentration and length also helped ring formation. The size of rings was determined mostly by filament rigidity and the strength of volume-exclusion effects between filaments, not by the two other parameters. These rings facilitated rotational motions of filaments due to their circular shapes and also increased the velocity correlation of filaments and the heterogeneity of morphology. However, in cases with a large number of small rings, the velocity correlation and the heterogeneity were reduced. The rings and bands were very stable once they were formed, so they lasted for long time. When the diversion of filaments after collisions was not strong enough to form the bands or the rings due to high filament rigidity or too weak repulsive forces, filaments formed homogeneous networks or flocks that are loose, transient bundles. Too short filaments and too low filament concentration can also prevent filaments from forming the bands and the rings.

In such cases, filaments showed no or poor collective behaviors in terms of velocity correlations and rotational motions.

Our findings are similar to observations reported by previous studies in many aspects. Effects of the extent of volume-exclusion effects between gliding filaments on structure formation were similar to observations in [14]: homogeneous networks at weak repulsive forces, flocks at intermediate repulsive forces, and rings and bands at high repulsive forces. Rings that reached a steady state in our study are reminiscent of a frozen steady state observed in [56]. The formation of more rings with longer filaments that we showed at low filament concentration is consistent with in vitro experiments showing filament alignment is facilitated better by longer filaments [11]. Effects of filament length was also tested in the computational study [14]. In this study, filament rigidity was defined as the ratio of persistence length to filament length. They found that increasing rigidity (i.e., decreasing filament length) can induce bundle formation due to higher directional persistence of shorter filament. We also observed that an increase in the persistent movement of filaments due to either short filaments or high bending stiffness can lead to formation of large bundles rather than rings.

There are some differences between our study and previous ones. Although the in vitro study reported that filament length decreases over time due to motor-induced severing of the filaments [11], we did not observe a change in filament length during simulations because of the absence of severing events. It will be interesting to study how severing of actin filament affects collective behaviors in the future. In addition, in a previous study, swirls, which exhibit swarming flocks that can self-interact, were observed at higher filament concentration, low bending stiffness, and high repulsive force [14]. We did not observe swirls with the ranges of tested parameter values. It is possible that filaments in our simulations were not long enough to form rings and self-interact. One previous in vitro study showed that filaments in the motility assay formed millimeter-sized belt-like patterns, and the curvature of the structure is smaller with shorter filaments [80]. Although we observed that the curvature was smaller with shorter filaments, a direct comparison between our results and the previous findings is hard because of a large difference in the filament concentration; they used much higher concentration in the in vitro experiments than ours.

4. MYOSIN-DRIVEN F-ACTIN FRAGMENTATION FACILITATES CONTRACTION OF ACTIN NETWORKS

4.1 Introduction

In non-muscle cells, the actin cytoskeleton is responsible for a wide range of vital processes, such as cell migration and cytokinesis. The actin cytoskeleton is comprised of disordered actin filaments (F-actins), myosin motor proteins, actin cross-linking proteins (ACPs) that interconnect pairs of F-actins, and other actin-binding proteins. Actomyosin contractility originating from interactions between F-actin and myosin motors drives many of physiological processes [88, 98, 99]. Non-muscle myosin II, which walks toward the barbed ends of F-actins, plays the most important role in the actomyosin contractility in non-muscle cells [100-102]. Single-molecule experiments have shown that non-muscle myosin II is non-processive or weakly processive, meaning that it spends only a small fraction of its lifetime in a bound state [103, 104]. To remain bound to F-actins for a longer time, non-muscle myosin II self-assembles into a thick filament with a bipolar structure having myosin heads on both ends [105, 106]. The bipolarity of the myosin thick filament allows F-actins with opposite polarities to slide toward each other [107, 108].

To better investigate the actomyosin contractility, researchers have employed an *in vitro* minimal system consisting of purified actin, myosin II, and various types of ACPs [22, 24, 109]. Since it is hard to directly measure mechanical stress exerted on reconstituted networks, the contractile behaviors of networks have been a primary interest in the *in vitro* studies. It was shown that reconstituted actin networks exhibit spontaneous contraction into multiple small clusters (local contraction) or a single cluster (global contraction), depending on network connectivity [22, 24, 27]. Such local/global network contraction was successfully recapitulated in several computational studies [110]. With sufficient ACPs, networks could show global contraction due to superior connectivity between F-actins. However, in both experiments and simulations, it was also shown that a very large number of ACPs can inhibit network contraction by inhibiting the buckling of F-actins [27, 94]. Motor activities generate both tensile and compressive forces on F-actins, but buckling breaks the balance between the two forces by relaxing compressive forces, leading to net contraction [25]. With much higher ACP density, the length of buckling units between ACPs

becomes shorter, increasing a critical buckling force. Thus, buckling is eventually inhibited, so networks are unable to contract.

Initial network connectivity can be varied over time by the dynamics of F-actins and ACPs. Several computational studies demonstrated that the force-dependent unbinding of ACPs from F-actins is able to induce network contraction by reducing effective frictions and connections between F-actins [24]. However, if the unbinding takes place too frequently, networks hardly contract due to poor physical coupling between F-actins. This would result in the biphasic dependence of network contraction on the unbinding rate of ACPs. However, the unbinding rate of ACPs in cells or in vitro experiments does not vary significantly [111] unless the temperature of a system changes substantially unlike that of myosin motors highly influenced by ATP concentration and drugs [112]. This implies that ACP unbinding with a physiologically relevant rate may not be able to facilitate the contraction of networks with heavily cross-linked F-actins.

The other potential mechanism for the reduction of network connectivity is the fragmentation of F-actins [27, 113]. Our previous study demonstrated that F-actins can be fragmented or severed during network contraction due to an increase in their bending angle caused by buckling [27]. It was also shown that too frequent buckling-induced F-actin fragmentation can lead to the formation of multiple small clusters as a result of network contraction rather than a single large cluster because network connectivity is severely deteriorated by the fragmentation. However, this type of fragmentation occurs after network contract is initiated, so buckling-induced F-actin fragmentation cannot be a mechanism for reducing connectivity of networks with heavily cross-linked F-actins that do not spontaneously contract.

F-actins can be fragmented by a tensile force as well. A single-molecule experiment showed that F-actins are fragmented if they are subjected to large tensile forces above ~500 pN [114]. F-actins can experience such large tensile forces if numerous motors walk on F-actins tightly cross-linked to each other. Then, a small fraction of F-actins supporting the largest tensile forces may undergo fragmentation, resulting in a decrease in network connectivity. If this event occurs in series, even a network with highly cross-linked F-actins may reach a low level of connectivity sufficient for network contraction. Despite this possibility, the role of tension-induced F-actin fragmentation in network contraction has not been investigated in any of the previous studies, to our knowledge.

In this study, we employed *in vitro* reconstituted actomyosin networks and a well-established agent-based computational model to investigate the effects of force-induced F-actin fragmentation on network contraction. As a base study, we evaluated how the concentrations of motors, ACPs, and ATP affect network contraction. Then, we showed that F-actin fragmentation induced by either severing proteins or large tensile forces can lead to the contraction of an otherwise stable network.

4.2   Methods

4.2.1   Preparation of proteins

Note: This section is from Kyohei Matsuda and Junichiro Yajima at the University of Tokyo.

Actin was purified from the rabbit skeletal muscle [115]. Actin was stored in the G buffer [2 mM Tris-HCl (pH 8.0), 0.2 mM ATP, 0.2 mM $CaCl_2$, and 0.2 mM DTT] in liquid nitrogen. To prepare F-actin, G-actin was polymerized in an F buffer [5 mM Tris-HCl (pH 8.0), 1 mM $MgCl_2$, 100 mM KCl, 0.1 mM $CaCl_2$, and 0.5 mM DTT] with 10 μM rhodamine phalloidin and 100 μM ATP for 1 h at room temperature. The mixture was then centrifuged for 1 h at 355,000×g and 4°C (Optima MAX, Beckman), and the pellet was suspended in the F buffer with 1 μM ATP.

Myosin II was also purified from the rabbit skeletal muscle [115]. Myosin II was stored in 600 mM KCl and 1 mM DTT in liquid nitrogen. To create myosin II thick filaments, myosin II was diluted in the assay buffer [50 mM PIPES-Na (pH 7.4), 50 mM KCl, 1 mM $CaCl_2$, 1 mM $MgCl_2$, and 1 mM EGTA] at room temperature (24 ± 1 °C). The final buffer contained 33 mM PIPES-Na, 233 mM KCl, 0.66 mM $CaCl_2$, 0.66 mM $MgCl_2$ and 0.66 mM EGTA.

Recombinant human anillin was prepared as follows [111]. First, coding sequence of the mfGFP was attached to the 3′ end of the human anillin 231-711 amino acid. The construct encoding anillin was cloned into pColdIII vector. The pColdIII-anillin-GFP were next transformed into *Escherichia coli* BL21 Star (DE3) cells. Anillin was expressed for 24 h at 15°C. Expressed proteins were purified by immobilized metal affinity chromatography using a HisTrap HP column (Cytiva) and then further purified using gel filtration chromatography (Superose 6, Cytiva) and stored in liquid nitrogen.

Recombinant human gelsolin was prepared as follows. First, a hexa histidine-tag was attached to the 3′ end of human gelsolin DNA sequence [116]. The gelsolin-His construct was cloned into pCold III vector for expression in *Escherichia coli* BL21 Star (DE3) cells. The pCold-gelsolin-His was next transformed into the cell. Gelsolin-His was expressed for 24 h at 15°C; the cells were collected by centrifugation and resuspended in a lysate buffer [20 mM imidazole-HCl, 300 mM KCl, 1 mM DTT, and 10 mM $CaCl_2$] containing the protease inhibitor cocktail (Roche), and sonicated for 20 min on ice. Next, the lysate was centrifuged for 20 min at 305,000×g and at 4°C. Ni-NTA resin (Bio-Rad) was added, and the mixture was gently stirred for 1 h at 4°C. The Ni-NTA beads were washed with a buffer [20 mM imidazole-HCl, 300 mM KCl, 1 mM DTT and 10 mM $CaCl_2$] by centrifuging several times. Gelsolin-His was then eluted with another buffer [200 mM imidazole-HCl, 300 mM KCl, 1 mM DTT and 10 mM $CaCl_2$], desalted on a NAP5-culumn (Cytiva), and stored in a gelsolin buffer [10 mM Tris-HCl (pH 7.4), 10 mM $CaCl_2$, 150 mM NaCl, 1mM DTT and 50 μM ATP] in liquid nitrogen.

4.2.2   Estimation of concentrations of proteins

Note: This section is from Kyohei Matsuda and Junichiro Yajima at the University of Tokyo.

The concentrations of actin, meromyosin, and myosin were estimated based on ultraviolet absorbance of their solution. We used the absorption coefficients of full-length myosin II (A_{280nm} = 0.53 /mg/ml/cm), heavy-meromyosin (HMM) (A_{280nm} = 0.6 /mg/ml/cm), and G-actin (A_{290nm} = 0.63 /mg/ml/cm) and also used molecular masses of full-length myosin II (470 kDa), HMM (350 kDa), and G-actin (42 kDa). The concentrations of anillin and gelsolin were estimated by SDS-PAGE on 10% acrylamide gels using BSA standards (Thermo Scientific) loaded on the same gel. Gels were stained with Quick-CBB PLUS (Wako) and imaged using a CCD camera (CSFX36BC3, Toshiba). The bands containing anillin, gelsolin, and BSA standards were quantified using ImageJ (NIH).

4.2.3   Microscope images of F-actin

Note: This section is from Kyohei Matsuda and Junichiro Yajima at the University of Tokyo.

F-actins were observed using a fluorescence microscope (IX70, Olympus) with a stable stage (KS-N, ChuukoshaSeisakujo) and a stage controller (QT-CM2-35, Chuo Precision Industrial) with illumination from a mercury lump (U-HGLGPS, Olympus); 20×/ NA, UPlanFl objective lens (Olympus); and U-MWIG filter set (Olympus). Images were recorded by sCMOS camera (Zyla 4.2 PLUS USB3.0, Andor). Shutter was controlled using SSH-C (Sigma-koki). In the actin fragmentation assay, 100×/ NA 1.40 oil immersion UPlanApo objective lens (Olympus) was used.

4.2.4 Actomyosin network contraction assay

Note: This section is from Kyohei Matsuda and Junichiro Yajima at the University of Tokyo.

In the network contraction assay, G-actin, skeletal muscle myosin II thick filaments, and ACPs were mixed and self-organized into a disordered actin network. For ACPs, we employed anillin that is known to be localized at a contractile ring during cytokinesis [117]. The formation of actomyosin networks was initiated by mixing myosin II thick filaments, anillin, and G-actin (3 μM) in an assay buffer [50 mM PIPES-Na (pH 7.4), 50 mM KCl, 1 mM $CaCl_2$, 1 mM $MgCl_2$, and 1 mM EGTA] containing 2 mg/ml BSA, 1.0 μM rhodamine phalloidin, 0.5 mM DTT, and various concentrations of ATP. To prevent photobleaching, 0.2% catalase, 1.5 mg/ml glucose, and 50 U/ml glucose oxidase as the oxygen scavenger were added [116]. To maintain constant ATP concentration in the assay, 20 mM creatine phosphate and 0.3 mg/ml creatine kinase were added to the solution as an ATP regenerating system [116]. The assay was performed in flow chambers assembled from two coverslips, 18×18 mm and 24×36 mm (Matsunami), attached via a double-sided tape (NW-25, Nichiban). The glass surface was blocked with 2 mg/ml BSA to prevent glass-protein interactions. The assay mixture was placed in the chamber, and the observation commenced 30 s after mixing. For the assay, both ends of the chamber were sealed with nail polish. Images of F-actins were recorded as described above, every 10 s, with 0.5-s exposure time (Fig. 4.1).
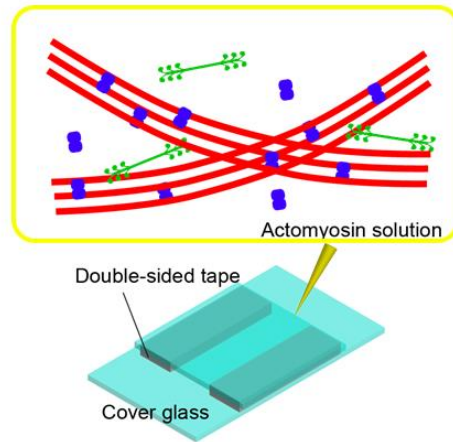
Figure 4.1. A schematic diagram explaining the setup of in vitro experiments. The assay was performed in flow chambers assembled with two coverslips, 18×18 mm and 24×36 mm, attached via a double-sided tape. Formation of actomyosin networks was initiated by mixing actin (red), myosin minifilaments (green), and anillin (blue) in an assay buffer [50 mM PIPES-Na pH 7.4, 50 mM KCl, 1 mM $CaCl_2$, 1 mM $MgCl_2$, and 1 mM EGTA] containing 2 mg/ml BSA, 1.5 μM rhodamine phalloidin, 0.5 mM DTT, and various ATP concentrations of ATP in the presence of the ATP-regenerating system. Note: This figure is from Kyohei Matsuda and Junichiro Yajima at the University of Tokyo.

To confirm that anillin does not induce network contraction by itself, we performed experiments with various concentrations of anillin without myosin II thick filaments. With R_A (the ratio of anillin concentration to actin concentration) = 0.1 or 0.2, morphology of networks remains homogenous with uniform meshes, whereas relatively heterogeneous networks with bundles were formed with $R_A = 0.3$. However, as expected, cluster formation was not observed in these passive networks without myosin II thick filaments (Fig. 4.2).
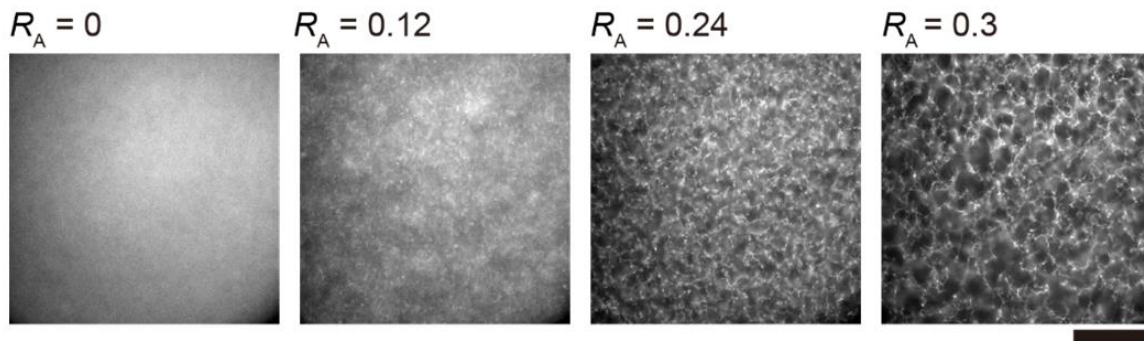
Figure 4.2. Actin networks with various densities of anillin in the absence of myosin. Networks were assembled with G-actin (3 µM), rhodamine phalloidin (1 µM), anillin (R_A = 0-0.3), and ATP (1 mM) without the ATP-regenerating system. A scale bar indicates 100 µm. Without anillin, F-actins exist as individual filaments, so they are hardly visible in the image. With intermediate anillin density (R_A = 0.12 and 0.24), cross-linked actin networks with homogenous meshes were formed. With the highest anillin density (R_A = 0.3), a highly bundled network was formed. Note: This figure is from Kyohei Matsuda and Junichiro Yajima at the University of Tokyo.

4.2.5   Measurement of myosin II thick filament length using electron microscopy

Note: This section is from Kyohei Matsuda and Junichiro Yajima at the University of Tokyo.

A 10-nM myosin II thick filament solution was applied onto carbon-coated copper grids and negatively stained with 1.0% (w/v) uranyl acetate [118]. The specimens were examined using an electron microscope (Hitachi High-Technologies, H-7500) operated at 80 kV with magnification of 12,000× (Fig. 4.3A, B). The length of myosin thick filaments was evaluated visually by using the built-in "segmented-line" tool in ImageJ.
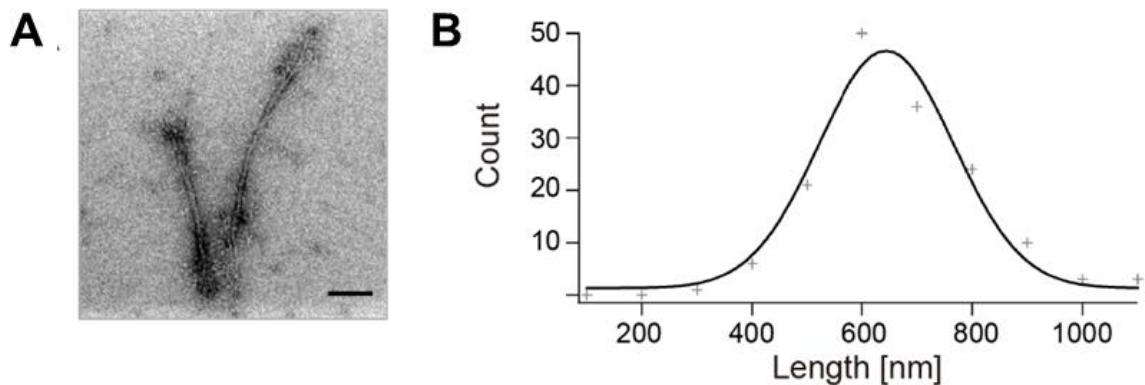
Figure 4.3. Measurement of the length of myosin minifilaments. (A) An electron microscopy image showing two negatively stained myosin minifilaments. A scale bar indicates 100 nm. (B) Distribution of the length of 154 myosin minifilaments. The mean and standard deviation were derived from a Gaussian fitting. Note: This figure is from Kyohei Matsuda and Junichiro Yajima at the University of Tokyo.

4.2.6   Triggering network contraction via addition of gelsolin

Note: This section is from Kyohei Matsuda and Junichiro Yajima at the University of Tokyo.

To induce fragmentation of F-actins in a prestressed network, 1 μl of 0.02-0.20 μM gelsolin diluted in a gelsolin buffer [10 mM Tris-HCl (pH 7.4), 10 mM $CaCl_2$, 150 mM NaCl, 1mM DTT, and 50 μM ATP] was loaded into the glass chamber. The final concentration of gelsolin was 0.002-0.020 μM. Images were recorded by sCMOS camera every 10 s, with 0.5-s exposure time.

4.2.7   Assay for observation of myosin-induced F-actin fragmentation in networks

Note: This section is from Kyohei Matsuda and Junichiro Yajima at the University of Tokyo.

To better observe F-actin fragmentation induced by myosin, a network with partly labeled actin was prepared, containing 3 μM G-actin, 1 μM dark phalloidin, 0.1% rhodamine-labeled F-actin, 0.5 μM anillin-GFP, 1 μM myosin II thick filament, the oxygen scavenger, 2 mg/ml BSA,

92

and 1 mM ATP in the assay buffer. The images of partly labeled F-actins were recorded as described above, every 2 s with 0.5-s exposure time. The retracting speed of fragmented F-actins was quantified using an automated tracking program Mark2 (Ken'ya Furuta, NICT). Fluorescence images of F-actin fragments were fitted using a 2D Gaussian function to determine the position of the fluorescence intensity peak, corresponding to the center of the fragments [119]. Displacements of the actin fragments were calculated using the x and y coordinates of the fragments in each frame. The speed was calculated based on displacement for a time interval of 10 s corresponding to five frames.

4.2.8　Agent-based computational model for simulating network contraction

To simulate the contraction of actomyosin networks, we used the agent-based model built introduced in Chapter 2 and used in our previous studies [27, 61-63]. Parameter values are listed in Table 4.1 and 4.2. Many of the parameter values employed in simulations are inherited from our previous studies which recapitulated a wide variety of the contractile behaviors of actin networks [61, 62].

Table 4.1. List of parameters employed in the model.

Symbol	Definition	Value
$r_{0,\mathrm{A}}$	Length of an actin segment	1.4×10^{-7} [m]
$r_{\mathrm{c,A}}$	Diameter of an actin segment	7.0×10^{-9} [m] [69]
$\theta_{0,\mathrm{A}}$	Bending angle formed by adjacent actin segments	0 [rad]
$\kappa_{\mathrm{s,A}}$	Extensional stiffness of F-actin	1.69×10^{-2} [N/m]
$\kappa_{\mathrm{b,A}}^{*}$	Reference bending stiffness of F-actin	2.64×10^{-19} [N·m] [70]
$r_{0,\mathrm{ACP}}$	Length of an ACP arm	2.35×10^{-8} [m] [71]
$r_{\mathrm{c,ACP}}$	Diameter of an ACP arm	1.0×10^{-8} [m]
$\theta_{0,\mathrm{ACP}}$	Bending angle formed by two ACP arms	0 [rad]
$\kappa_{\mathrm{s,ACP}}$	Extensional stiffness of ACP	2.0×10^{-3} [N/m]
$\kappa_{\mathrm{b,ACP}}$	Bending stiffness of ACP	1.04×10^{-19} [N·m]
$r_{0,\mathrm{M}}$	Length of a motor arm	1.35×10^{-8} [m]
$r_{\mathrm{c,M}}$	Diameter of a motor arm	1.0×10^{-8} [m]
$\kappa_{\mathrm{s,M}}$	Extensional stiffness of a motor arm	1.0×10^{-3} [N/m]
k_{20}^{*}	Reference ATP-dependent unbinding rate of myosin heads	20 [s^{-1}]
N_{h}	Number of heads represented by a motor arm	8
N_{a}	Number of arms in a motor	4
$k_{\mathrm{n,A}}$	Nucleation rate of actin	$0.000125 - 1$ [μM^{-1}s^{-1}]
$k_{+,\mathrm{A}}$	Polymerization rate of actin at the barbed end	60 [μM^{-1}s^{-1}]
$k_{\mathrm{u,ACP}}^{0*}$	Reference zero-force unbinding rate constant of ACP	0.115 [s^{-1}] [68]
$\lambda_{\mathrm{u,ACP}}$	Sensitivity of ACP unbinding to an applied force	1.04×10^{-10} [m] [68]
$\kappa_{\mathrm{r,A}}$	Strength of a repulsive force	1.69×10^{-3} [N/m]
Δt	Time step	1.15×10^{-5} [s] or 2.875×10^{-6} [s]
μ	Viscosity of surrounding medium	8.6×10^{-1} [kg/m·s]
$k_{\mathrm{B}}T$	Thermal energy	4.142×10^{-21} [J]
C_{A}	Actin concentration	100 [μM]
R_{M}	Motor density (= Ratio of motor concentration to C_{A})	$0.008 - 0.8$
R_{ACP}	ACP density (= Ratio of ACP concentration to C_{A})	$0 - 0.1$
$<L_{\mathrm{f}}>$	Average length of F-actins	$0.69 - 3.02$ [μm]

Table 4.2. List of parameter values used for adopting "parallel cluster model." [72, 73]

Symbol	Definition	Value
k_{01}	A rate from unbound to weakly bound state	40 [s^{-1}]
k_{10}	A rate from weakly bound to unbound state	2 [s^{-1}]
k_{12}	A rate from weakly bound to post-power-stroke state	1000 [s^{-1}]
k_{21}	A rate from post-power-stroke to weakly bound state	1000 [s^{-1}]
k_{20}	A rate from post-power-stroke to unbound state	5-640 [s^{-1}]
F_0	Constant for force dependence	5.04×10^{-12} [N]
E_{pp}	Free energy bias toward the post-power-stroke state	-60×10^{-21} [J]
E_{ext}	External energy contribution	0 [J]
d	Step size	7×10^{-9} [m]
k_m	Spring constant of the neck linkers	1.0×10^{-3} [N/m] (= $\kappa_{s,M}$)

Briefly, F-actin, motor, and ACP in the model are coarse-grained by interconnected cylindrical segments (Fig. 4.4A). F-actins consist of serially connected segments with polarity (i.e., barbed and pointed ends). ACPs are comprised of two arm segments connected at their center point. Each motor consists of a backbone structure with 8 arms, mimicking the geometry of myosin II thick filaments. Each motor arm represents 8 myosin heads kinetically. The displacements of all the cylindrical segments at each time step are determined using the Langevin equation. The model accounts for extensional and bending forces that maintain equilibrium distances and angles formed by cylindrical segments, respectively, as well as a repulsive force representing volume-exclusion effects between neighboring actin segments.
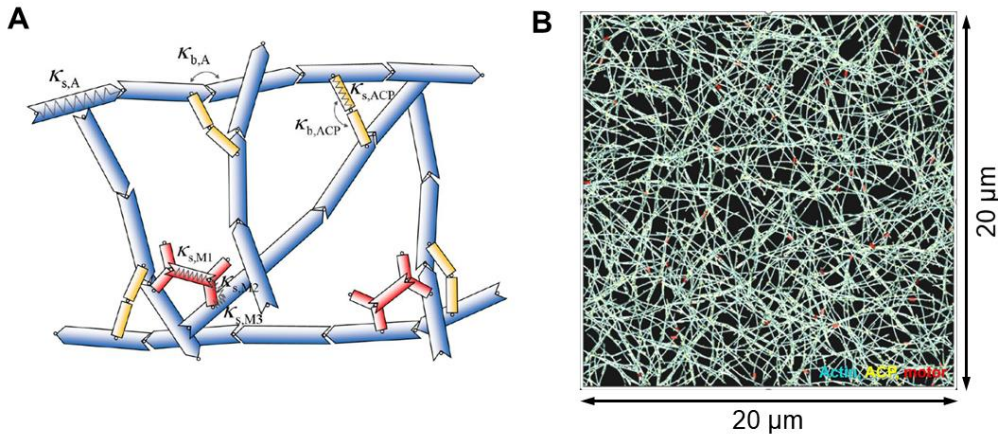
Figure 4.4. Agent-based computational model. (A) A schematic diagram showing an actomyosin network consisting of F-actin (blue), motor (red), and ACP (yellow) simplified by interconnected cylindrical segments. F-actins are coarse-grained by serially connected segments with barbed and pointed ends. ACPs consist of two arm segments. Each motor is comprised of a backbone structure with motor arms. One motor arm represents eight myosin heads kinetically. (B) An example of an actomyosin network assembled in a thin computational domain (20×20×0.1 µm) with the periodic boundary condition in the x and y directions.

A network is formed in a thin computational domain (20×20×0.1 µm) with the periodic boundary condition in the x and y directions (Fig. 4.4B). A repulsive boundary condition is applied in the z-direction. During network formation, actin undergoes slow nucleation and relatively fast polymerization events to form F-actins. ACPs can bind to a pair of F-actins at a constant rate to form functional cross-links and also unbind from F-actins in a force-dependent fashion obeying Bell's law [67]. Motor arms self-assemble into a thick filament and then bind to F-actin without walking motion. After the network assembly, motors start walking toward the barbed end of F-actins, based on the mechanochemistry rates of myosin II. In part of simulations, it is assumed that F-actin is fragmented in a deterministic manner if it is subjected to a tensile force greater than 500 pN [114].

4.2.9   Quantification of network contraction in experiments and simulations

To evaluate how fast networks contract, contraction speed was calculated in experiments as follows. First, background intensity was subtracted using a built-in "subtract background" plugin in ImageJ. We binarized fluorescence images of actin networks using the ImageJ threshold-

96

plugin (Fig. 4.5A, B). In binarized images, we calculated the total area occupied by actin and plotted the total area over time (Fig. 4.5C). An increase in the total area at early times indicates network formation, whereas a decrease in the total area at later times is indicative of network contraction. A linear fit was used to estimate contraction speed in a contraction regime (Fig. 4.5C). In addition, to represent how fast F-actins are displaced during contraction, we calculated the average of the magnitude of moving speeds that were estimated via the PIV plug-in in ImageJ (Fig. 4.5D, E). We also quantified the maximum cluster size as follows. First, background intensity was subtracted in the same way. To determine cluster size, a built-in "analyze particle" plugin in ImageJ was used. We define clusters as an actin structure with intensity higher than 150 a.u. and with a long axis shorter than 200 μm. Maximum cluster size was defined as the size of the largest cluster size in the final image in the entire glass chamber area.
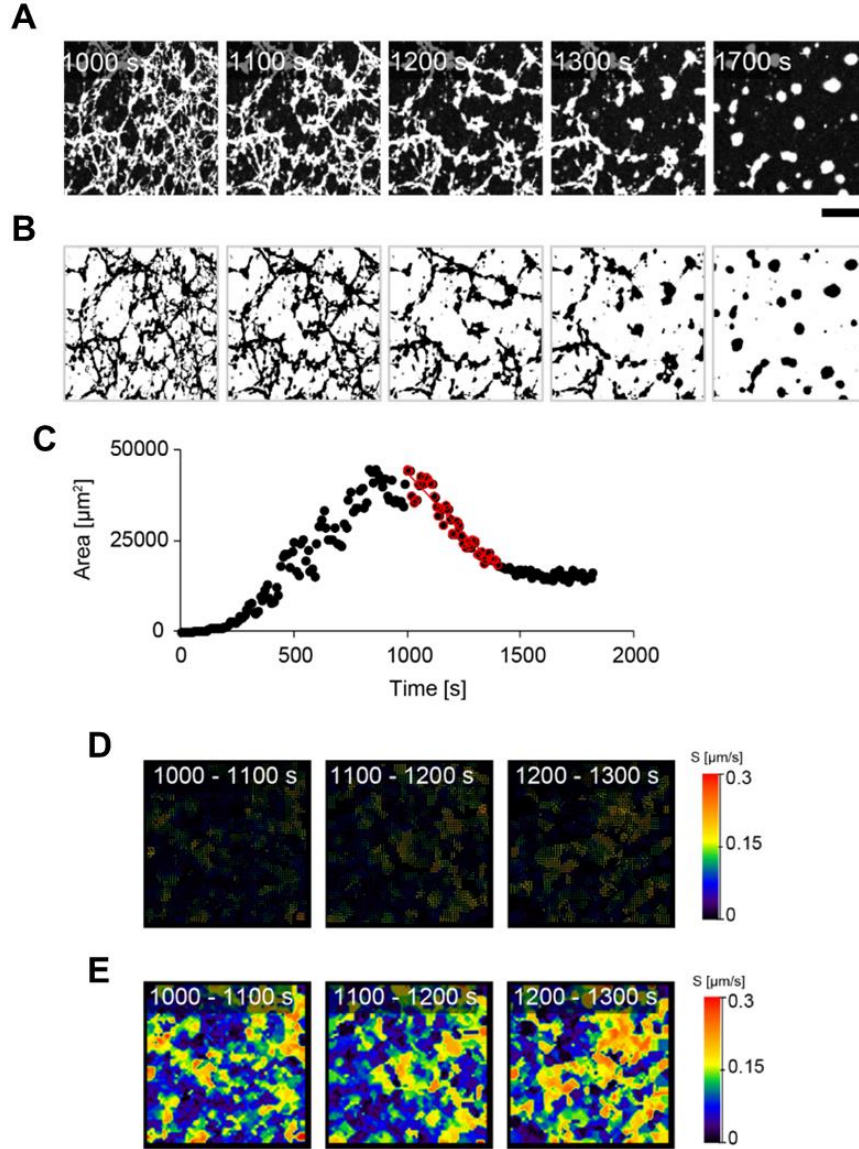
Figure 4.5. Quantification of contractile behaviors of networks. (A-C) Estimation of contraction speed. (A) Time-lapse images taken during network contraction. F-actins are shown in white. (B) Binarization of the time-lapse images using the ImageJ threshold plug-in. (C) Time evolution of the total area in black in the binarized images. An initial increase in the area indicates formation of a network ($0 - 1000$ s), whereas a decrease in the area at later times means network contraction ($1000 - 1300$ s). Contraction speed was determined from a linear fit to the decreasing part after reaching the peak. (D-E) Estimation of moving speed. (D) Speed vector plots drawn via the ImageJ PIV plug-in. (E) Plots showing the magnitudes of velocity vectors. The average of the magnitudes is considered to be moving speed. Note: This figure is from Kyohei Matsuda and Junichiro Yajima at the University of Tokyo.

Network contraction speed in simulations was measured in a similar manner. Images in simulations showing the positions of F-actins at each time point were used to calculate the area of the network (Fig. 4.6A). Each image was divided into 70×70 grids. The area is defined as the number of grids that are occupied by more than one actin segment, divided by total number of grids. The average decreasing rate of area for first 8 s was used as network contraction speed. Ensemble- and time-averaged speed of each actin segment for first 8 s was used as moving speed. Due to the computational cost, we used 20 μm as a domain width in simulations which is much smaller than the width of observed area in the experiments, ~300 μm. Due to such a difference in length-scales, we observed many simulations where networks contract into a single connected network, whereas experiments often show network contraction into multiple separate clusters. In the connected networks observed from simulations, we identified regions with much higher actin density compared to other regions and considered them to be clusters. To detect the clusters, we employed images used for the area calculation (Fig. 4.4A). Then, we filtered the images by excluding grids where the number of actin segments is smaller than 3 times the average number of actin segments per grid. (Fig. 4.6B). K-means clustering was used to detect clusters in the filtered image (Fig. 4.6C) [120]. If more than one grid are adjacent to each other, they are treated as one cluster by finding all grids along the boundary of those neighboring grids (Fig. 4.6D, E). If the boundary grids from two clusters overlap with each other, the two clusters are merged and treated as a single cluster (Fig. 4.6F).
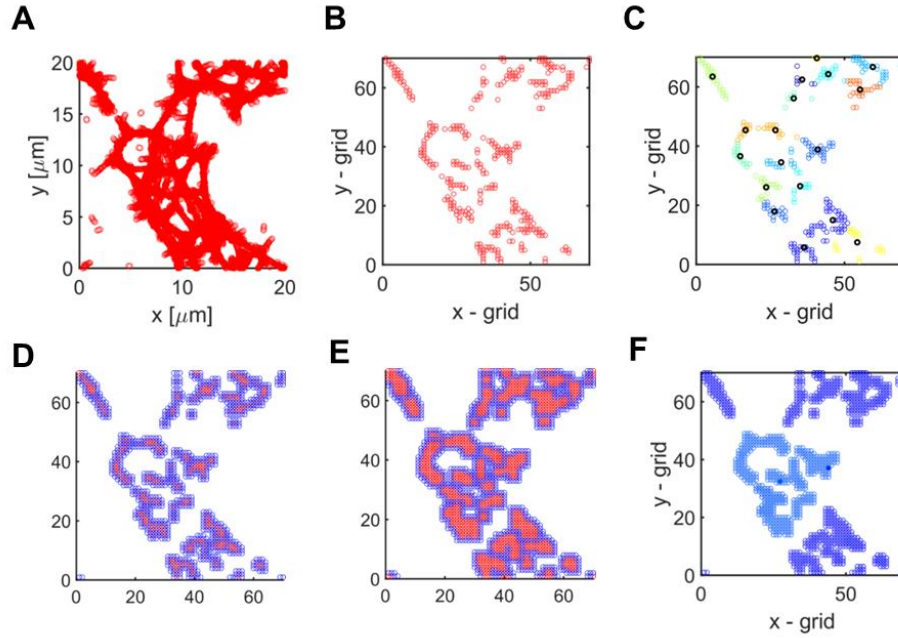
Figure 4.6. Quantification of network area and cluster number in simulation. (A) Network was divided by 70 by 70 grids. A grid is considered filled (red circle) if there is a single or more actin in a grid. Then the area of the network at a given timepoint was determined as (number of filled grids)/(number of total grids) (B) A grid was considered filled (red circle) if the number of actins in the grid is higher than 3×(Total number of actins in the network)/(Total number of grids) and considered empty if not. (C) K-means clustering was used to detect clusters in (B). Different colors represent different clusters. Black circle represents the center of each cluster. (D) Grids surrounding filled grids from (B) were found. Red circle represents filled grids from (B) and blue circle represents surrounding grids. (E) Grids surrounding filled grids from (D) were found. Red circle represents filled grids from (C) and blue circle represents surrounding grids. (F) If there is an overlap between surrounding grids from two clusters, the clusters are combined. Then, number of clusters is found. Different colors represent different clusters.

4.3   Results

To investigate network contraction driven by the actomyosin contractility, we conducted in vitro experiments and computer simulations. Note that there are notable differences in two approaches, in terms of system size, average filament length, and mechanochemistry of motors. Despite the difference, we acquired qualitatively similar results and will present them together to discuss similarities and differences between experiments and simulations.

4.3.1 ACPs modulates network contraction by varying connectivity between F-actins

Using the network contraction assay, we conducted experiments with myosin II (1 μM) and various anillin densities (R_A) in the presence of ATP (100 μM) and ATP-regenerating system. Distinct self-organizing structures resulting from myosin activity at different length-scales were reproducibly observed (Figs. 4.7A and 4.8A, B), which is consistent with previous experiments [24] and theoretical studies [27, 84]. With a moderate amount of anillin (R_A = 0.033-0.1), a cross-linked actin network is broken into multiple clusters with mean maximum cluster size ranging between 100 μm^2 and 1000 μm^2 (Fig. 4.7A, B). With a large amount of anillin (R_A = 0.2), a network was condensed into multiple large clusters with mean maximum cluster size greater than 1000 μm^2 (Fig. 4.7A, B). When there was an excessive amount of anillin (R_A = 0.3), network contraction hardly occurred. We observed that time required for reaching the steady state is longer if the final cluster size is larger. However, it typically takes less than 1 h to reach the steady state after proteins are mixed. In addition, with higher R_A, clusters were formed more slowly as indicated by lower contraction and moving speeds of actins (Fig. 4.7C). However, the probability of contraction and cluster formation was lower because it is harder for motors to break highly cross-linked networks into clusters (Fig. 4.8C), which is consistent with previous studies [94, 110].
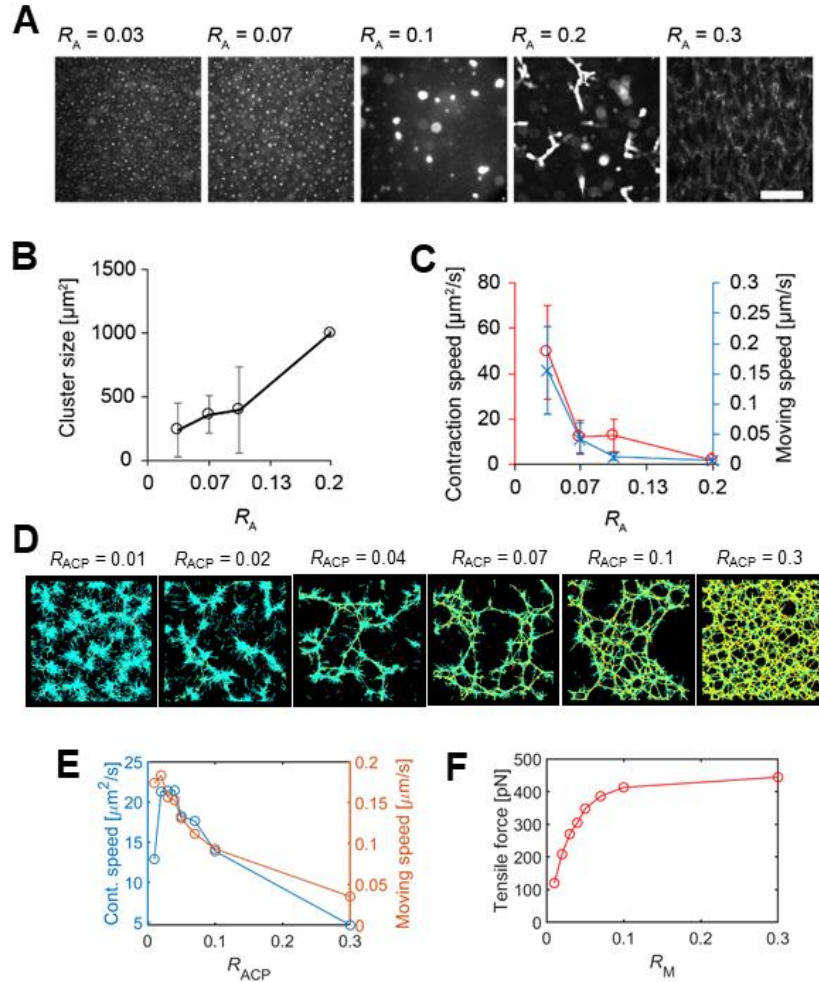
Figure 4.7. Network contraction depending on density of actin cross-linking proteins (ACPs). (A-C) Results from experiments G-actin (3 μM), myosin ($R_M = 0.33$), anillin ($R_A = 0.03$-0.3), ATP (100 μM), and the ATP-regenerating system. (A) Representative fluorescence microscope images of networks with various R_A. A scale bar corresponds to 100 μm. (B, C) Cluster size, contraction speed, and moving speed depending on R_A (0.03-0.2). (D-F) Results from simulations with actin (100 μM) motor ($R_M = 0.16$), and ACPs ($R_{ACP} = 0.01$-0.3). (D) Network morphology in simulation at 15s depending on R_{ACP} with $R_M = 0.16$. Actins (cyan), myosin motors (red), and ACPs (yellow) are shown. (E) Contraction speed, and moving speed depending on R_{ACP}. Data during initial 8s was used to calculate contraction speed and moving speed. In both experiments and simulations, networks show slower contraction into larger clusters as crosslinker density increases. (F) Average tensile force exerting on selected actin segments. Throughout simulation, ten actin segments with highest tensile force were selected. Note: (A)-(C) are from Kyohei Matsuda and Junichiro Yajima at the University of Tokyo.
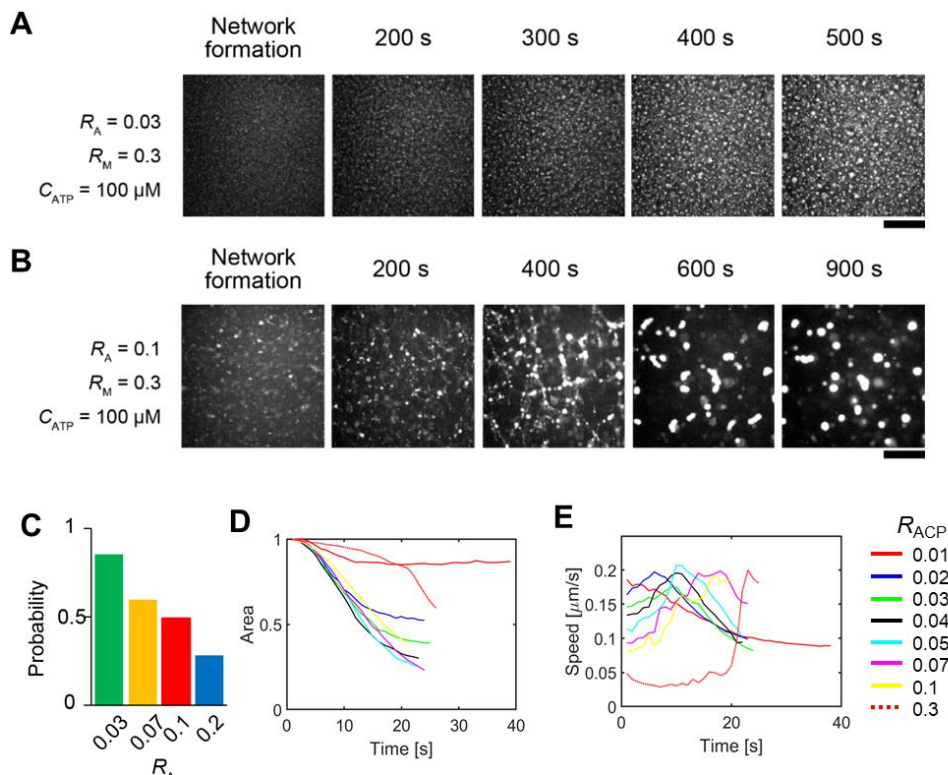
Figure 4.8. Network contraction depending on density of actin cross-linking proteins (ACPs). (A-B) Representative time-lapse images of networks prepared under two different conditions correspond to two cases in Fig. 4.7A. A scale bar indicates 100 μm. (C) The probability of cluster formation. The probability is calculated as the ratio of the number of experiments with cluster formation to the total number of performed experiments. The probability is calculated with a variation in anillin density. R_A is 0.033 (green), 0.067 (yellow), 0.1 (red), and 0.2 (blue). (D) Change of area covered by clusters over time. (E) Ensemble average of actin speed as a function of time. Note: (A)-(C) are from Kyohei Matsuda and Junichiro Yajima at the University of Tokyo.

We also used the computational model to run simulations with various ACP densities (R_{ACP}) with other parameter values fixed. When ACP density was very low, many loose clusters were formed with short distance between them, indicative of low contractility (Fig. 4.7D). With such low cross-linking density, the long-range transmission of forces generated by motors is prohibited, so local contraction occurs. As ACP density increases, fewer, tight clusters were formed as a result of strong contractility. However, if there are too many ACPs, network contraction was inhibited as observed in our experiments, so clusters did not emerge. With more ACPs, actins tended to move slower and networks contracted more slowly due to the high network connectivity except in the case with the lowest R_{ACP} (Figs. 4.7E and 4.8D, E). If the cross-linking density is too low, network contraction and F-actin movements are hard to be significant due to

103

inefficient transmission of force generated by motors. Network connectivity can also be enhanced by an increase in average length of F-actins. When average filament length ($<L_f>$) was increased, network contraction slowed down as well (Fig. 4.9).
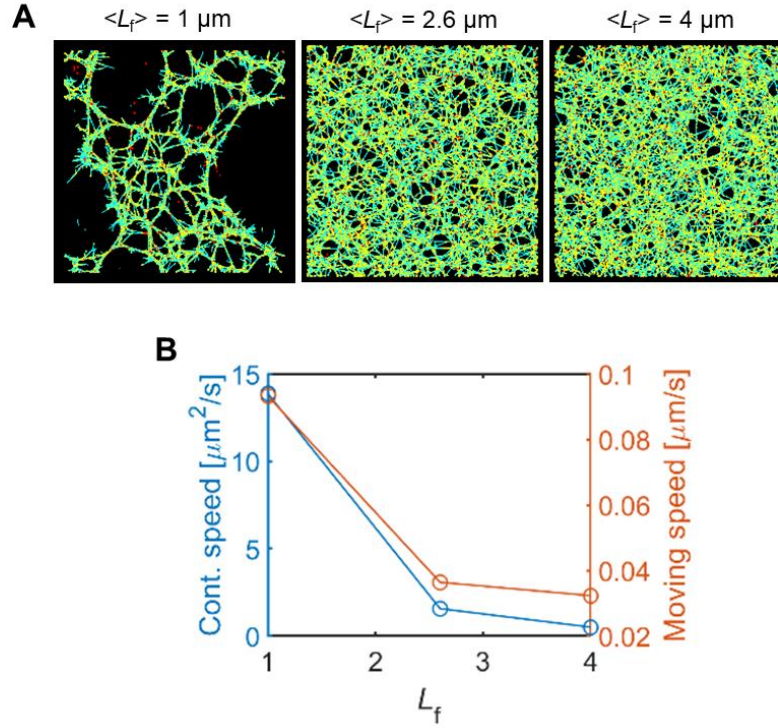
Figure 4.9. Effects of filament length on network contraction. (E) Network morphology in simulation at 15 s depending on filament length. Actins (cyan), myosin motors (red), and ACPs (yellow) are shown. (B) Contraction speed and moving speed depending on filament length. With shorter filament length, networks contract more rapidly.

4.3.2   A larger amount of motors enables a network to contract faster into larger clusters

To understand the effects of myosin-driven force generation on network contraction, we performed experiments with different molar ratios of myosin (R_M) and four different anillin density (R_A) in the presence of G-actin (3 μM), ATP (100 μM), and ATP-regenerating system. With higher R_M, networks contracted to larger clusters at a faster rate with faster F-actin movements (Fig. 4.10A-D). As explained earlier, a network cross-linked by more anillin (i.e., higher R_A) exhibited slower contraction into larger clusters, regardless of R_M. With higher R_M, the probability of cluster formation was higher because a larger number of myosins can generate larger forces required for breaking down a well cross-linked network into clusters (Fig. 4.11A). In general, with more anillin,

more myosin motors were necessary to transform the network into clusters. However, with the largest amount of myosins and anillin ($R_M = 0.67$, $R_A = 0.2$), the probability of cluster formation was quite low because the critical buckling force could be very large with such high R_A.
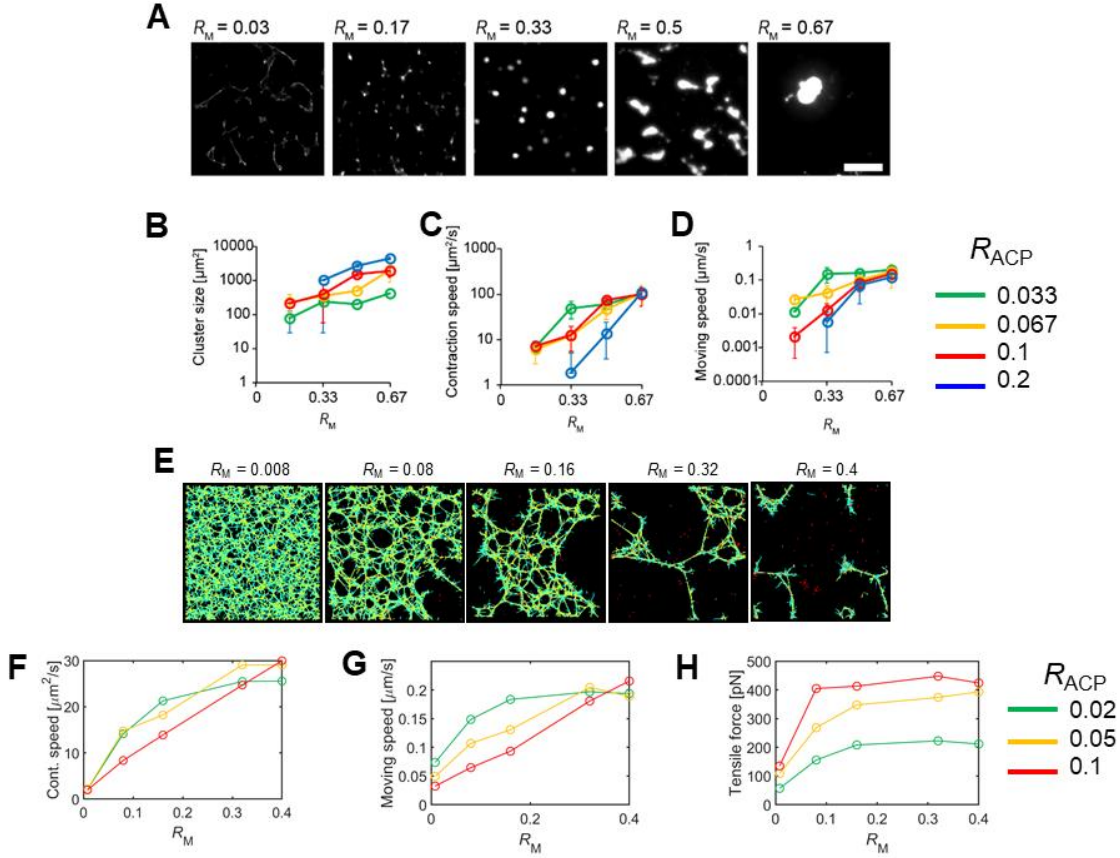
Figure 4.10. Effects of density of motors (R_M) on network contraction at various anillin density. (A-D) Results from experiments G-actin (3 μM), myosin ($R_M = 0.03$-0.67), anillin ($R_A = 0.03$-0.2), ATP (100 μM), and the ATP-regenerating system. (A) Representative fluorescence microscope images of networks with various R_M at $R_A = 0.1$. A scale bar indicates 100 μm. (B-D) Dependence of cluster size, contraction speed, and moving speed on R_M at $R_A = 0.03$ (green), 0.07 (orange), 0.1 (red), and 0.2 (blue). (E-G) Results from simulations with F-actin (100 μM), motor ($R_M = 0.008$-0.4), and ACP ($R_A = 0.1$). (E) Network morphology in simulation 15s depending on R_M with $R_{ACP} = 0.1$. Actins (cyan), myosin motors (red), and ACPs (yellow) are shown. (F) Contraction speed, and (G) moving speed depending on R_M. In both experiments and simulations, with more motors, networks contract into larger clusters more rapidly. Data at initial 8s was used to calculate contraction speed and moving speed. (H) Average tensile force exerting on selected actin segments. Throughout simulation, ten actin segments with highest tensile force were selected. Note: (A)-(D) are from Kyohei Matsuda and Junichiro Yajima at the University of Tokyo.
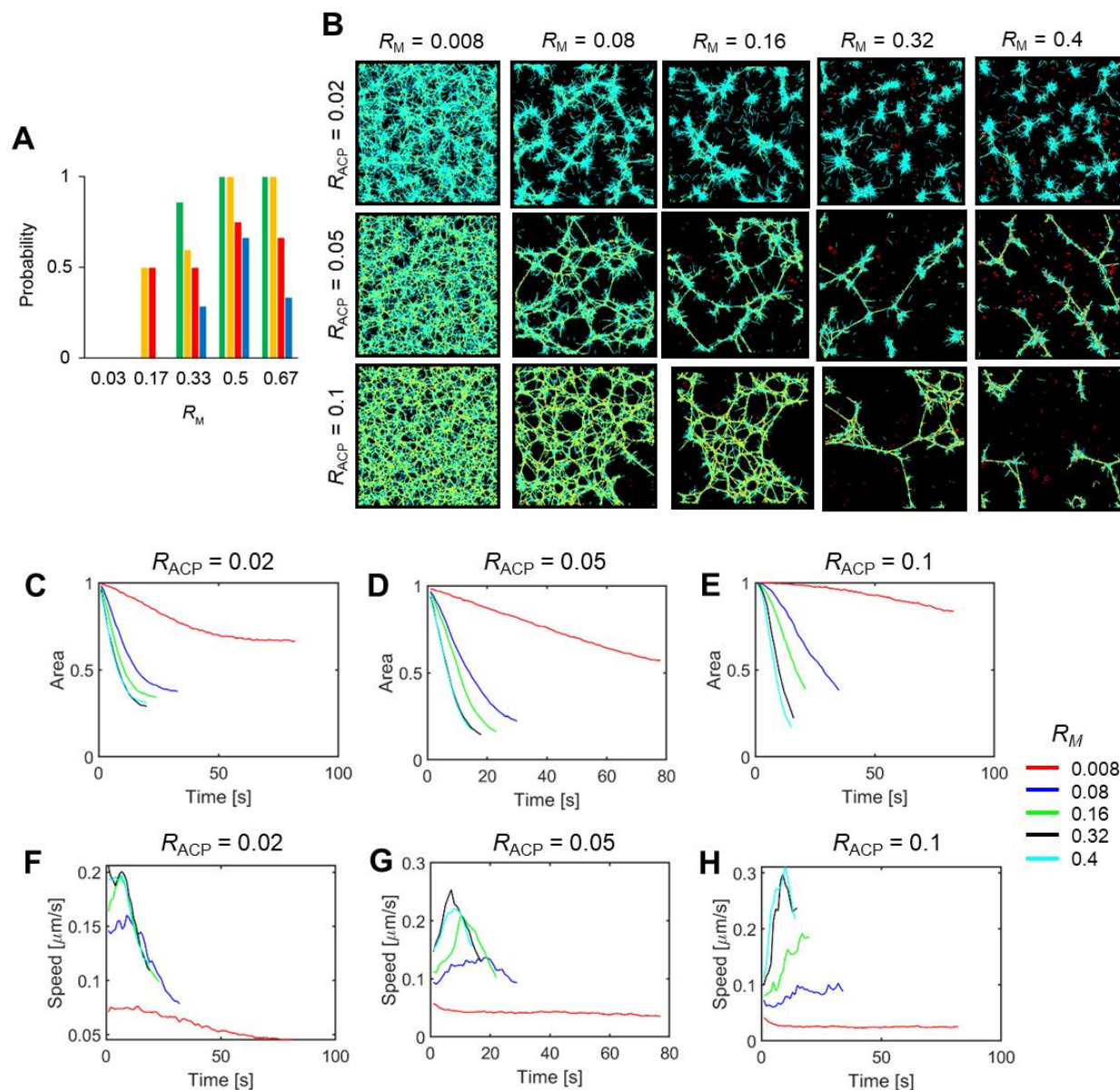
Figure 4.11. Influences of motor and crosslinker density on network morphology. (A) Network morphology in simulation. Higher motor density facilitates network contraction into clusters, which is more pronounced at higher crosslinker density. (B) The probability of cluster formation. The probability is calculated as the ratio of the number of experiments with cluster formation to the total number of performed experiments. R_A is 0.033 (green), 0.067 (yellow), 0.1 (red), and 0.2 (blue). (C-E) Change of area covered by clusters over time. (F-H) Ensemble average of actin speed as a function of time. Data during initial 8 s was used. Note: (A) is from Kyohei Matsuda and Junichiro Yajima at the University of Tokyo.

Results from simulations also showed that networks with higher motor density tended to show faster contraction into fewer larger clusters (Figs. 4.10E-G and 4.11B-H). We found a single

cluster forms at high R_{ACP} (= 0.1) and R_M (= 0.4) in simulation. Due to computational cost, we did not increase R_{ACP} above 0.1, but we expect that contraction would be suppressed even with high R_M if there are numerous ACPs, as observed in experiments. With $R_M \leq 0.16$, more ACPs result in slower contraction at the same motor density, which is also consistent with results shown in Fig. 4.7. Interestingly, at high R_M, contraction and moving speeds were higher in cases with more ACPs. Because a large number of motors generate forces, the resistance of a network to contraction becomes less important, but higher connectivity resulting from ACPs enables motors to contract networks faster. This is also supported by observation that contraction and moving speeds with the lowest R_{ACP} did not increase much due to a further increase in R_M if R_M is already high enough, which was also shown in experimental results.

4.3.3 ATP concentration highly affects the length-scale of contraction and cluster size

During the cross-bridge cycle of myosin, the unbinding of a myosin head from F-actin requires the binding of an ATP molecule to the head. Thus, with higher ATP concentration (C_{ATP}), the unbinding rate becomes higher, which decreases processivity but increases walking speed. In addition, due to a decrease in the duty ratio, forces generated by one thick filament may decrease with higher C_{ATP}. It is not clear how these changes would affect network contraction. Thus, we conducted experiments with a wide range of C_{ATP} at different R_A (Figs. 4.12A and 4.13A, B). At the lowest $R_A = 0.03$, networks formed larger clusters more rapidly as C_{ATP} increases from 1 μM to 100 μM (Fig. 4.12B-D). Although the duty ratio and forces of myosin decrease with higher C_{ATP}, loosely cross-linked networks can still contract into clusters because large, long-lasting forces are not necessary for the contraction of such a network. Thus, network contraction speed is determined largely by the walking speed of myosin heads. However, with the highest $C_{ATP} = 1000$ μM, networks did not show noticeable contraction (Fig. 4.12B) and showed slower F-actin movements (Fig. 4.12D) because the duty ratio and forces of myosin became too small. As a result, both contraction and moving speeds show biphasic dependence on C_{ATP} (Fig. 4.12C, D), which is consistent with a previous study that employed reconstituted networks consisting of actin, myosin II, and fascin [121]. With higher R_A, we still observed the biphasic dependence, but optimal C_{ATP} yielding maximum contraction and moving speeds was lower as R_A was larger (Fig. 4.12C, D); greater forces from lower C_{ATP} are required to contract networks with more cross-linking points.

The probability of cluster formation also showed biphasic dependence on C_{ATP} and was mostly larger with smaller R_A (Fig. 4.13C).
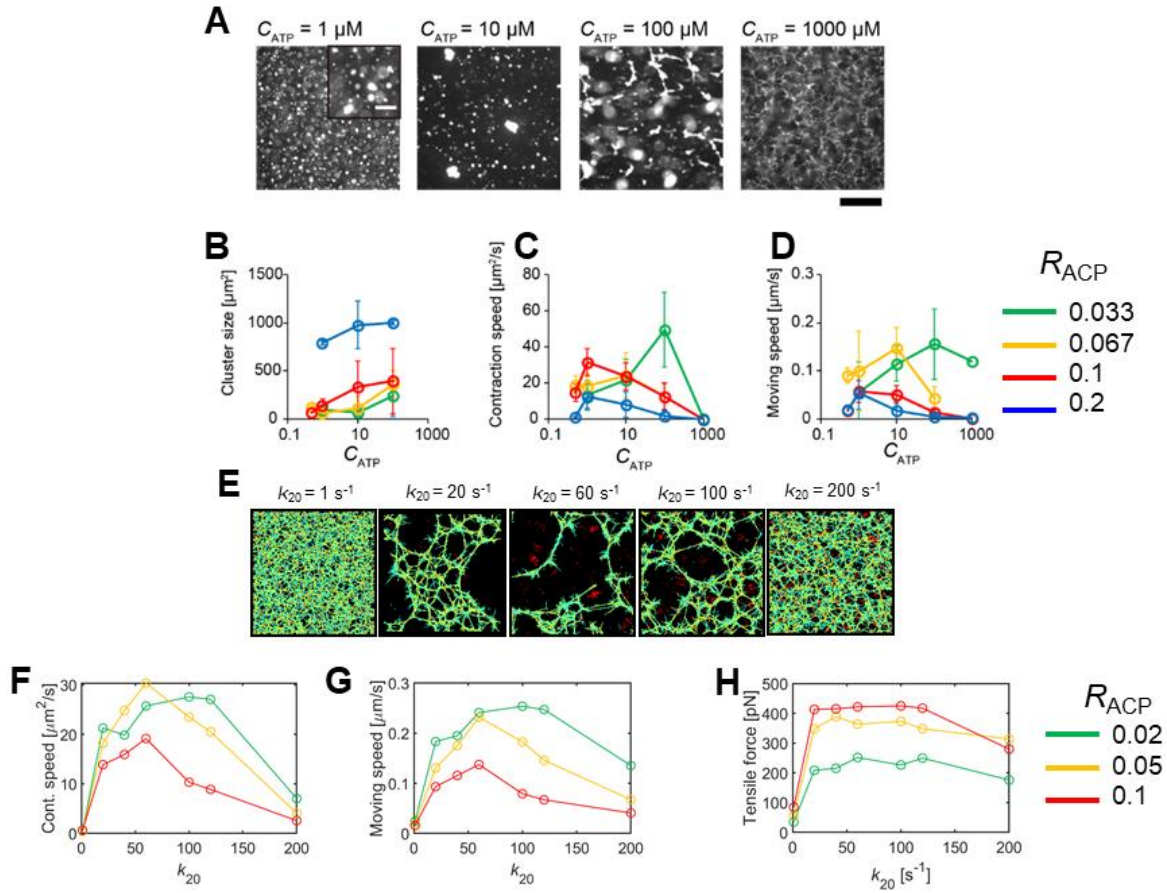
Figure 4.12. Network contraction with a wide range of ATP concentration. (A-D) Results from experiments G-actin (3 μM), myosin ($R_M = 0.33$), anillin ($R_A = 0.03$-0.2), ATP (0.5-1000 μM), and the ATP-regenerating system. (A) Representative fluorescence microscope images of networks with different ATP concentration (C_{ATP}) at $R_A = 0.1$. A scale bar corresponds to 100 μm. (B-D) Dependence of cluster size, contraction speed, and moving speed on C_{ATP} at $R_A = 0.03$ (green), 0.07 (orange), 0.1 (red), and 0.2 (blue). (E-G) Results from simulations with F-actin (100 μM), motor ($R_M = 0.16$), and ACP ($R_A = 0.1$). We varied ATP-the dependent unbinding rate of motors to mimic a change in C_{ATP} (k_{20}). (E) Network morphology in simulation at 15 s depending on k_{20} with $R_{ACP} = 0.1$. Actins (cyan), myosin motors (red), and ACPs (yellow) are shown. (F) Contraction speed, and (G) moving speed depending on k_{20}. In both experiments and simulations, network contraction speed and moving speed show biphasic dependence on ATP concentration. Data during initial 8s was used to calculate contraction speed and moving speed. (H) Average tensile force exerting on selected actin segments. Throughout simulation, ten actin segments with highest tensile force were selected. Note: (A)-(D) are from Kyohei Matsuda and Junichiro Yajima at the University of Tokyo.

108
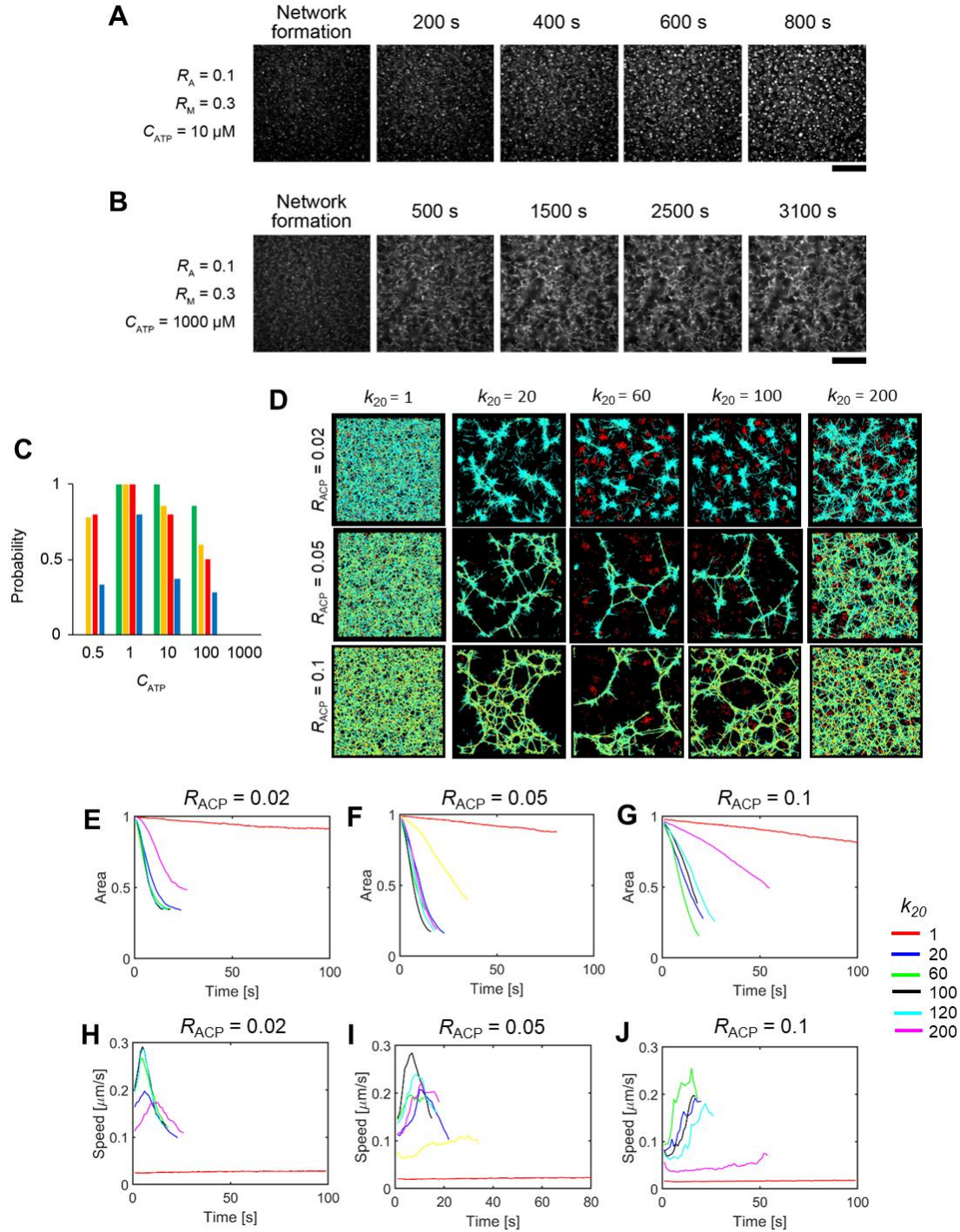
Figure 4.13. Effects of ACP density and k_{20} on network morphology. (A, B) Cases shown in 3A. (C) The probability of cluster formation. The probability is calculated as the ratio of the number of experiments with cluster formation to the total number of performed experiments. R_A is 0.033 (D) Network morphology in simulation. (E-G) Change of area covered by clusters over time. (H-J) Ensemble average of actin speed as a function of time. Note: (A)-(C) are from Kyohei Matsuda and Junichiro Yajima at the University of Tokyo.

In simulations, to mimic a variation in C_{ATP}, we varied the ATP-dependent unbinding rate of myosin heads (k_{20}) used in the parallel cluster model [72, 73], which was incorporated in our agent-based model. With higher k_{20}, the duty ratio and stall force of motors are reduced, but the walking rate increases, which corresponds to changes in myosin due to an increase with ATP concentration. As in experiments, contraction and moving speeds showed biphasic dependence on k_{20} (Figs. 4.12F-G and 4.13D-J). In addition, optimal k_{20} level for maximum contraction/moving speeds tended to be smaller with higher R_{ACP} like experiments.

4.3.4 The contraction of mechanically stable networks can be triggered by F-actin fragmentation

So far, we have shown how forces generated from motors contract networks by competing with resistance from ACPs. One of the observations was that networks with a very large amount of anillin did not exhibit noticeable contraction due to mechanical stability originating from high network connectivity. We attempted to induce the contraction of such stable networks by perturbing network connectivity via a protein called gelsolin which severs F-actins [122]. First, we assembled a prestressed network with G-actin (3 μM), myosin ($R_M = 0.33$), and anillin ($R_A = 0.2$) in the presence of ATP (50 μM) and the ATP-regenerating system. After network assembly, we added gelsolin and monitored the emergence of contraction. Soon after the addition of gelsolin, the prestressed network began to contract locally, and then the contraction was propagated to a whole network, resulting in multiple medium-sized clusters (Fig. 4.14A). A control experiment with the addition of a buffer solution without gelsolin did not show noticeable contraction (Fig. 4.14B). This difference in two experiments demonstrates that the contraction was induced by the severing activity of gelsolin. We also found that contraction speed was larger with higher gelsolin concentration (Fig. 4.14C). These results imply that F-actin fragmentation can facilitate network contraction by perturbing the mechanical stability of networks.
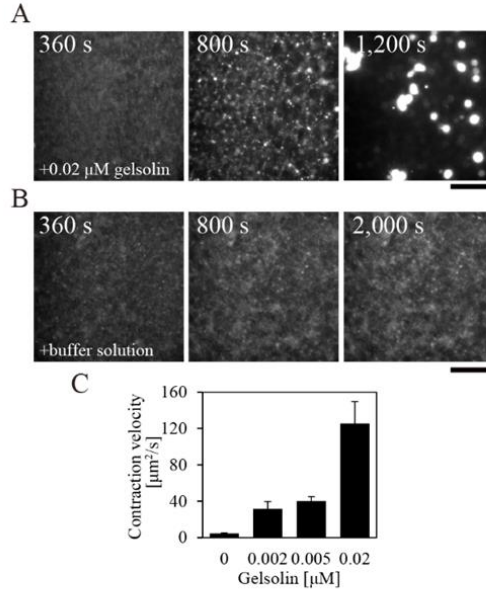
Figure 4.14. Triggering contraction of mechanically stable networks via severing of F-actins. Networks were assembled with G-actin (3 μM), rhodamine phalloidin (1 μM), myosin ($R_M = 0.33$), anillin ($R_A = 0.2$), ATP (50 μM), and the ATP-regenerating system. Since a network is densely cross-linked, significant contraction does not occur. (A, B) Sequential images of networks with a scale bar indicating 100 μm. In (A), the actin-severing protein, gelsolin, is introduced to the network after assembly ($t = 360$ s) in order to shorten F-actins. Soon after addition of the gelsolin (final concentration, 0.02 μM), the network contracts into medium-size clusters. In (B), a buffer containing 50 μM ATP was injected as a control experiment. After addition of the buffer contraction does not occur. (C) A change in contraction speed with different gelsolin concentration. The number of experiments is 3 for 0 μM, 3 for 0.002 μM ($R_{Gelsolin} = 0.00066$), 4 for 0.005 μM ($R_{Gelsolin} = 0.0017$), and 4 for 0.02 μM ($R_{Gelsolin} = 0.0066$). Note: This figure is from Kyohei Matsuda and Junichiro Yajima at the University of Tokyo.

However, the fragmentation by severing proteins is external perturbation applied to prestressed stable networks. We further investigated whether F-actin fragmentation plays an important role in network contraction even without severing proteins. We introduced a small amount of F-actins labeled by rhodamine phalloidin (0.1%) to a network with unlabeled G-actin (3 μM), myosin ($R_M = 0.33$), anillin ($R_A = 0.2$), and ATP (1 mM) in the absence of the ATP-regenerating system (Fig. 4.15). We found that F-actins were frequently fragmented during network contraction, and then the fragments moved in opposite directions, forming small clusters in most cases (Fig. 4.15A). We measured the speed of labeled F-actin segments over time (Fig.

4.15B). The speed initially fluctuated over a small range but occasionally showed a rapid jump. We found that such a sharp increase in the speed appeared right after F-actin fragmentation. The speed showed two-fold increase in ~80% of fragmented F-actins (Fig. 4.15C). These results imply that F-actins were fragmented by tensile forces rather than buckling because they showed rapid retraction in the opposite directions right after fragmentation, which is reminiscent of the retraction of stress fibers in cells observed right after laser ablation [123]. We also found that F-actin fragmentation takes place most severely at the lowest $C_{ATP} = 1$ μM in which motors generate larger forces (Fig. 4.16). It is likely that the formation of small clusters at $C_{ATP} = 1$ μM (Fig. 4.12A, B) is attributed to severe F-actin fragmentation facilitated by large tensile forces generated from stronger motors.
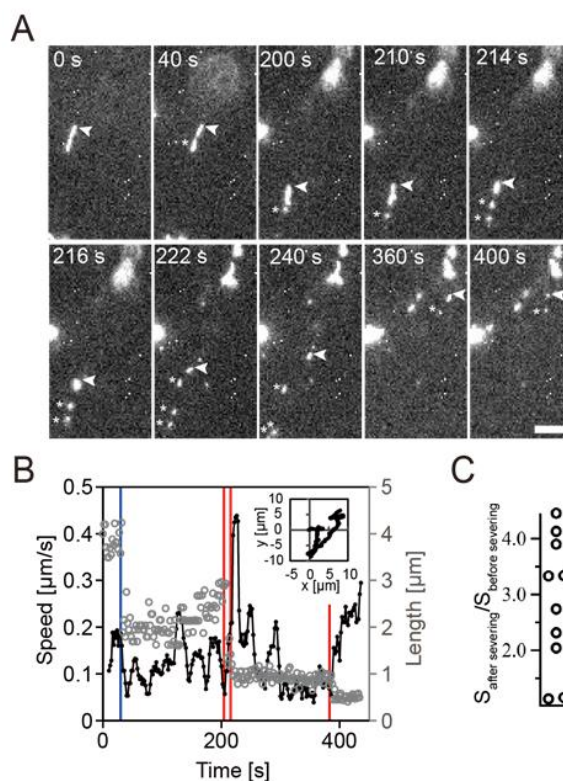
Figure 4.15. Observation of fragmentation of F-actins during network contraction. Networks were prepared with G-actin (3 μM), phalloidin (1 μM), myosin (R_M = 0.33), anillin (R_A = 0.2), ATP (1000 μM), and the ATP-regenerating system. A small number of F-actins labeled by rhodamine phalloidin (0.1 %) were included in the networks. (A) Time-lapse images of the labeled F-actins with time points from the initiation of observation. The observation began 6 min after mixing. White arrowheads indicate a traced fragment. A scale bar indicates 5 μm. (B) The speed of a F-actin fragment (black dot and line) indicated by orange arrowheads in (A), and the length of the fragment (gray open circle) over time. Red lines denote the fragmentation followed immediately by a jump in the speed (212 s, 218 s, and 390 s), meaning retraction of tensed F-actin. A blue line on the left denotes F-actin fragmentation without a significant increase in the speed (40 s), which is likely to be buckling-induced fragmentation. Inset: An example of the trajectory of F-actin fragments. (C) The sharp increase in the speed occurred right after fragmentation in 8 experiments out of 10. Note: This figure is from Kyohei Matsuda and Junichiro Yajima at the University of Tokyo.

113
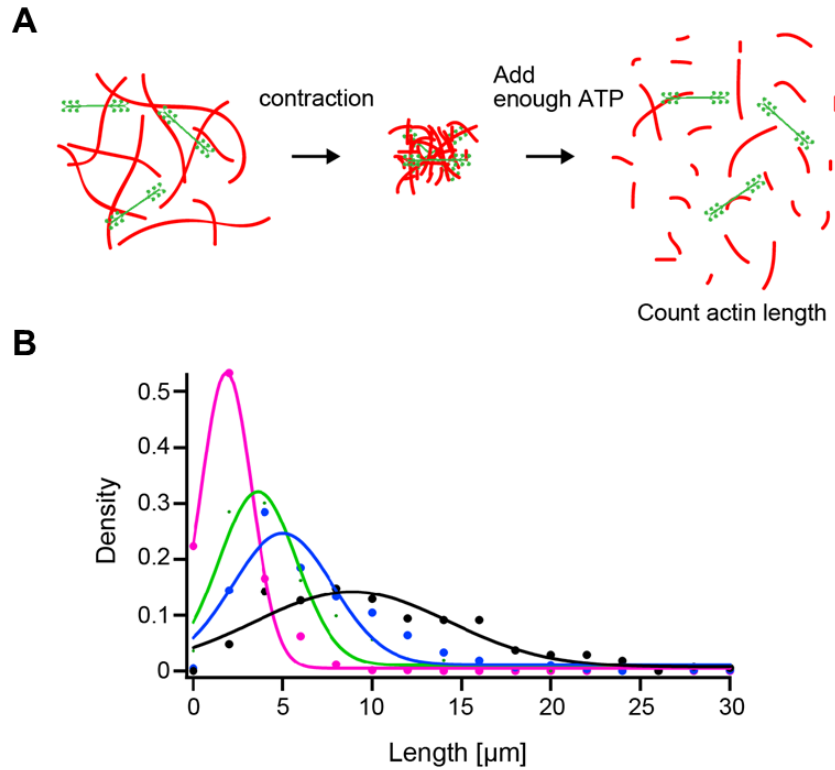
Figure 4.16. Actin fragmentation dependent on ATP concentration. (A) Actin fragmentation assay in bulk containing 3 µM G-actin, 1 µM myosin and various concentration of ATP with ATP regenerating system. In this experiment, after network contraction, excessive amount of ATP (5 mM) was added. The clusters were loosened, and the length of the actin filament was measured. (B) $C_{ATP} = 1$ µM; 1.9 ± 1.0 µm (magenta, n = 658), $C_{ATP} = 10$ µM; 3.6 ± 1.2 µm (green, n = 708), $C_{ATP} = 100$ µM; 5.0 ± 1.4 µm (blue, n = 622), $C_{ATP} = 1000$ µM; 8.9 ± 1.9 µm (black, n = 372). Note: This figure is from Kyohei Matsuda and Junichiro Yajima at the University of Tokyo.

4.3.5 F-actin fragmentation is particularly important for the contraction of networks with high connectivity

Previous studies demonstrated that network contraction necessitates the unbinding of ACPs if network connectivity is high [24]. Each ACP unbinding event breaks one cross-linking point between a pair of F-actins. If subsequent unbinding events occur rapidly, mechanically stable networks may be able to contract. However, ACPs may bind back to F-actin soon after they unbind from F-actin, meaning that many of the unbinding events could be insignificant for network contraction. In addition, as mentioned earlier, the unbinding rate of ACPs is not varied over a wide range in cells unlike the ATP-dependent unbinding rate of myosin motors. Thus, if a network

114

consists of long F-actins and many ACPs, the ACP unbinding might not be sufficient for breaking down the network into clustering structures. Unlike ACP unbinding, F-actin fragmentation is mostly an irreversible process unless F-actin turns over or is annealed [124], which are inhibited or hardly occurs in *in vitro* experiments. In addition, since network connectivity is more sensitive to average F-actin length than to ACP density [27], F-actin fragmentation may facilitate network contraction better than ACP unbinding. However, since an F-actin can support a tensile force up to ~500 pN before it is fragmented [114], large forces should be generated across a network.

We ran a set of simulations with or without force-induced F-actin fragmentation in order to identify conditions under which F-actin fragmentation plays an important role in network contraction. We first varied R_M and average length of F-actin ($<L_f>$) in the presence of ACP unbinding with $R_{ACP} = 0.1$ and $k_{20} = 20$ s^{-1}. We increased $<L_f>$ above the value used in the simulations presented earlier ($<L_f> = 1$ μm) since tensile force didn't reach ~500 pN in those simulations with $<L_f> = 1$ μm (Fig. 4.7F, 4.10H, 4.12H). F-actin fragmentation affected network morphology and contraction/moving speeds significantly only when R_M and $<L_f>$ were very high where fragmentation occurred frequently (Figs. 4.17 and 4.19). When either R_M or $<L_f>$ was low, sufficiently large forces could not be developed, so F-actin fragmentation did not occur frequently. Under the condition causing frequent F-actin fragmentation ($R_M = 0.4$) and ($<L_f> = 2.6$ μm), we varied R_{ACP} and k_{20} to understand how these variables affect the role of fragmentation for network contraction. When R_{ACP} was low, or when k_{20} was high, the network showed similar morphology and contraction/moving speeds, regardless of the presence of F-actin fragmentation (Figs. 4.18 and 4.20). In these cases, low connectivity or low duty ratio of motors hindered large force generation by motors, thus causing fragmentation to less likely to occur.
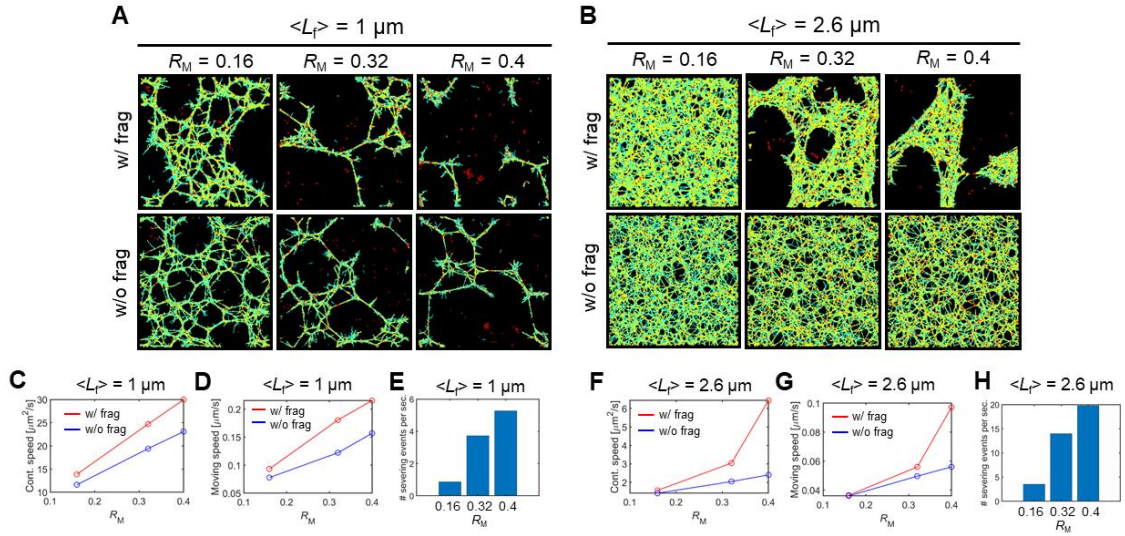
Figure 4.17. Differential effects of F-actin fragmentation under different conditions. (A, B) Network morphology of simulation at 15 s with or without tensile force-induced F-actin fragmentation (frag) with (A) short ($<L_f>$=1 µm) and (B) long F-actins ($<L_f>$=2.6 µm). R_{ACP} was 0.1. F-actin (cyan), motors (red), and ACPs (yellow) are shown. F-actin fragmentation facilitates network contraction when filament length is long (2.6 µm) and motor density is high (R_M = 0.32~0.4) (C, D, F, G) Contraction speed and moving speed during initial 8 s calculated in the cases shown in (A, B). (E, H) Time-averaged number of severing events.
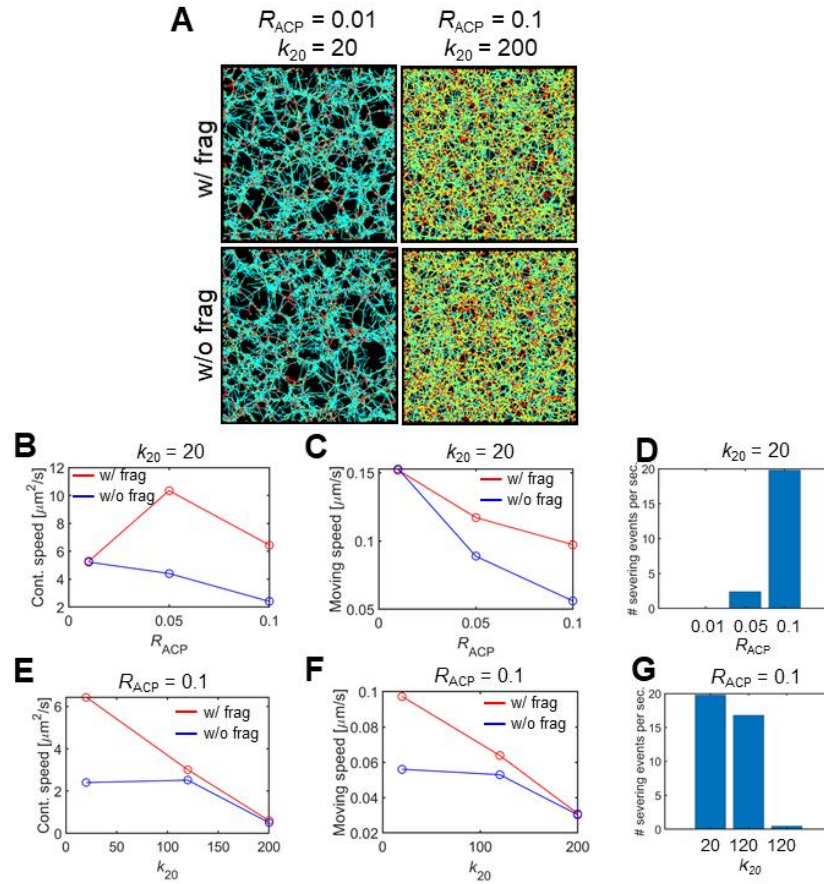
Figure 4.18. Differential effects of F-actin fragmentation under different conditions. (A-C) Network morphology of simulation under different conditions. Actins (cyan), myosin motors (red), and ACPs (yellow) are shown. (B, C, E, F) Contraction speed and moving speed averaged at initial 8 s. (D, G) Time-averaged number of severing events.
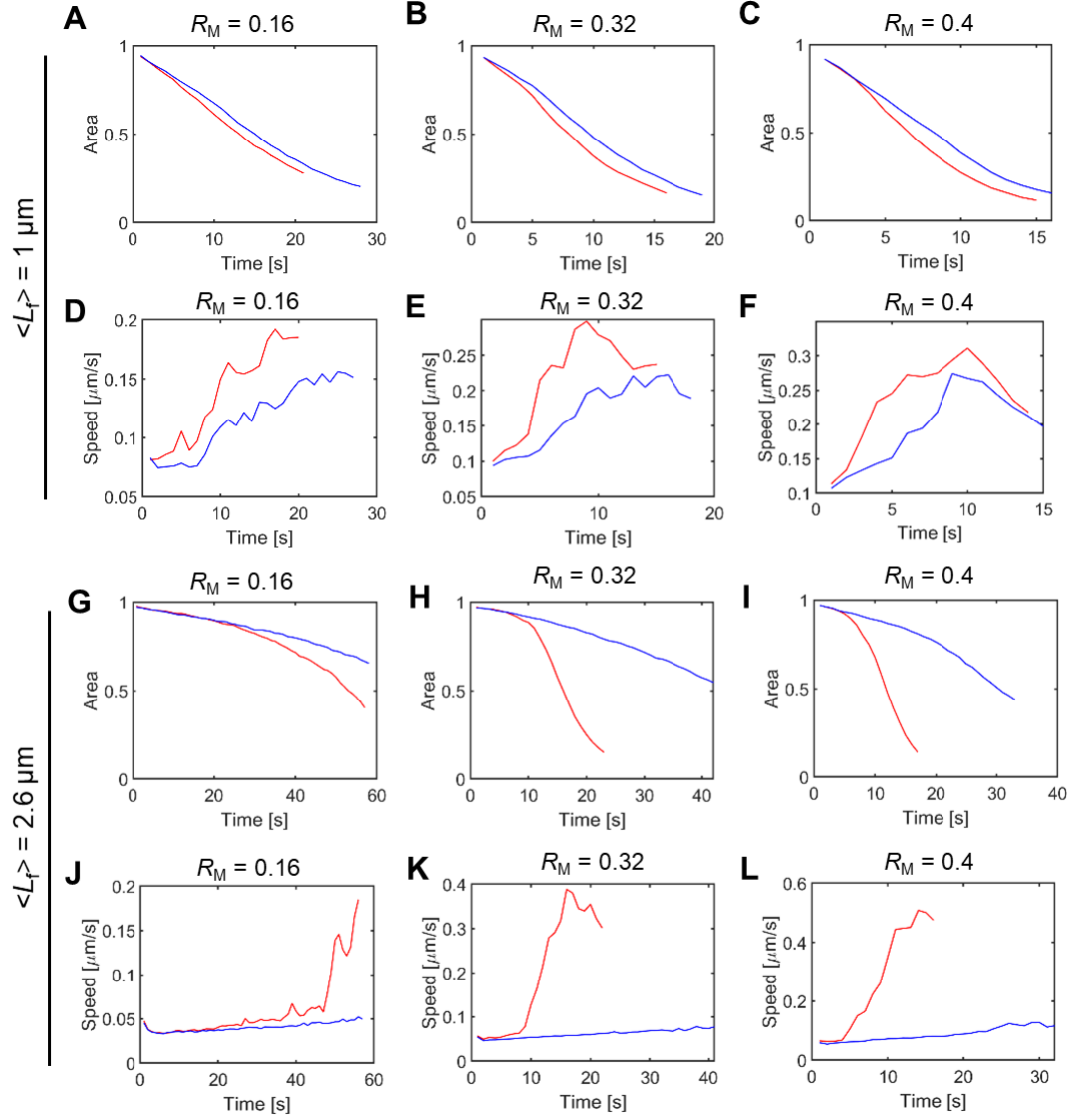
Figure 4.19. Contraction speed and moving speed depending on F-actin fragmentation. Network contraction over time and ensemble average of actin speed in the cases with (red curve) or without (blue curve) F-actin fragmentation. With fragmentation, network contracts faster.
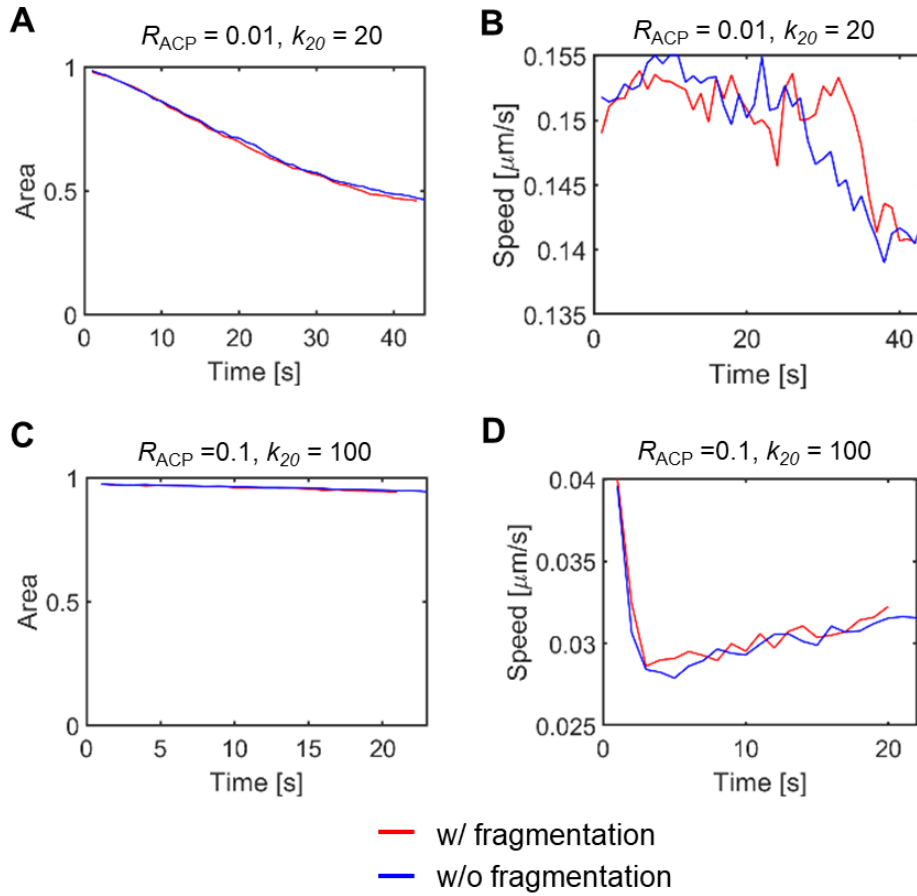
Figure 4.20. Contraction speed and moving speed with or without F-actin fragmentation. (A, C) Network contraction over time in the cases with (red curve) or without (blue curve) F-actin fragmentation. With fragmentation, network contracts faster. (B, D) Ensemble average of actin speed as a function of time in the cases with or without F-actin fragmentation. With fragmentation, actins move faster. Data was averaged during initial 8 s.

From these results, we conclude that F-actin fragmentation can facilitate the contraction of networks where motors can develop sufficiently high forces on F-actins, such as networks with high network connectivity (high R_{ACP} and $<L_f>$), high R_M, and high duty ratio of motors (low k_{20}).

4.3.6 F-actin fragmentation can solely induce network contraction or enhance contraction caused by ACP unbinding

We studied the relative importance of ACP unbinding and F-actin fragmentation for network contraction by running additional simulations under three conditions: i) with F-actin fragmentation and ACP unbinding, ii) with F-actin fragmentation without ACP unbinding, and iii)

with ACP unbinding without F-actin fragmentation (Fig. 4.21). When average filament length and R_M were low, the case without ACP unbinding shows long time delay (~15 s) before contraction (Fig. 4.21A-C). Once main contraction started, network contraction speed (i.e., the decreasing rate of area over time) was higher than the two other cases with ACP unbinding, implying catastrophic fragmentation events. The first fragmentation event was hard to occur under this condition because motors cannot generate large force and forces are uniformly distributed on the network with permanent cross-links, leading to the time delay. However, once a few fragmentation events occurred, force distribution became heterogeneous in short time scale due to perturbed network connectivity, resulting in the accumulation of large forces on some of the other F-actins and thus more F-actin fragmentation. By contrast, two cases with ACP unbinding showed similar morphology and contraction dynamics, regardless of whether F-actin can be fragmented or not. If ACPs unbind from F-actins, forces acting on networks are relaxed, which prevents F-actins from being fragmented by tensile forces. Indeed, the frequency of F-actin fragmentation with ACP unbinding was very low (Fig. 4.21B). This indicates that ACP unbinding plays a more crucial role in network contraction than F-actin fragmentation under the condition with low network connectivity and low motor density.
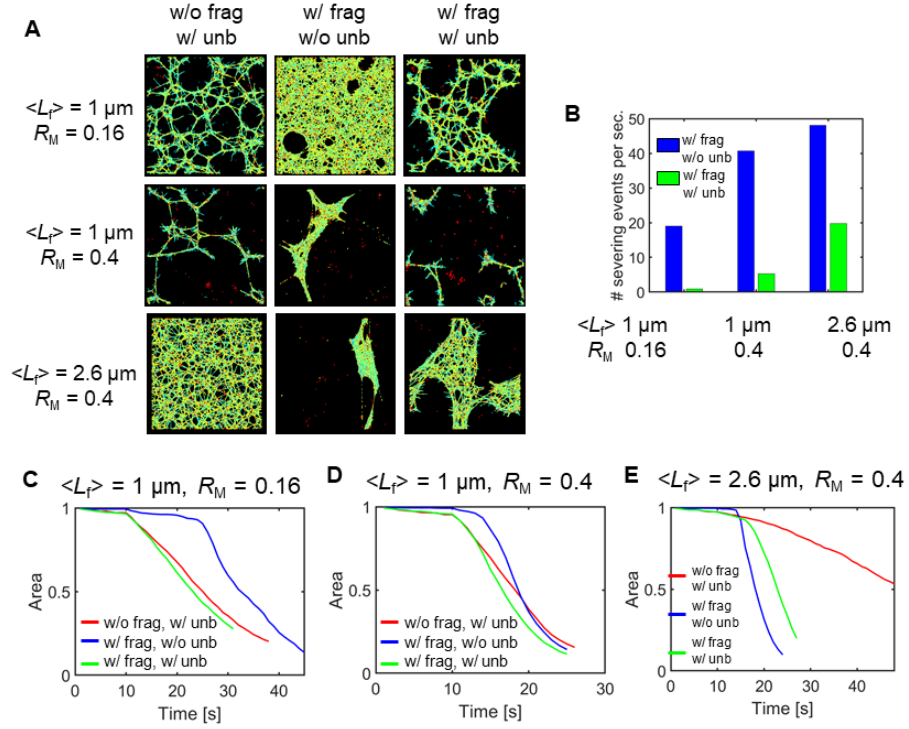
Figure 4.21. Relative importance of F-actin severing and ACP unbinding on network contraction depends on initial network connectivity. (A) Snapshots of networks with R_{ACP} =0.1 where F-actin severing is inactivated (first column), ACP unbinding is inactivated (second column), and both F-actin severing and ACP unbinding is activated (third column). (B) Time-averaged number of severing events per second, which is calculated in the cases shown in (A). (C-E) Network area over time in the cases shown in (A).

We repeated simulations with higher $R_M = 0.4$ (Fig. 4.21A, B, D). A noticeable difference is that time delay in the case only with F-actin fragmentation is much shorter (< 3 s) than that observed in the cases with fewer motors. If there are more motors, F-actin fragmentation can be fragmented much easier even without ACP unbinding since F-actins experience larger forces. The case with both ACP unbinding and F-actin fragmentation started showing contraction earlier, but the initial contraction speed was similar to that in the case only with F-actin fragmentation, which is higher than contraction speed in the case only with ACP unbinding. It was found that F-actin fragmentation still occurred in the presence of ACP unbinding. These observations indicate that under the condition with short filaments and a large number of motors, F-actin fragmentation can solely induce fast network contraction without ACP unbinding or enhances network contraction to some extent with ACP unbinding.

With higher R_M and longer filaments, the case only with ACP unbinding exhibited the slowest contraction with a gradual decrease in the area whereas two other cases with F-actin fragmentation showed a sharp drop in the area due to catastrophic fragmentation events (Fig. 4.21A, B, E). In the presence of fragmentation, more frequent fragmentation occurred in the case without ACP unbinding (Fig. 4.21B). Interestingly, the case only with F-actin fragmentation overtook that with F-actin fragmentation and ACP unbinding although contraction started late. These imply that F-actin fragmentation is much more important for network contraction than ACP unbinding in the network with long filaments. In such a network, fragmentation can reduce network connectivity more effectively compared to ACP unbinding.

4.4   Discussion

The contractile behaviors of actomyosin networks have been investigated actively during recent decades using a number of in vitro experiments and theoretical/computational models. In early studies, researchers focused mainly on interactions between F-actins and myosin motors [125]. Later, the importance of the dynamic behaviors of other cytoskeletal components has been discovered in several studies. For example, it was shown that the unbinding of ACPs is of great importance for the viscoelastic responses of actomyosin networks, such as stress relaxation, creep, plastic deformation, and frequency-dependent shear moduli [24, 126-128]. More recent modeling studies demonstrated that the turnover of F-actins can help networks sustain generated stress and homogeneous morphology for long time [129] and that buckling of F-actins is crucial for network contraction and force generation [27].

However, none of these studies paid attention to F-actin fragmentation that can result from large tensile forces developed during network contraction. In this study, we investigated the role of force-induced F-actin fragmentation using reconstituted actomyosin networks and computational models. First, as a base study, we showed how network contraction is governed by the amount of motors, ACPs, and ATP. The effects of the densities of motors and ACPs were consistent with observations in previous experiments and simulations [94, 110]. In general, with more motors, networks contracted faster to a greater extent, and network contraction was maximal at intermediate ACP density. ATP influenced the contractile behaviors of networks in a biphasic manner, meaning that the contraction was faster and greater at optimal intermediate ATP

concentrations that depends on network connectivity. The biphasic dependence of contraction and moving speeds was consistent with a previous in vitro experiment [121].

In our experiments, we observed several fragmentation events of F-actins during network contraction. Such fragmentation events were observed in a previous in vitro experiment [25], but it was suggested that F-actins were fragmented due to buckling. However, careful examination of time-lapse images implied that a large fraction of F-actin fragmentation events observed in our experiments resulted from tensile forces. We ran simulations in the presence of force-induced F-actin fragmentation under various conditions. It was found that force-induced F-actin fragmentations can facilitate network contraction especially when both network connectivity and contractility are high. If the contractility is not high enough, F-actin fragmentation is less important for network contraction than ACP unbinding.

In cells, F-actin turns over rapidly, which can prevent motors from generating very large forces as our previous study showed [64]. Then, force-induced F-actin fragmentation can be less important for network contraction in cells. Further, the constant structural fluctuation of actin network might be controlled by other F-actin fragmentation induced by different mechanisms, such as F-actin buckling by non-muscle myosin IIB [130, 131] or F-actin twisting by the binding of cofilin [124]. However, in the regions of cells with slow F-actin turnover without many other proteins causing F-actin fragmentation, force-induced F-actin fragmentation could be quite important for the contractile behaviors of actomyosin networks.

Although we found the significance of the F-actin fragmentation induced internally by motors, we expect that F-actins in passive networks with permanent or less transient ACPs (i.e., without motors) subjected to external large strain or stress can undergo fragmentation events because some of them would support very large tensile forces as shown in many previous studies [132, 133]. In a broader context, any kind of network structures consisting of cross-linked semi-flexible or rigid polymers can undergo catastrophic force-induced polymer fragmentation under high loads and thus show rapid rupture or fracture because if the polymers are severed by tensile forces without significant yielding.

In this study, we demonstrated that F-actins are fragmented by tensile forces during the contraction of actomyosin networks, and that the F-actin fragmentation can indeed play a significant role for inducing the contraction of otherwise non-contractile networks, which has been neglected to date. In the near future, we will include F-actin turnover and F-actin fragmentation

induced by both buckling and large tensile forces to evaluate their relative significance for the contractile behaviors of actomyosin networks in more physiologically relevant circumstances.

5. DYNAMIC MOTIONS OF MOLECULAR MOTORS IN THE ACTIN CYTOSKELETON

The work described in this chapter has been published in [134].

5.1 Introduction

Cells move cellular cargos by a process called intracellular transport. Intracellular transport plays a crucial role in a wide variety of cellular functions [135, 136]. For example, during the development of neural systems, neurotransmitters and mRNAs are transported, which facilitates neuronal functions including neurogenesis and morphogenesis [135]. In addition, cholesterol levels in cell membranes, which affect membrane properties and signal transduction processes, are regulated via intracellular transport [136].

To understand how cells regulate intracellular transport, many researchers have characterized motions of cargos via single particle tracking [30]. By tracking and analyzing the motions of vesicles or microspheres inside cells, it has been discovered that they undergo dynamically distinct motions [32]. The slope of the mean square displacement (MSD) calculated from their trajectories in log-log scale (α) provides information about the nature of the motions. Vesicles attached to cellular components, such as a membrane, tend to show stalled or highly subdiffusive motions ($\alpha << 1$) [31, 137-139]. When cargos are not connected physically to any cellular component, they are transported within the cytosol primarily via diffusion [140]. Due to crowded environments of cytoplasm, they exhibit subdiffusive motions ($\alpha < 1$) [141]. Cargos can be transported by molecular motors along the cytoskeleton, which is called active transport. Cargos undergoing active transport show ballistic ($\alpha \sim 2$) or superdiffusive ($1 < \alpha < 2$) motions [31, 142]. Cargos can also show a subdiffusive or stationary behavior when multiple molecular motors are bound to a single cargo and attempt to move in different directions [29], which is called tug-of-war [143].

Traditional studies regarding active transport focused mainly on transport of cargos driven by two types of molecular motors, kinesin and dynein, along radially oriented microtubules. This active transport is responsible for long-distance transport between a cell nucleus and a membrane [144, 145]. For example, cargos are transported from the nucleus to the membrane for secretion

by kinesin, and from the membrane to the nucleus for endocytosis by dynein [146]. However, cargo transport along actin structures is also of great importance for local transport and cooperates with microtubule-based transport. For example, in neuronal growth cones, transport is dependent on both microtubules in the axon and F-actin in the soma [147, 148]. In addition, myosin V helps regulation of secretory processes by preventing a majority of secretory vesicles in cortical actin networks from reaching a membrane [149, 150]. Due to structural differences between microtubules and the actin cytoskeleton, motions of cargos are quite different depending on where they are moving. Cargos exhibit directed motions on microtubules, whereas they show more diffusive and slower behaviors on actin structures [32, 33, 151]. Studies demonstrated that MSD of myosin motors walking on random actin networks decays as measurement time increases, which corresponds to the aging process in glassy dynamics [152, 153].

Since actin networks in cells are highly disorganized, it is not obvious how myosin motors walk along the actin networks. One study found that MSD of myosin II is quite different depending on network architecture and types of cross-linkers [34]; motors walking on mixed polarity bundles formed by fimbrin and α-actinin can be trapped, whereas polarity-sorted bundle structures formed by fascin lead to highly directional motions. Another study using liposomes linked to multiple myosin V molecules showed that motions of the liposomes tend to be stalled more in unbranched actin networks, compared to those in branched networks formed by Arp2/3 [29]. These experimental studies suggest that motors that can bind to more than one F-actin can be stalled or slow down due to tug-of-war.

Computational models have also been widely used to identify governing factors for the motions of motors in actin networks. It was found that cargos are transported from a nucleus to a membrane most efficiently when actin is densely distributed near the nucleus [154]. Also, it was shown that the length and number of F-actins significantly affect transport efficiency [155, 156]. In addition, several studies showed that specific geometry of actin networks can trap motors. For example, it was demonstrated that stalling of myosin motors walking on an actin network may originate from a cycling state in which motors keep circulating within a geometrical trap formed by more than two F-actins [157]. Another study showed that motors can be trapped near the center of clusters formed by motor-driven polarity sorting of F-actins [158]. These computational studies have provided valuable insights into understanding of how myosin motors move in disorganized actin structures. However, some of the assumptions used in those studies were less biologically

relevant in that the mechanics and dynamics of cytoskeletal components were neglected or oversimplified. For example, load-dependent velocity of motors have not been incorporated in many previous models [154-156]. In addition, it was assumed that a network is completely rigid, meaning that filaments constituting a network were not allowed to be displaced or deformed [157].

We hypothesized that motions of motors can be quite different if assumptions are closer to real actin networks. We employed an agent-based computational model to investigate motions of motors in disorganized actin networks with more physiologically relevant assumptions. The model accounts for the mechanics and dynamics of cytoskeletal components, such as the force-dependent walking velocity of motors and deformability of actin networks. We quantitatively analyzed motions of myosin motors in actin networks under various conditions. We found that motor motions can be confined due to three different reasons in the absence of F-actin turnover. Two of the reasons were verified via in vitro experiments using reconstituted actomyosin networks. However, in the presence of F-actin turnover, motors consistently move for a long time without significant confinement.

5.2   Methods

5.2.1   Model Overview

We used the agent-based model built introduced in Chapter 2 and used in our previous studies [27, 61-63]. Parameter values used in this research are listed in Tables 5.1 and 5.2. Values of most parameters are adopted from our previous studies [43, 61, 63, 64].
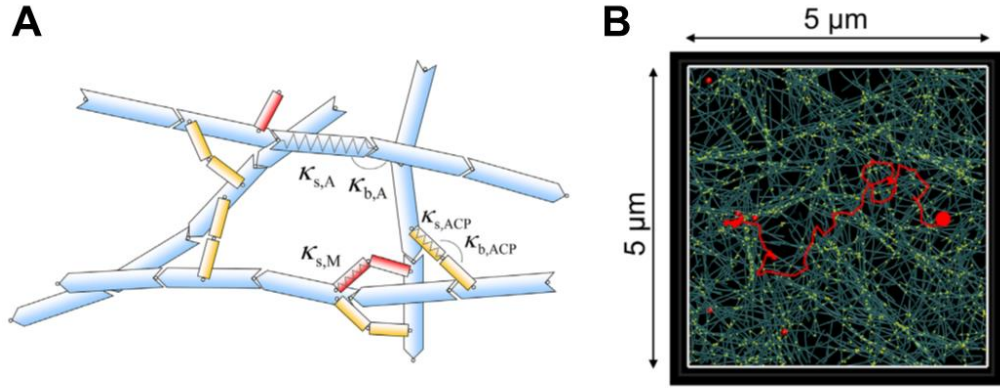
Figure 5.1. Analysis of motor motions using an agent-based computational model. (A) Actin filaments (F-actins, blue) are modeled as serially connected cylindrical segments. Adjacent segments are connected by elastic hinges. Actin cross-linking proteins (ACPs, yellow) and two-arm motors (red, bottom) are modeled as two segments connected by elastic hinges. One-arm motors (red, top) are modeled as one segment. ACPs can bind to a pair of F-actins to form a functional cross-link. One-arm motors can bind to only one F-actin unlike two-arm motors that can bind to a pair of F-actins simultaneously. Arms of motors walk toward the barbed ends of F-actins. Bending (κ_b) and extensional (κ_s) stiffness govern mechanical behaviors of these segments. (B) An example of movement of a motor walking on a thin cortex-like network. A periodic boundary condition is applied in x and y directions. A trajectory of a motor measured in a simulation is visualized using a red line. A red circle represents the initial position of the motor.

Table 5.1. List of parameters employed in the model.

Symbol	Definition	Value
$r_{0,A}$	Length of an actin segment	1.4×10^{-7} [m]
$r_{c,A}$	Diameter of an actin segment	7.0×10^{-9} [m] [69]
$\theta_{0,A}$	Bending angle formed by adjacent actin segments	0 [rad]
$\kappa_{s,A}$	Extensional stiffness of F-actin	1.69×10^{-2} [N/m]
$\kappa_{b,A}$	Bending stiffness of F-actin	2.64×10^{-19} [N·m] [70]
$r_{0,ACP}$	Length of an ACP arm	2.35×10^{-8} [m] [71]
$r_{c,ACP}$	Diameter of an ACP arm	1.0×10^{-8} [m]
$\theta_{0,ACP}$	Bending angle formed by two ACP arms	0 [rad]
$\kappa_{s,ACP}$	Extensional stiffness of ACP	2.0×10^{-3} [N/m]
$\kappa_{b,ACP}$	Bending stiffness of ACP	0 [N·m]
$r_{0,M}$	Length of a motor arm	1.35×10^{-8} [m]
$r_{c,M}$	Diameter of a motor arm	1.0×10^{-8} [m]
$\kappa_{s,M}$	Extensional stiffness of a motor arm	1.0×10^{-3} [N/m]
N_h	Number of heads represented by a motor arm	4
N_a	Number of arms in each motor	1 or 2

Table 5.1 continued

$k_{\text{n,A}}$	Nucleation rate of actin for network formation	0.0022 [$\mu\text{M}^{-1}\text{s}^{-1}$]
	Nucleation rate of actin for networks with turnover	0.15 [$\mu\text{M}^{-1}\text{s}^{-1}$]
$k_{\text{+,A}}$	Polymerization rate of actin at the barbed end for network formation	60000 [$\mu\text{M}^{-1}\text{s}^{-1}$]
	Polymerization rate of actin at the barbed end for networks with turnover	0.1-70 [$\mu\text{M}^{-1}\text{s}^{-1}$]
$k_{\text{-,A}}$	Depolymerization rate of actin at the pointed end for network formation	0 [s^{-1}]
	Depolymerization rate of actin at the pointed end for networks with turnover	0.1-70 [s^{-1}]
$k_{\text{u,ACP}}^{0*}$	Reference value of the zero-force unbinding rate constant of ACP	0.115 [s^{-1}] [68, 71]
$\lambda_{\text{u,ACP}}$	Sensitivity of ACP unbinding to applied force	1.04×10^{-10} [m] [68]
κ_{r}	Strength of repulsive force	1.69×10^{-3} [N/m]
Δt	Time step	1.5×10^{-5} [s]
μ	Viscosity of medium	8.6×10^{-1} [kg/m·s]
$k_{\text{B}}T$	Thermal energy	4.142×10^{-21} [J]
C_{A}	Actin concentration	100 [μM]
N_{M}	Number of motors in a network	0-100
R_{ACP}	Ratio of ACP concentration to actin concentration	0.01-0.1
$\langle L_{\text{f}} \rangle$	Average length of F-actins	1.2-3.9 [μm]

Table 5.2. List of parameter values used for adopting "parallel cluster model." [72, 73]

Symbol	Definition	Value
k_{01}	A rate from unbound to weakly bound state	40 [s^{-1}]
k_{10}	A rate from weakly bound to unbound state	2 [s^{-1}]
k_{12}	A rate from weakly bound to post-power-stroke state	1000 [s^{-1}]
k_{21}	A rate from post-power-stroke to weakly bound state	1000 [s^{-1}]
k_{20}	A rate from post-power-stroke to unbound state	5-640 [s^{-1}]
F_0	Constant for force dependence	5.04×10^{-12} [N]
E_{pp}	Free energy bias toward the post-power-stroke state	-60×10^{-21} [J]
E_{ext}	External energy contribution	0 [J]
d	Step size	7×10^{-9} [m]
k_{m}	Spring constant of the neck linkers	1.0×10^{-3} [N/m] ($=\kappa_{\text{s,M}}$)

5.2.2 Dynamics of motors

Two types of motors are used in this study: one-arm motors can bind to only one F-actin, whereas two-arm motors can bind to a pair of F-actins. Two-arm motors can represent a cargo transported by more than one myosin motor in context of active transport and also represent myosin thick filaments that can bind to more than one F-actin [159]. Indeed, effects of connectivity between a motor and multiple F-actins on active transport have been considered in a recent study [157].

After binding to F-actin, each motor arm can either unbind from F-actin or walk toward the barbed end of F-actin in force-dependent manners. The force-dependent unbinding ($k_{u,M}$) and walking ($k_{w,M}$) rates of motor arms are determined by the parallel cluster model (PCM) which accounts for cooperative behaviors of several myosin heads with consideration of mechanochemical cycles [72, 73]. The implementation and benchmark of PCM into our model are explained in detail in our previous study [61]. In general, $k_{u,M}$ and $k_{w,M}$ generated from PCM have tendency to decrease as forces exerted on motor arms increase (Fig. 5.2). Thus, a motor arm eventually stops walking if motor arms experience forces beyond stall level which is ~3.8 pN per myosin head. If motor arms reach the barbed end of F-actin, they slide off from F-actin by a next walking event. After slide-off or unbinding, motor arms can bind to different F-actin, resulting in hopping from one F-actin to the other. If all arms of a motor lose connection to F-actin, the motor diffuses in the medium until one of its arms binds to another F-actin. We explicitly account for such diffusion in a free state because diffusion may play a significant role in motor motions as suggested in a previous study [140].

One-arm motors cannot generate large forces because drag forces acting on the center of the motors are not strong enough to resist reaction forces from F-actins, as one cannot exert a large force on a rope by pulling it on a slippery surface. On the contrary, two-arm motors can develop large forces on F-actins if they are bound to relatively anti-parallel F-actins, as one can exert large forces on two ropes by pulling them with both hands in opposite directions even on a very slippery surface.
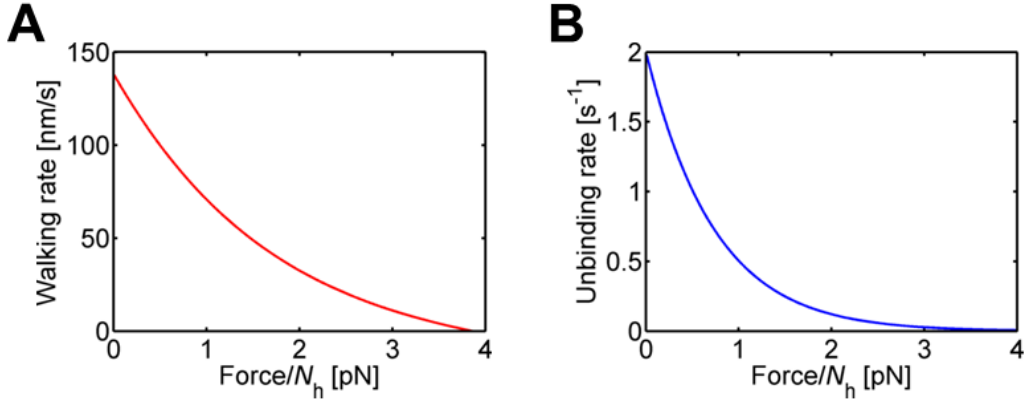
Figure 5.2. Force-dependent behaviors of motors. (A) Walking and (B) unbinding rates of a motor arm as a function of a force acting on the arm. N_h is the number of heads represented by each motor arm. Since the unbinding rate decreases with higher applied force, the motor arm behaves as a catch bond.

5.2.3   Network assembly

In each simulation, motors walk on a pre-assembled network. If motors walk during network assembly, network morphology can become highly different at the beginning of measurement of motor motions. Then, it is hard to compare cases in different conditions since motors in those cases walk on a different structure from the beginning. To avoid this issue, we assembled networks without motors, then imported the pre-assembled network into each simulation with motors. Note that preassembly of networks without motor activities has been employed in previous in vitro experiments [160].

For network formation, a cross-linked actin network is assembled via dynamic events of F-actins and ACPs in a three-dimensional thin rectangular domain ($5 \times 5 \times 0.2\mu$m) with a periodic boundary condition only in x and y directions (Fig. 5.1b). In all simulations, nucleation of F-actins takes place in a random direction perpendicular to the z direction at equal probabilities, followed by fast polymerization. This initially results in formation of a cortex-like network with randomly oriented F-actins. ACPs bind to a pair of F-actins to form a functional cross-link between F-actins.

By varying cross-linking density (R_{ACP}) and average F-actin length ($<L_f>$), we are able to control network connectivity. Larger R_{ACP} and $<L_f>$ lead to formation of networks with higher connectivity. If ACPs cannot unbind from F-actins, a network remains homogeneous until the end of simulations. By contrast, with transient ACPs that can unbind, it was observed that F-actins tend to gradually form bundles over time under conditions of high connectivity, which is consistent

with previous in vitro studies [161, 162] and a computational study [163]. In general, it takes a while for such a network to reach a steady-state configuration. If the slow transition to a bundled network occurs while motors walk on the network, patterns of motor motions inevitably become time-variant because geometry of a network where motors walk keeps changing over time. In addition, it is computationally inefficient to delay activation of motor walking in each simulation until a network reaches a steady state. Thus, we ran a few simulations in the absence of motors for 1000 s to generate networks that reached a steady state in terms of network morphology. Then, we imported these steady-state networks at the beginning of the simulations in order to quantify motions of motors without significant influences of F-actin bundling.

5.2.4   Evaluation of motions of motors

We evaluate motions of motors in a network in three ways. First, we calculate time-averaged, ensemble-averaged mean squared displacement (TE-MSD):

$$\text{TE-MSD}(\tau) = \frac{1}{N}\sum_{i=0}^{N}\left(\frac{1}{T-\tau}\int_{0}^{T-\tau}\left\|\mathbf{r}_i(t+\tau)-\mathbf{r}_i(t)\right\| dt\right)^{2} \tag{5.1}$$

where N is the number of motors, T is the duration of a simulation, τ is the lag time, $\mathbf{r}_i$ is the position vector of the ith motor, and t is time. TE-MSD(τ) indicates how far motors are displaced for τ on average.

Second, we calculate ensemble-averaged mean squared displacement (E-MSD) that represents how far motors are displaced on average for τ from an initial position at $t = 0$:

$$\text{E-MSD}(\tau) = \frac{1}{N}\sum_{i=0}^{N}\left(\left\|\mathbf{r}_i(\tau)-\mathbf{r}_i(0)\right\|^{2}\right) \tag{5.2}$$

If the nature of motor motions is almost time-invariant (i.e. ergodic), TE-MSD would be very similar to E-MSD [157]. By comparing E-MSD and TE-MSD with reference curves indicating $\sim\tau^{1}$ and $\sim\tau^{2}$, we estimate the local power-law exponent α which is indicative of the nature of motions. $\alpha < 1$, $\alpha = 1$, $1 < \alpha < 2$, and $\alpha = 2$ indicate subdiffusive, diffusive, superdiffusive, and ballistic motions, respectively.

Third, we fix the lag time (τ) and calculate ensemble-average mean squared displacement during the lag time at each time point t, which is named τ-MSD:

$$\tau\text{-MSD}(t) = \frac{1}{N}\sum_{i=0}^{N}\left(\left\|\mathbf{r}_i(t+\tau)-\mathbf{r}_i(t)\right\|^2\right) \tag{5.3}$$

τ-MSD provides information about motor motions at each time point.

TE-MSD and E-MSD have been used in previous studies with different names [153, 157, 164]. τ-MSD was often averaged from the beginning to different time points (i.e. measurement time) to determine whether motions undergo an aging process induced by confinement or trapping [153, 157, 164]. Unlike the previous studies, we used τ-MSD at each time point to understand when motor motions start slowing down. In the previous studies, τ used for calculating τ-MSD ranges between 5 s and 15 s [153]. We found that with higher τ, τ-MSD is larger, but the shape of all curves does not change significantly (Fig. 5.3). Thus, we set τ to 10 s for calculating τ-MSD. We calculated TE-MSD, E-MSD, and τ-MSD using 10-100 motor trajectories (Figs. 5.4, 5.7). and took the average.
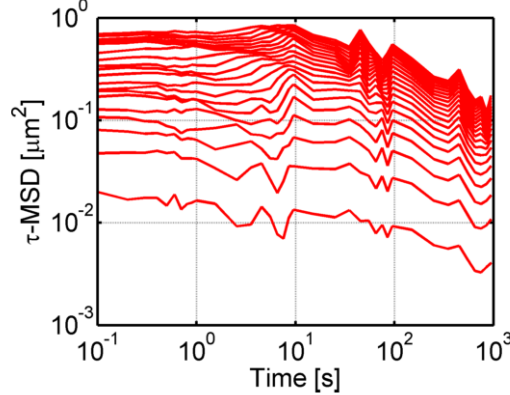
Figure 5.3. (A) τ-MSD with lag time (τ) ranging from 1 s to 20 s for a case shown by a red solid curve in Fig. 5.5B. As τ is higher, values of τ-MSD tend to be larger. Overall, the shape of the curves is similar to each other. We chose 10 s for a fixed value of τ (τ = 10s) used for calculating τ-MSD in all other figures.
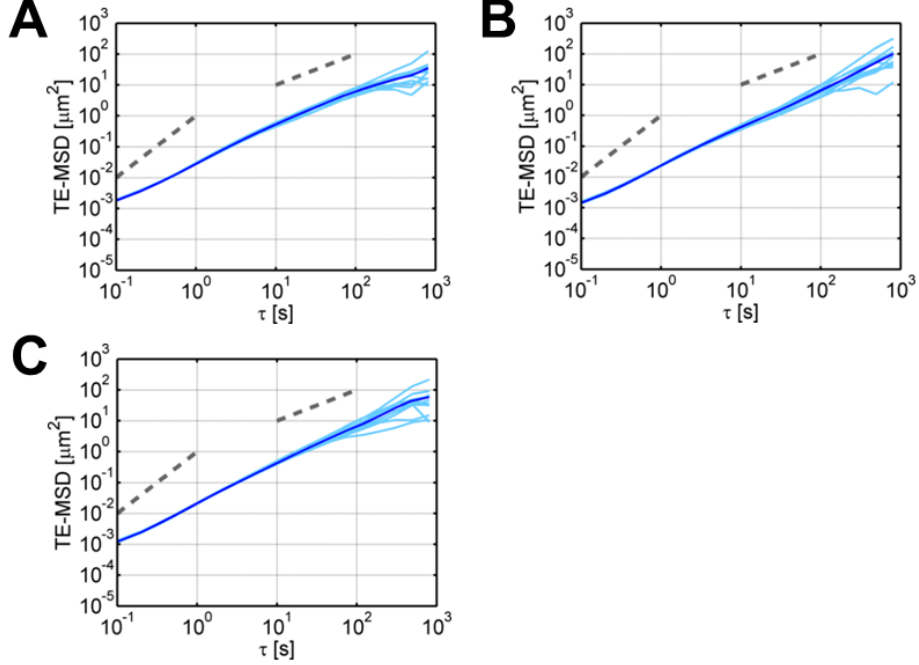
Figure 5.4. TE-MSD of one-arm motors in networks with (A) low, (B) medium, and (C) high connectivity. In each simulation, there were 5 motors ($N_M = 5$) in the absence of ACP unbinding and F-actin turnover. Cyan curves show TE-MSD of individual motors. Blue curves represent the ensemble average of all cyan curves, corresponding to red, blue, and green dashed lines shown in Fig. 5.5B. Gray dashed lines indicate the slope of MSD corresponding to diffusive motions ($\sim \tau^1$) and ballistic motions ($\sim \tau^2$).

5.2.5   Evaluation of F-actin confinement

To indirectly estimate elasticity of actin networks, we calculate TE-MSD of all actin segments (e.g. Fig. 5.5A). In our previous study, we showed a correlation between TE-MSD of F-actins and network elasticity [43]. If F-actins are well connected due to more ACPs or longer F-actins, F-actins cannot move freely, resulting in lower TE-MSD which implies higher network stiffness [43, 165]. By contrast, if F-actins are loosely connected, F-actins can move more freely, leading to higher TE-MSD which implies lower network stiffness. We evaluate TE-MSD of actin segments only in cases with 5 motors to avoid network stiffening induced by many motors so that TE-MSD is determined largely by network connectivity regulated via R_{ACP} and $<L_f>$.

Figure 5.5. Motions of one-arm and two-arm motors in networks with different connectivity. In each simulation, 5 motors were used ($N_M = 5$), and ACP unbinding and F-actin turnover were not incorporated. (A) TE-MSD (time- and ensemble-averaged mean squared displacement) of actins in networks with low, medium, and high connectivity. Networks with higher connectivity exhibit much lower TE-MSD, implying that movements of F-actins are confined more if connectivity is higher. (B) TE-MSD of one-arm and two-arm motors. Gray dashed lines indicate the slope of MSD corresponding to diffusive motions ($\sim\tau^1$) and ballistic motions ($\sim\tau^2$). Two-arm motors show much lower TE-MSD in networks with medium and high connectivity, whereas one-arm motors exhibit similar TE-MSD regardless of network connectivity. (C) Average force exerted on each myosin head in motor arms, which is the ensemble average of time average of forces acting on motor arms, divided by the number of heads represented by each motor arm (N_h). One arm motors bear very small force (~0.1 pN) because they cannot generate force on F-actins. By contrast, two-arm motors bound to relatively antiparallel F-actins can generate high force. (D) The fraction of stalling indicating how long motors are stalled during a simulation run up to $t = 1000$ s. One-arm motors do not experience force-induced stalling due to very small force acting on their arms, whereas two-arm motors are stalled significantly.

5.2.6   Quantification of heterogeneity and aggregation of networks

Under certain conditions, a network tends to aggregate due to motor activity, resulting in heterogeneous network morphology. We analyzed the extent of aggregation and network heterogeneity using the radial distribution function, $g(r)$, that represents density of particles as a function of a radial distance from a particle [158]. First, a particle density ρ is calculated by assuming that all particles are uniformly distributed throughout an entire region. Then, at a distance

135

r from a particle, the number of particles in a donut-shaped region with small thickness Δr is counted (Fig. 5.6A). Note that the area of the donut-shaped region is approximately $2\pi r \Delta r$, and the number of particles in the donut-shaped region, $P(r)$, is normalized by $2\pi r \Delta r \rho$. The normalized value at the distance r is calculated with respect to all particles, and all normalized values are averaged into $g(r)$.

$$g(r) = \left\langle \frac{P(r)}{2\pi r \Delta r \rho} \right\rangle \tag{5.4}$$

If particles are distributed uniformly, $g(r)$ is close to one. Conversely, $g(r) > 1$ represents aggregation of particles near the distance r, and $g(r) < 1$ indicates the sparse distribution of particles near the distance r. At every 100 s, we calculate $g(r)$ using instantaneous positions of actin segments with $\Delta r = 20$ nm (Fig. 5.6B). Then, we average values of $g(r)$ at 0.1 µm $< r <$ 1 µm to obtain $\bar{g}(t)$. The lower limit (0.1 µm) is an approximate distance at which $g(r)$ becomes higher than 1, and the upper limit (1 µm) is an approximate distance beyond which $g(r)$ shows no significant change. Then, the highest value of $\bar{g}(t)$ found in a simulation ($\bar{g}_{max}$) is divided by the initial value calculated at the beginning of the simulation ($\bar{g}_{init}$) as a measure of network aggregation. Higher "$\bar{g}_{max} / \bar{g}_{init}$" indicates more severe network aggregation.
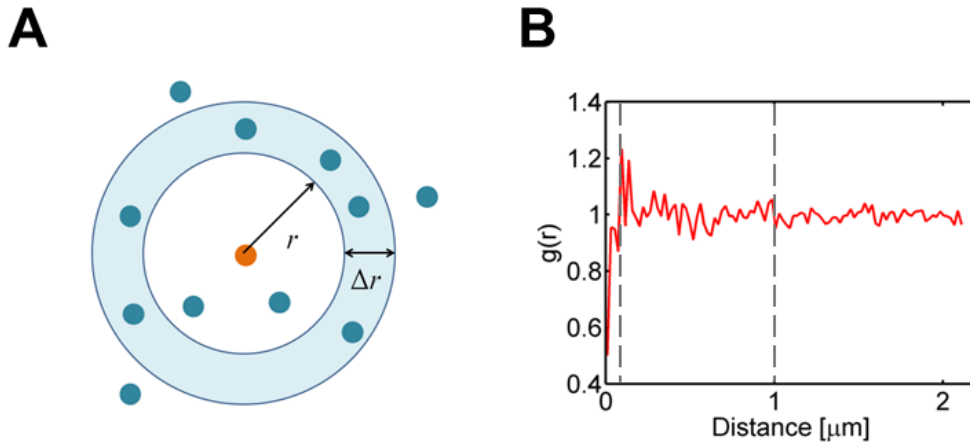
Figure 5.6. Quantification of the extent of network heterogeneity. (A) A schematic diagram showing how the radial distribution function, $g(r)$, is calculated. (B) An example of $g(r)$ calculated using a network with low connectivity. Two dashed lines indicate the range of r used for calculation of the average value, $\bar{g}(t)$.

5.2.7 Experimental methods

To verify some of the hypotheses derived from simulations, we employ an in vitro experimental model of the cell cortex. Unlike simulations where non-muscle myosin II was modeled, we used skeletal muscle myosin in experiments. Since we are interested in tracking individual motors, we could not use non-muscle myosins in experiments due to a limitation in tagging those myosins.

The in vitro model followed the method previously described [166]. On a plasma-cleaned glass coverslip, we generate a lipid bilayer consisting of a mixture of 100:1 egg phosphatidylcholine:Oregon Green 488 DHPE lipids. F-actins are pre-polymerized at concentration of 2.64 µM G-actin in F-buffer (50 mM KCl, 1 mM MgCl$_2$, 10 mM Imidazole, 200 µM EGTA, and 500 µM ATP at pH 7.5) and stabilized with 1.32 µM phalloidin. We use 75:25 as a ratio of dark to fluorescently labeled G-actin. Pre-polymerized F-actins are crowded onto the lipid bilayer with 0.25% 14kDa MW methylcellulose, and then glucose oxidase (0.25% mg/mL), catalase (0.05 mg/mL), and glucose (25 mM) are added to the imaging chamber to minimize photobleaching.

α-actinin aliquots and fluorescently labeled myosin are snap frozen and freshly thawed immediately before use. We centrifuge myosins immediately before use in the presence of stabilized pre-polymerized F-actins and high ATP to remove inactive motors. α-actinin and myosin are added to the imaging chamber after F-actins are fully crowded onto the lipid bilayer.

5.3 Results

In this study, we investigated effects of several factors on motions of motors, such as network connectivity, reversibility of cross-links, F-actin turnover, the number of motors, and connectivity between motors and F-actins. For network connectivity, we used three different conditions: low, medium, and high. Average filament length ($<L_f>$) for low, medium, and high connectivity is 1.2 µm, 2.3 µm, and 3.9 µm, respectively. Cross-linking density (R_{ACP}) for low, medium, and high connectivity is 0.01, 0.04, and 0.1, respectively.

5.3.1 Motors are stalled by locally generated forces in networks with high connectivity

First, we analyzed motions of one-arm and two-arm motors in networks with three different connectivity levels. It was assumed that ACPs form permanent cross-links without the possibility of unbinding (i.e. $k_{u,ACP}^{o} = 0$), and F-actins do not undergo turnover (i.e. $k_{t,A} = 0$). Although this condition is less physiologically relevant since F-actins and most kinds of the ACPs turn over in cells, we used this condition as a control case to understand effects of ACP unbinding and F-actin turnover on motor motions.

F-actins in networks with higher connectivity show much lower TE-MSD of actins, implying that F-actins are confined more (Fig. 5.5A). As shown in our previous study [43], highly confined F-actins are indicative of larger network elasticity. We found that the magnitude of TE-MSD of one-arm motors is larger than that of two-arm motors in general (Fig. 5.5B, 5.8A). In addition, at $\tau < 100$ s, the slope of TE-MSD of one-arm motors is higher than that of two-arm motors (Fig. 5.8B). One-arm motors cannot generate large forces because they can bind to only one F-actin (Fig. 5.5C). Thus, they are able to walk along F-actins for a long time without force-induced stalling (Fig. 5.5D). It is noteworthy that TE-MSD and E-MSD measured from motions of one-arm motors are similar to each other, meaning that motions are more "ergodic" (Figs. 5.5B, 5.7D). Interestingly, in the case with one-arm motors, the magnitude and slope of TE-MSD are lower in a network with low connectivity at $\tau > 100$ s, compared to networks with medium and high connectivity (Fig. 5.5B). At this time range, the slope is smaller than one, indicating subdiffusive motions. With a small number of ACPs and short F-actins, thermal fluctuation of F-actins and forces exerted on F-actins by motors can make F-actins move substantially as high TE-MSD values of F-actins imply (Fig. 5.5A). Therefore, movement of F-actins can cause motor movement to deviate from ballistic motions even when motors are walking along F-actins without stalling, thus resulting in lower magnitude and slope of TE-MSD at $\tau > 100$ s.
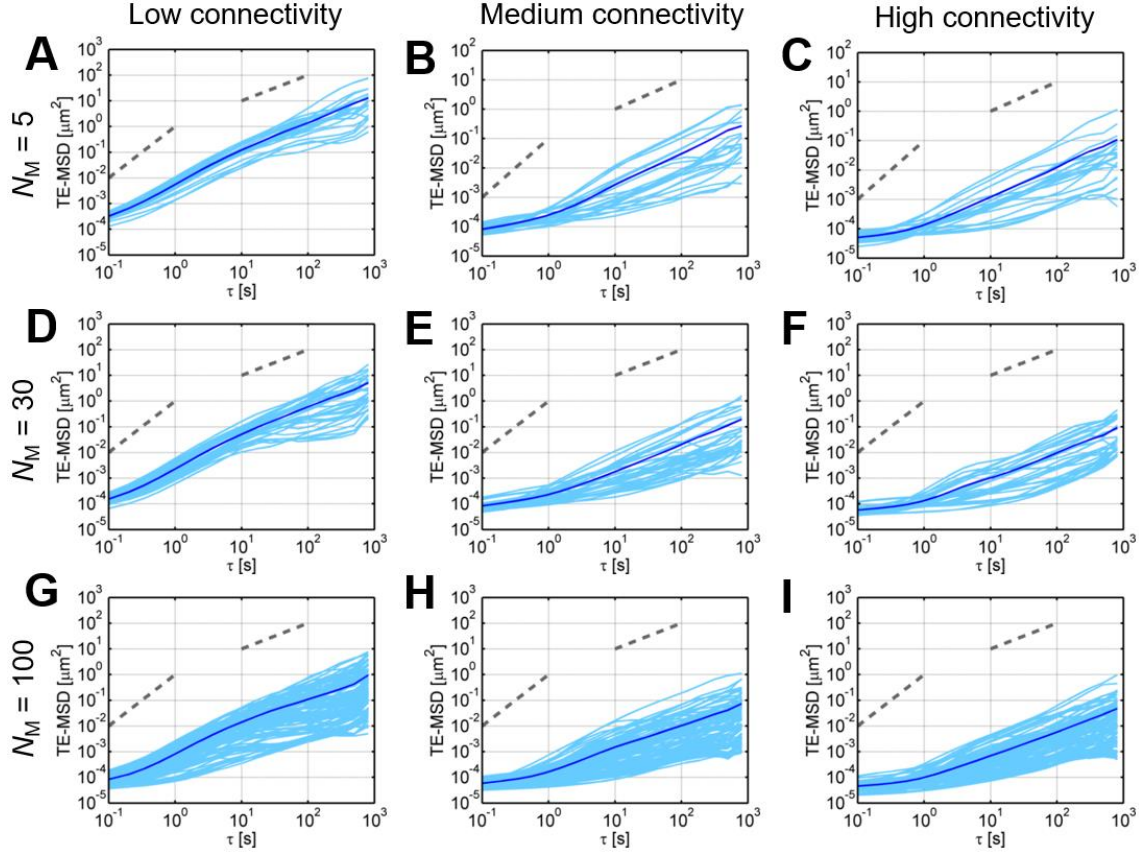
Figure 5.7. TE-MSD of two-arm motors in networks with low, medium, and high connectivity and $N_M = 5$, 30, and 100 without ACP unbinding and F-actin turnover. Cyan curves show TE-MSD of individual motors. Blue curves represent the ensemble average of all cyan curves, corresponding to 9 curves shown in Fig. 5.10A. Gray dashed lines indicate the slope of MSD corresponding to diffusive motions ($\sim\tau^1$) and ballistic motions ($\sim\tau^2$).

TE-MSD of two-arm motors in all cases is smaller than those of one-arm motors. As network connectivity increases, the magnitude and slope of TE-MSD in cases with two-arm motors noticeably decrease (Figs. 5.5B, 5.8A, 5.8B). This can be explained by force-induced stalling. Unlike one-arm motors, two-arm motors can generate large forces if they bind to two F-actins oriented in relatively anti-parallel directions. Forces are generated better by motors in networks with high connectivity (Fig. 5.5C) because F-actins are confined tightly (Fig. 5.5A); two-arm motors can easily develop forces on tightly confined F-actins by pulling them. As a result, two-arm motors in networks with medium and high connectivity spend most of time in a stalling state (Fig. 5.5D). Since TE-MSD is calculated by averaging squared displacements over an entire time range, it is hard to estimate how long motors walk on average before force-induced stalling. τ-MSD and E-MSD can provide useful information about this (Figs. 5.8C, D). In the network with

low connectivity, the slope of E-MSD and the magnitude of τ-MSD become smaller after $t \sim 50$ s, implying that two-arm motors walk for ~50 s on average before stalling. In the networks with medium and high connectivity, such changes in E-MSD and τ-MSD start between ~ 1 s and ~10 s, indicating that it takes less time for two-arm motors to be stalled in these networks.
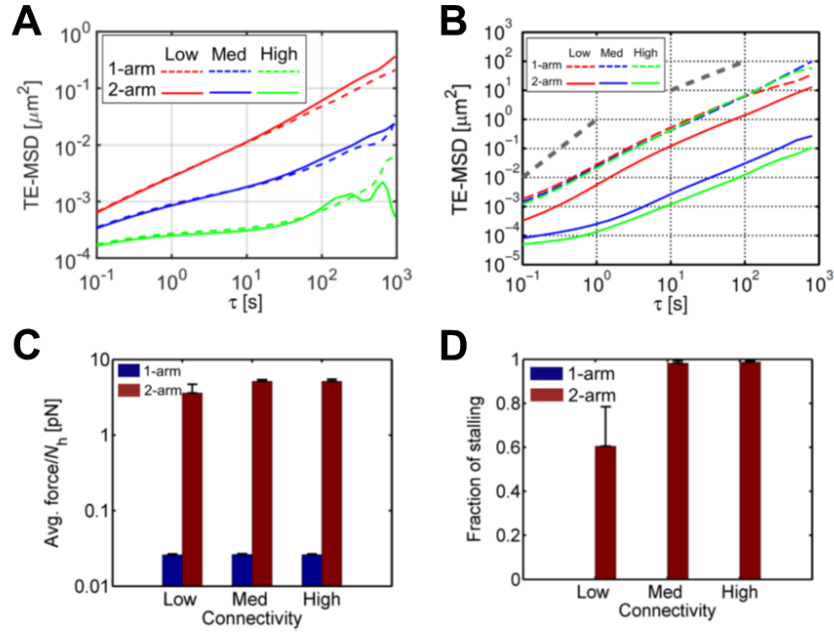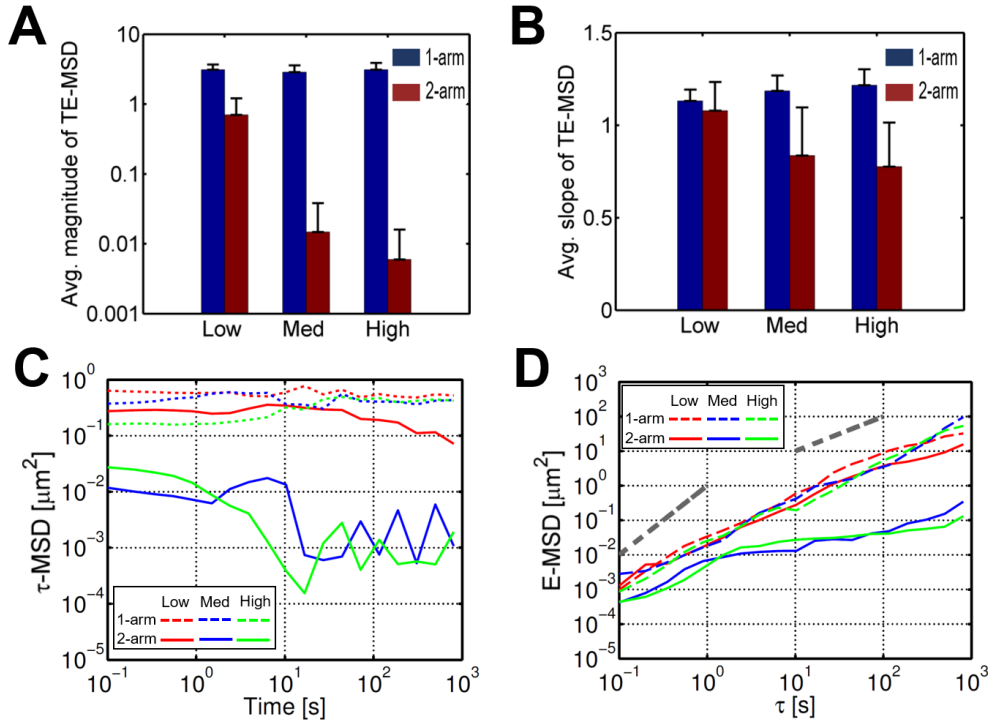

Figure 5.8. Motions of one-arm and two-arm motors in networks with different connectivity. In each simulation, 5 motors were used ($N_M = 5$), and ACP unbinding and F-actin turnover were not included. (A) Magnitude and (B) slope of TE-MSD of motors averaged at $\tau = 0.1\text{-}100$ s. Unlike one-arm motors, the magnitude and slope of TE-MSD of two-arm motors are inversely proportional to network connectivity. (C) τ-MSD and (D) E-MSD of motors. In cases with one-arm motors, τ-MSD does not change significantly over time, and the slope of E-MSD does not depend much on τ. For two-arm motors, the magnitude of τ-MSD and the slope of E-MSD noticeably decrease from ~50 s in a low- connectivity network and decrease between ~1s and ~10 s in networks with medium and high connectivity. This indicates that motor stalling takes place earlier in the cases with medium and high network connectivity.

From the slope of E-MSD, we found that both one-arm and two-arm motors do not show ballistic movement even at short time scale ($\tau < 1$ s). This is attributed to frequent unbinding of motors from F-actins which leads to diffusion of motors and hopping to other F-actin (Fig. 5.2B). In addition, in cases with a low-connectivity network, relatively large movement of F-actins can make the trajectory of motors less straight even when motors are very processive. To confirm this

hypothesis, we analyzed motions of one-arm motors with much less frequent unbinding within a network with high connectivity (Fig. 5.9). We found that motors show nearly ballistic movement at an early time range ($\tau < 10$ s).
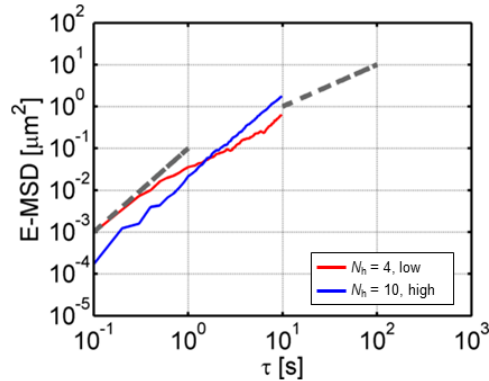
Figure 5.9. E-MSD of one-arm motors with different number of heads (N_h) and different network connectivity. Gray dashed lines indicate the slope of MSD corresponding to diffusive motions ($\sim\tau^1$) and ballistic motions ($\sim\tau^2$). Motors with $N_h = 10$ in a high-connectivity network show ballistic movement ($\sim\tau^2$). Motors with $N_h = 4$ in a low-connectivity network exhibit the slope of MSD smaller than 2. More frequent unbinding of motors with lower N_h (i.e. less processive) leads to more hopping or diffusion of motors, thus hindering ballistic motions. In addition, in the low-connectivity network, larger motions of F-actins (Fig. 5.5A) hinder ballistic motions.

In summary, we found that the amount of forces exerted on motors highly affects motions of motors in disordered networks. If motors can bind to only one F-actin, they tend to consistently walk for a long time without stalling because they cannot generate large forces. If motors can bind to two F-actins, motors can be stalled by locally generated forces to an extent proportional to confinement of F-actins to the network.

5.3.2   Motors can be stalled due to global force transmission through a network

It was shown that networks with more motors generate larger stress and show stronger contractile behaviors [63]. We probed effects of the number of motors (N_M) on motions of two-arm motors in the same three networks with different connectivity. All other conditions are the same as above. TE-MSD of motors walking in a network with low connectivity shows strong dependence on N_M (Fig. 5.10A); with a smaller number of motors, TE-MSD is higher. Such dependence of TE-MSD on N_M is consistent with changes in average force generated by motors and the fraction of motor stalling. As N_M increases, the average force becomes larger than the stall

force, and the fraction of stalling is much higher (Fig. 5.10B, C). This implies that motors are stalled by high forces even in a network with low connectivity if there are a larger number of motors. Although motors may contribute to enhancement of cross-linking level by acting as a tentative cross-linker, 100 motors cannot make the cross-linking density high enough to reduce TE-MSD. Note that the number of ACPs in a network with low connectivity is 1,504, which is much larger than 100.

Figure 5.10. Motions of two-arm motors in networks with different connectivity and different number of motors (N_M). ACP unbinding and F-actin turnover were not considered in these simulations. (A) TE-MSD (time- and ensemble-averaged mean squared displacement) of motors. Gray dashed lines indicate the slope of MSD corresponding to diffusive motions ($\sim\tau^1$) and ballistic motions ($\sim\tau^2$). In a network with low connectivity, higher N_M leads to lower TE-MSD. (B) Average force exerted on each myosin head in motor arms, which corresponds to the ensemble average of time average of forces acting on motor arms, divided by the number of heads represented by each motor arm (N_h). For $N_M > 10$, the average force increases with N_M in a network with low connectivity, resulting in higher average force at $N_M = 100$ than that in networks with medium and high connectivity. (C) The fraction of stalling indicating how long motors are stalled during a simulation run up to $t = 1000$ s. Motors are mostly stalled in networks with medium and high connectivity, regardless of N_M. In a network with low connectivity, the fraction of stalling increases at $N_M > 10$, which is consistent with the increase in the average force shown in (B). (D) Visualization of networks at 800 s. Blue, white, and red represent low, intermediate, and high forces, respectively. Only actins and motors bearing high forces (> 25 pN) are visualized. In a network with low connectivity and high N_M, adjacent motors are connected via force-bearing F-actins, indicating force transmission between the motors.

We hypothesized that this can be attributed to mechanical interactions via force transmission between motors. Tensile forces generated by motors can be transmitted to other

143

motors through taut F-actins and ACPs that physically connect the motors, which can result in an increase in forces acting on the other motors. This is similar to mechanical interations between myosin molecules occurring within a thick filament; a power stroke motion of one myosin molecule on F-actin can develop forces on other myosin molecules bound to different or the same F-actin via the backbone of the thick filament. To confirm this hypothesis, we visualized large forces (> 25 pN) acting on F-actins and motors (Fig. 5.10D). In the low-connectivity network with $N_M = 100$, F-actins between neighboring motors bear a large amount of forces, which clearly demonstrates mechanical interactions between the neighboring motors. Motors create a web-like structure bearing large forces, and such large forces are not observed in other parts of the network (Fig. 5.10D).

In networks with medium and high connectivity, dependence of TE-MSD on N_M is much weaker (Fig. 5.10A). In addition, forces exerted on motors and the fraction of motor stalling do not vary due to a change in N_M (Figs. 5.10B, C). Forces acting between motors increase with larger N_M, but the degree of the increase is less than that observed in the low-connectivity network (Fig. 5.10D). Indeed, fewer neighboring motors mechanically communicate (i.e. fewer motors connected by F-actin with high forces) compared to those in the low-connectivity network, so the web-like structure is not observed in networks with medium and high connectivity. This indicates that motors in networks with medium and high connectivity tend to exert forces to their vicinity rather than other motors located distantly. τ-MSD and E-MSD show that it takes ~10 s on average for 100 motors to be stalled in the low-connectivity network (Figs. 5.11A, B). By contrast, in networks with higher connectivity, motors are stalled soon (~ 1 s) after they start walking. In networks with higher connectivity, motors can be stalled quickly by reaction forces from F-actin at cross-linking points or between anti-parallel F-actins located near their initial positions. On the other hand, in networks with low connectivity, motors keep moving until they find one of a few positions where they can generate large forces and feel forces transmitted from other motors to form the web-like structure, thus resulting in a longer time before being stalled.

Figure 5.11. Motions of two-arm motors in networks with different connectivity and different number of motors (N_M). In these simulations, ACP unbinding and F-actin turnover were not included. (A) τ-MSD and (B) E-MSD of motors. The magnitude of τ-MSD and the slope of E-MSD for a low-connectivity network start decreasing later than those for medium- and high-connectivity networks. The case with $N_M = 100$ and low network connectivity shows much lower values of τ-MSD and E-MSD compared to those with $N_M = 5$ and 30, indicating much slower motor motions resulting from global force transmission as explained in the text.

In summary, two-motors walking in the low-connectivity network without ACP unbinding and F-actin turnover can be stalled by global force transmission between motors if the number of motors is large. However, in networks with higher connectivity, motors are stalled quickly by locally generated forces, so global force transmission plays an insignificant role in motor stalling.

5.3.3 Motions of motors can be confined by F-actin aggregation

Unlike the assumption used above, most of ACPs existing in cells form transient cross-links because they unbind stochastically from F-actins in a force-dependent manner [68, 167]. We ran simulations under the same conditions as above but incorporated the force-dependent unbinding of ACPs (Eq. 1). TE-MSD of two-arm motors in networks with medium and high connectivity is not dependent on the number of motors (N_M) as strongly as in the cases without ACP unbinding (Fig. 5.12A). However, the magnitude of TE-MSD is much higher, and the average force exerted on motors and the fraction of stalling are significantly lower compared to the cases without ACP unbinding (Figs. 5.12A-C). In addition, in networks with medium and high connectivity, τ-MSD decreases from ~5 s but reaches a plateau at later times (Fig. 5.13A). The slope of E-MSD is also reduced at ~5 s but increases later (Fig. 5.13B). These imply that motors did not remain in the stalling state for a long time. Since forces acting on a network are relaxed

145

consistently by ACP unbinding, motors stalled by high local forces have an opportunity to resume walking. Although motors are stalled less, they still experience forces close to the stall force and thus walk more slowly than motors in the low-connectivity network, as seen in TE-MSD, E-MSD, and τ-MSD.

Figure 5.12. Motions of two-arm motors in networks with different connectivity and different number of motors (N_M). In these cases, ACPs are allowed to unbind from F-actins with the reference unbinding rate. F-actin turnover is not considered ($k_{t,A} = 0$). (A) TE-MSD (time- and ensemble-averaged mean squared displacement) of motors. Gray dashed lines indicate the slope of MSD corresponding to diffusive motions ($\sim\tau^1$) and ballistic motions ($\sim\tau^2$). In a network with low connectivity, higher N_M leads to lower TE-MSD after ~5 s. (B) Average force exerted on each myosin head in motor arms, which is the ensemble average of time average of forces acting on motor arms, divided by the number of heads represented by each motor arm (N_h). Motors in networks with medium and high connectivity experience much higher forces. (C) The fraction of stalling indicating how long motors are stalled during a simulation run up to $t = 1000$ s. Motors in networks with higher connectivity are stalled for a longer time, which is consistent with higher forces exerted on motor arms shown in (B). (D) Network heterogeneity quantified using the radial distribution function from positions of actins. Networks with low/medium connectivity high N_M exhibit aggregating behaviors. (E) TE-MSD of motors walking in reconstituted F-actin networks with low motor density. Cross-linking density is 0 (blue) or 0.1 (red). (F) A correlation between adjacent image frames showing only motors in (black and red) experiments and in (cyan and green) simulations. Cross-linking density is high in two cases represented by black and cyan and low in the other cases.
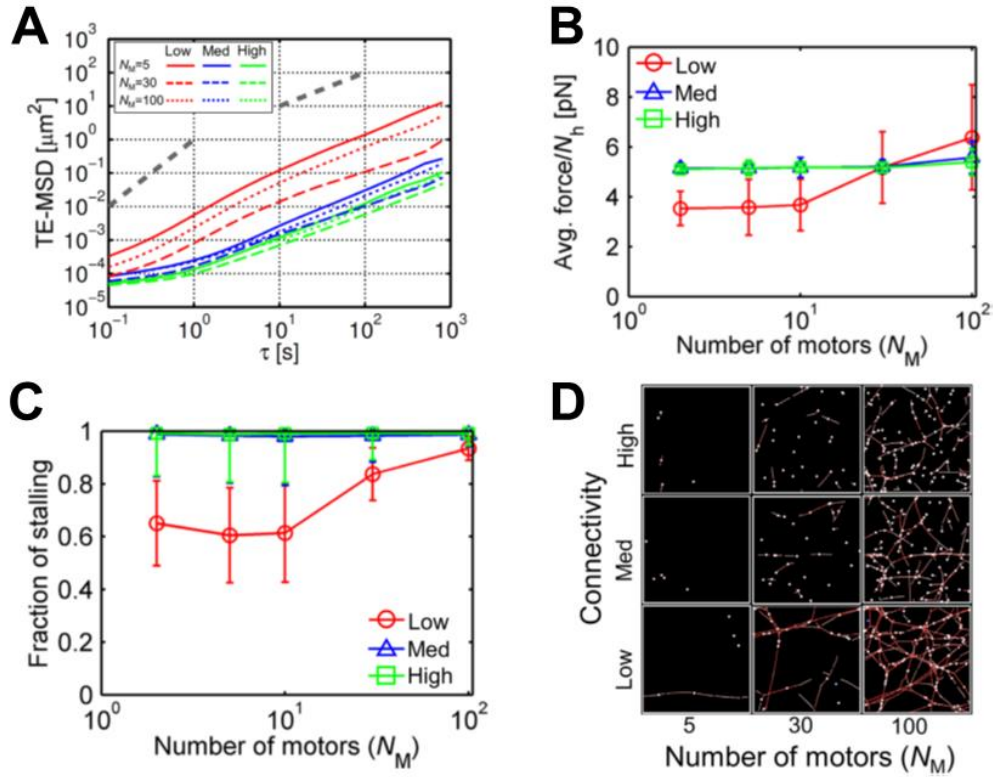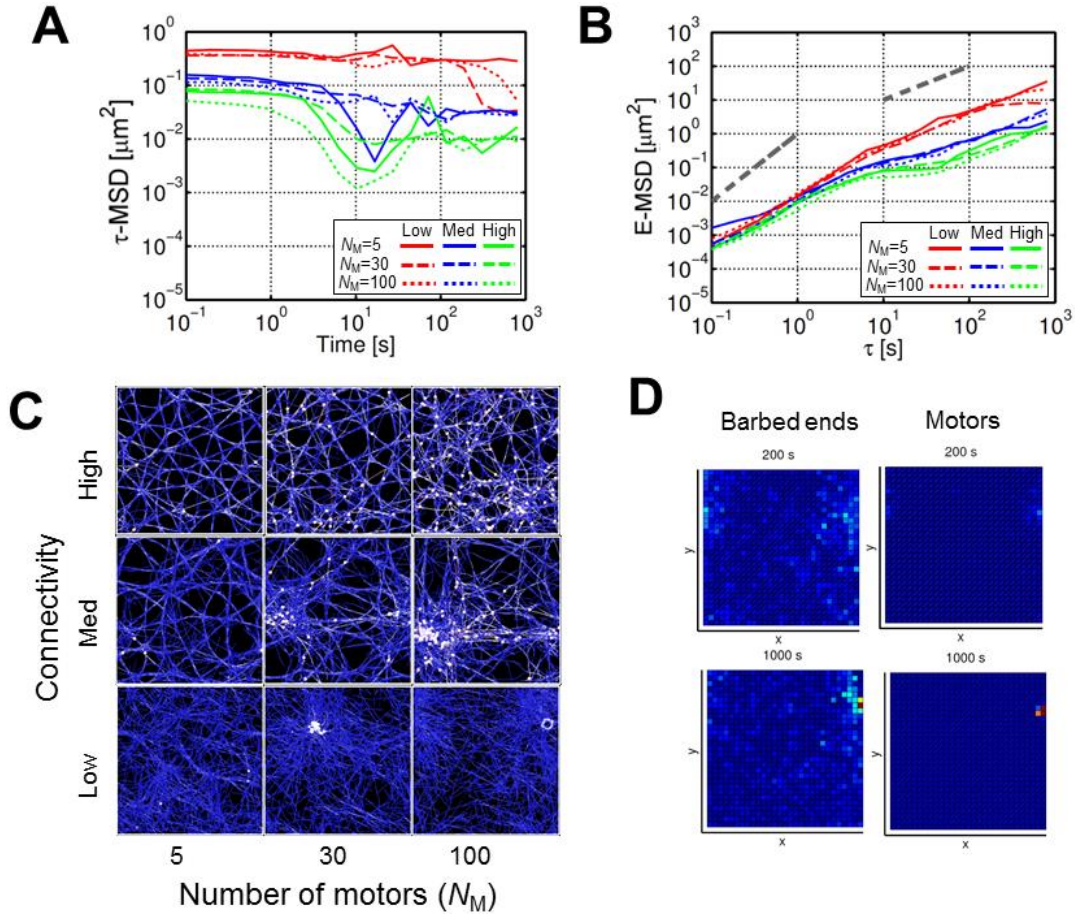
Figure 5.13. Motions of two-arm motors in networks with different connectivity and different number of motors (N_M) in the presence of ACP unbinding with the reference unbinding rate. F-actin turnover was not incorporated. (A) τ-MSD and (B) E-MSD of motors. For the low-connectivity network, the case with $N_M = 100$ shows lower values of τ-MSD and E-MSD at $t > \sim100$ s compared to the cases with $N_M = 5$ and 30. This is indicative of confined motor motions induced by network aggregation. (C) Visualization of networks at 800 s. Blue, white, and red represent low, intermediate, and high forces, respectively. Networks with $N_M \geq 30$ and low/medium connectivity exhibit severe aggregation of F-actins and motors. (D) Heat maps showing spatial distributions of the barbed ends of F-actins and motors in a case with a low-connectivity network with $N_M = 100$ shown in (C), at $t = 200$ s and 1000 s. Density is calculated by counting the number of elements in each grid of the computational domain and then dividing those numbers by the total number of elements. Motors and barbed ends are aggregated at the center of the aster-like structure, thus leading to confinement of motors without significant force generation.

TE-MSD of motors walking in the low-connectivity network shows dependence on N_M at $\tau > \sim5$ s. With higher N_M, TE-MSD tends to be lower although forces exerted on motors are lower (Figs. 5.12A, B). τ-MSD and the slope of E-MSD show a noticeable drop after ~100 s, meaning that motors walked relatively fast regardless of N_M before ~100 s (Fig. 5.13A, B). We found that

147

confinement of motor movements at high N_M is attributed to aggregation of a network. If many motors walk in a network with low connectivity, F-actins tend to form an aster-like structure (Figs. 5.12D, 5.13C). Additionally, it was shown that barbed ends are located near the center of the aster-like structure via polarity sorting [110]. Our results also shows that at the center of the aster-like structure, motors and barbed-ends are distributed more densly at later times (Fig. 5.13D). Then, once motors walk into the center, they cannot escape because there are few tracks oriented radially outward. However, they continuously move around the center region without force-induced stalling (Fig. 5.12B, C). In the aster-like structure, many of F-actins are oriented in a relatively parallel configuration due to the polarity sorting, and they are highly curved due to buckling occurring during aster formation [25]. Thus, a region near the center of the aster-like structure is not a favorable environment for two-arm motors to generate significant tensile forces. Thus, they rather keep walking along F-actins without stalling.

With 10-fold lower $\kappa_{u,ACP}^o$ (= 0.0115 s^{-1}), network aggregation still takes place in the low-connectivity network with high N_M (Fig. 5.14C), and similar dependences of TE-MSD and average motor forces on N_M were observed (Figs. 5.14A, B). However, with 100-fold lower $\kappa_{u,ACP}^o$ (= 0.00115 s^{-1}), the network does not aggregate significantly (Fig. 5.14F), and TE-MSD is almost independent of N_M (Fig. 5.14D). The average force exerted on motors increases with higher N_M (Fig. 5.14E), but it is not high enough to induce motor stalling for a long time. This implies that even slow ACP unbinding can prevent motor stalling induced by the global force transmission by slowly relaxing forces on a network.
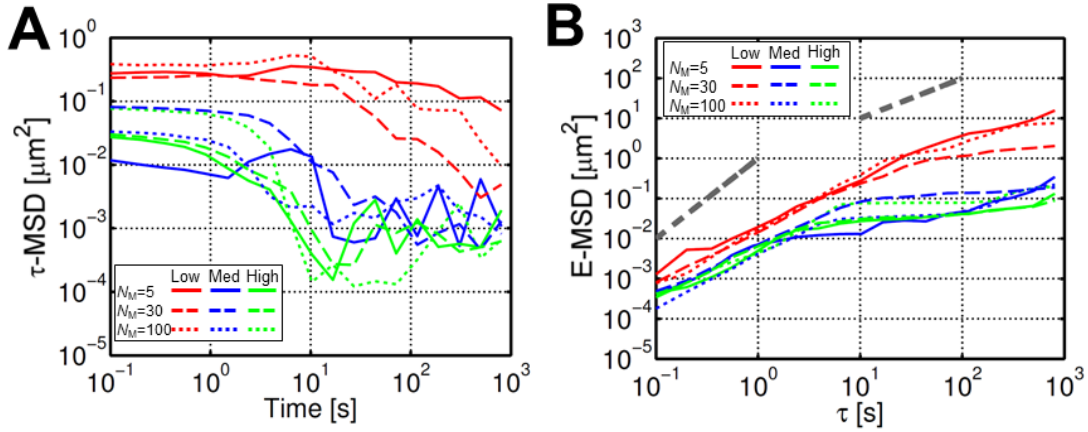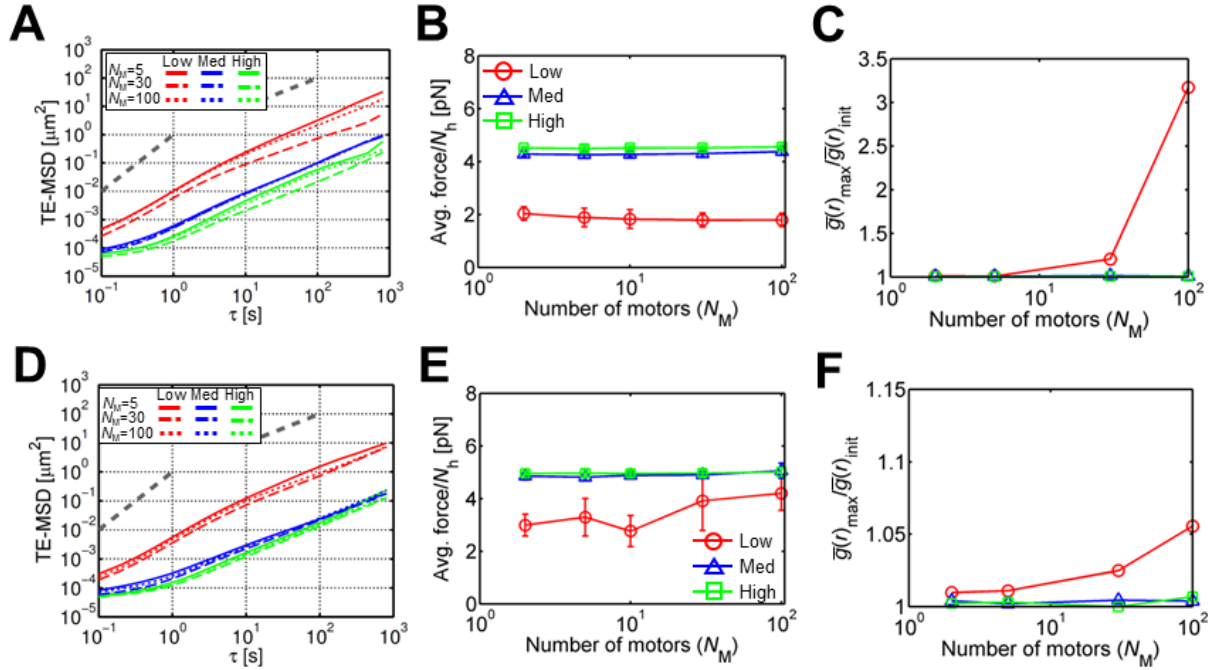
Figure 5.14. Motion of two-arm motors in networks with different connectivity and different number of motors (N_M) with slower ACP unbinding. Compared to the reference ACP unbinding rate, (A-C) 10-fold or (D-F) 100-fold smaller unbinding rate were used. F-actin turnover is not incorporated ($k_{t,A} = 0$). (A, D) TE-MSD of motors. (B, E) Average force exerted on each myosin head in motor arms. (C, F) Network heterogeneity quantified using a radial distribution function generated from positions of motors. Among cases with a low-connectivity network shown in (A-C), TE-MSD is lower, and network heterogeneity is higher with $N_M = 100$. This implies that motor confinement induced by network aggregation still takes place with a 10-fold smaller ACP unbinding rate. By contrast, with a 100-fold smaller unbinding rate, dependences of TE-MSD and network heterogeneity on N_M become much weaker. It indicates global force-induced stalling or motor confinement induced by network aggregation do not occur in these cases.

In sum, two-arm motors in networks with force-dependent unbinding of ACPs are not stalled permanently even with very high network connectivity because forces are relaxed consistently by ACP unbinding. If the network has low connectivity and a sufficient number of motors, it can severely aggregate. This can induce confinement of motors at the center of aggregates for a long time although the motors keep walking around the center.

5.3.4 Experimental measurements support the hypotheses for motor stalling and confinement

We qualitatively verified our hypotheses regarding the stalling and confinement of motors induced by force generation and aggregation, using reconstituted two-dimensional networks with

F-actin stabilized by phalloidin, α-actinin which transiently cross-links F-actins, and skeletal muscle myosin (SKMM). Skeletal muscle myosin is a highly non-processive motor which spends only ~4% of its lifetime in a bound state [76]. Hundreds of them are assembled into a long thick filament structure to stay on F-actin while they walk along F-actin fast [168]. Thus, admittedly, motors used in our in vitro experiments are quite different from those used in simulations in terms of the number of F-actins that they can bind simultaneously and total maximum force generated by one motor. In simulations, we can mimic behaviors of thick filaments consisting of skeletal muscle myosins by imposing the high ATP-dependent unbinding rate and the large number of myosin heads represented by each motor arm. In addition, our model can simulate a thick filament structure with multiple motor arms [61]. However, large forces generated by such motors prevented us from focusing mainly on motor motions without a significant change in network morphology. Thus, we decided to employ slightly non-processive, weak motors. However, due to the universal tendency of force-dependent walking and unbinding of different myosin isoforms, we can still make a qualitative comparison between some results from experiments and simulations to verify hypothesis.

First, with low motor density (0.5 nM SKMM), we conducted experiments with many ACPs (10:1 G-actin:α-actinin) and without any ACP. TE-MSD of motors is much lower in the case with high cross-linking density (Fig. 5.12E), which is consistent with simulation results (Fig. 5.12A). Note that values of TE-MSD measured in experiments are higher than those evaluated in simulations, which can be attributed to a large difference in walking velocity between SKMM (< ~5 μm/s) [76] and motors in simulations (< 140 nm/s) that intend to mimic behaviors of non-muscle myosins [74]. Still, the decrease in TE-MSD with high cross-linking density is consistent with our observation of force-induced motor stalling occurring at high R_{ACP}.

We repeated experiments with higher motor density (≥150 nM SKMM). Since many motors are closely located under this condition, tracking individual motors in images is not feasible. Thus, instead of quantifying MSD, we calculated a correlation between adjacent image frames showing only myosin motors in order to evaluate the extent of motions during each time interval. A correlation close to 1 indicates that motors hardly move between frames, whereas a lower correlation value is indicative of faster myosin movements between frames. With high connectivity (10:1 G-actin:α-actinin, 220 nM SKMM) (i.e. high cross-linking density), the correlation slightly

decreases at the beginning and then remains at ~1 (Fig. 5.12F). The correlation calculated using the simulation under similar conditions ($N_M = 100$ and high network connectivity) shows a qualitatively similar tendency. It implies that motors in both the experiments and the simulations hardly move over time. In the presence of only myosin motors (150 nM), severe network aggregation was observed as in the simulation (Fig. 5.13C). In both the experiment and the simulation, the correlation significantly drops at the beginning and is recovered to 1 after ~400 s (Fig. 5.12F). This implies that the network aggregates mostly at $t < 400$ s. Overall, correlations calculated in the experiments with high and low cross-linking density are consistent with our hypotheses for local force-induced stalling and confinement due to network aggregation.

5.3.5 Motor motions without F-actin turnover can be confined or stalled due to three reasons

The results that we have shown so far suggest three reasons for which motor motions are stalled or confined (Fig. 5.15): local force-induced stalling, global force-induced stalling, and confinement by network aggregation. First, local force-induced stalling occurs in networks with high connectivity without dependence on motor density (Fig. 5.15, blue). If there is no unbinding at all, motors can be stalled permanently in one location. As ACPs unbind more frequently, network connectivity needs to be higher to achieve motor stalling induced by locally generated forces. Even if ACP unbinding takes place very slowly, motors repeat walking and stalling over time without permanent stalling.
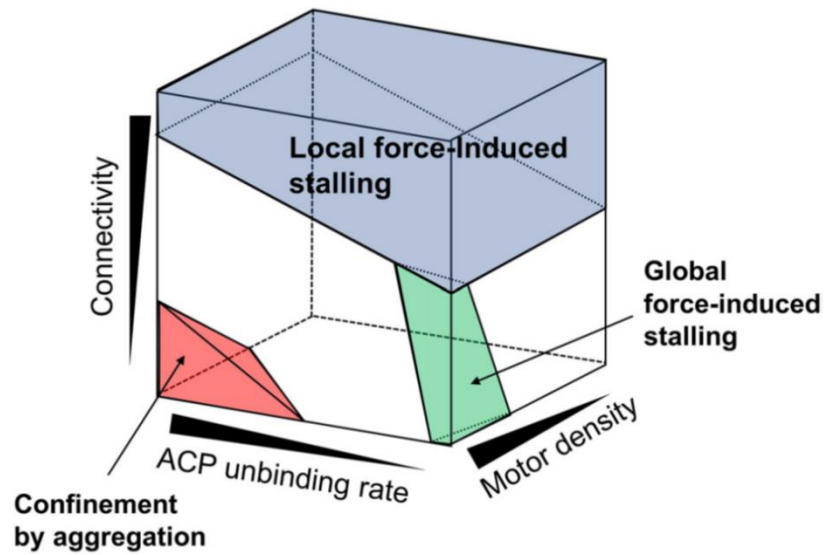
Figure 5.15. Phase diagram showing three mechanisms of motor stalling or confinement in a three-dimensional parametric space consisting of network connectivity, motor density (N_M), and ACP unbinding rate ($k_{u,ACP}^0$). It is assumed that F-actins do not undergo turnover.

Second, global force-induced stalling occurs in networks with low connectivity, many motors, and ACPs that unbind very slowly (Fig. 5.15, green). The ACP unbinding rate needs to be very low to keep the motors stalling for a long time. As network connectivity increases, more motors are required to achieve network-level force transmission between neighboring motors because it becomes harder to transmit forces over a long distance in a network with higher connectivity. Otherwise, with higher network connectivity, slightly faster ACP unbinding is necessary for bringing effective network connectivity to lower level so that global force-induced stalling can arise.

Lastly, motor motions can be confined by network aggregation if motor density and ACP unbinding rate are high, but network connectivity is low (Fig. 5.15, red). We do not call it stalling because motors consistently walk near the center of aggregated structures even after severe network aggregation. As connectivity increases, more motors or faster ACP unbinding events are required for confinement of motor motions via network aggregation.

5.3.6 F-actin turnover can rescue motors from confinement or stalling

The three mechanisms mentioned above were identified without F-actin turnover. Such a condition is similar to many in vitro studies where F-actin does not undergo turnover due to stabilization of F-actin via phalloidin. However, during most of the cellular processes, F-actin turns over very fast via various modes of actin dynamics [169]. Recent computational studies have shown that F-actin turnover can regulate force generation/dissipation and contractile behaviors in actin networks [42, 64, 128, 170, 171]. Common observations in those studies are that F-actin turnover keeps relaxing forces, prevents motors from generating large forces, and suppresses severe network aggregation. To evaluate effects of F-actin turnover on the three mechanisms of motor confinement/stalling, we incorporated F-actin treadmilling by imposing identical polymerization ($k_{+,A}$) and depolymerization rates ($k_{-,A}$) of F-actin. Then, the turnover rate of F-actin, $k_{t,A}$, is equal to $k_{+,A}$ and $k_{-,A}$.

First, we repeated simulations under conditions for local force-induced stalling. We used a network with the highest connectivity, $N_M = 100$, and without ACP unbinding. As the turnover rate of F-actin increases, TE-MSD of two-arm motors becomes larger, and the fraction of stalling and average force exerted on motors are reduced, resulting in enhanced motor motions (Figs. 5.16A, B). With $k_{t,A} = 20$ s^{-1}, TE-MSD, average motor force, and the fraction of stalling become very similar to those of two-arm motors walking in the low-connectivity network (Figs. 5.5B-D). If actin segments disappear due to depolymerization, all ACPs and motors that were bound to the segments are likely to lose connection to F-actin permanently because they cannot rebind to the same segments. Thus, the turnover (i.e. treadmilling) is able to facilitate force relaxation more efficiently than ACP unbinding, which can prevent local force-induced stalling from taking place. Note that these simulations imported a network without noticeable bundle formation unlike other simulations because we found that relatively fast actin turnover changes network morphology substantially if the network initially has bundles formed without actin turnover.
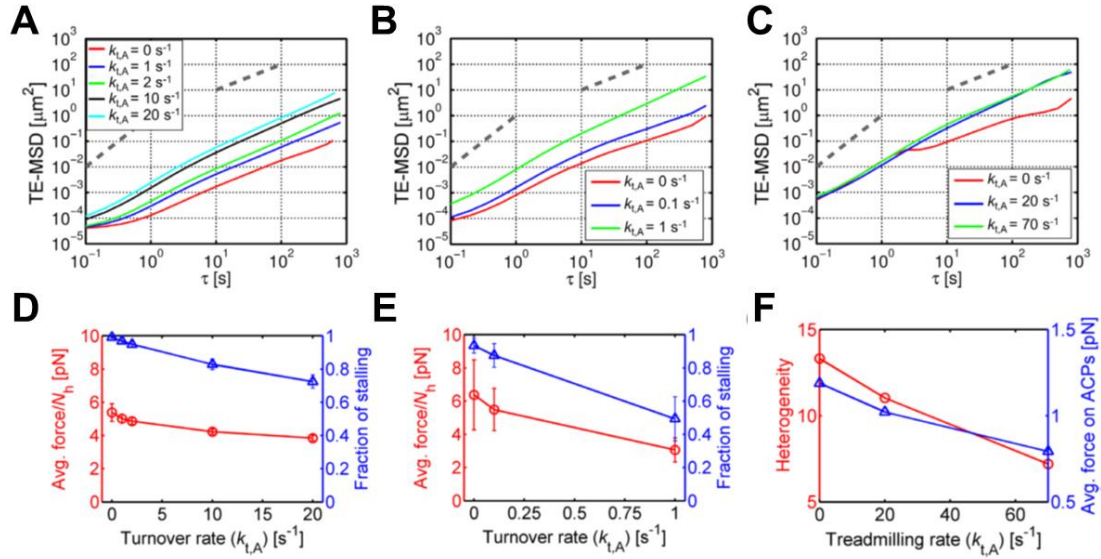
Figure 5.16. Effects of a F-actin turnover rate ($k_{t,A}$) on motions of two-arm motors. All of the simulations used for this figure have 100 motors ($N_M = 100$). (A) TE-MSD of motors in a network with high connectivity in the absence of ACP unbinding. Gray dashed lines indicate the slope of MSD corresponding to diffusive motions ($\sim\tau^1$) and ballistic motions ($\sim\tau^2$). With higher $k_{t,A}$, TE-MSD (time- and ensemble-averaged mean squared displacement) is higher, which indicates less motor stalling. (B) Average force exerted on each myosin head in motor arms and the fraction of stalling decrease with higher $k_{t,A}$. (C) TE- MSD of motors in a network with low connectivity without ACP unbinding. (D) Average force acting on each myosin head in motor arms and the fraction of stalling decrease with higher $k_{t,A}$. (E) TE- MSD of motors in a network with low connectivity. ACPs were allowed to unbind from F-actins with the reference unbinding rate. (F) Network heterogeneity and average force acting on ACPs decrease with higher $k_{t,A}$. For evaluating network morphology, we calculate the radial distribution function, $g(r)$, every 10 s. Then, the average value of $g(r)$ at $0.1\,\mu m < r < 1\,\mu m$, $\bar{g}(t)$, is calculated for each time point. The maximum value of $\bar{g}(t)$ normalized by its initial value, $\bar{g}_{max} / \bar{g}_{init}$, is used as a measure for network heterogeneity. All of the results shown here imply that F-actin turnover prevents motors from being stalled or confined.

Then, we investigated influences of F-actin turnover on global force-induced stalling by imposing different turnover rates on a network with low connectivity, $N_M = 100$, and without ACP unbinding. Even with a slight increase in the turnover rate, TE-MSD significantly increases, whereas average motor force and the fraction of stalling drop significantly, resulting in enhanced motor motions (Figs. 5.16C, D). Spatial distributions of actin segments and motors with very high force (>50 pN) clearly show that force transmission between neighboring motors diminishes as

154

the turnover rate increases (Fig. 5.17A). This indicates that global force-induced stalling of motors is much more sensitive to force relaxation occurring in a network than local force-induced stalling. Indeed, we have shown that global force-induced stalling does not appear even with slow ACP unbinding (Fig. 5.6D), indicating high sensitivity to force relaxation.

Figure 5.17. Effects of F-actin turnover on motions of two-arm motors. (A) Visualization of networks at 800 s under the same condition as that used for Figs. 5.16C, D. An only difference is that F-actins in the center and right cases undergo turnover (i.e. treadmilling). Blue, white, and red represent low, intermediate, and high forces, respectively. Only actins and motors bearing relatively high forces (> 50 pN) are visualized. With faster F-actin turnover, force transmission between motors decreases, resulting in a reduction of global force-induced stalling. (B) Time evolution of network heterogeneity in three cases shown in Figs. 5.16E, F. The averaged value of the radial distribution function was calculated every 10 s. There were 100 motors ($N_M = 100$) in a low-connectivity network, and ACP unbinding was allowed to occur with the reference rate. With $k_{t,A} = 70$ s^{-1}, a network remains relatively homogeneous compared to networks with lower $k_{t,A}$.

Lastly, we repeated simulations under conditions for severe network aggregation. We used a network with low connectivity, $N_M = 100$, and ACP unbinding ($k_{u,ACP}^o = 0.115$ s^{-1}). As the turnover rate increases, TE-MSD of motors increases, and network is more homogeneous without severe aggregation (Figs. 5.16E, F, 5.17B). To explain effects of the turnover rate, we quantified loads acting on ACPs at $t < 100$ s in each case. Since it is expected that only a small portion of

155

ACPs support large loads, we focused on the largest forces (top 5%) supported by ACPs. F-actin turnover reduces the amount of loads on ACPs (Fig. 5.16F). As a result, the ACP unbinding rate does not exponentially increase, so network connectivity is not disrupted significantly by too frequent ACP unbinding events. In addition, clusters formed by network aggregation can be disassembled if the turnover is fast enough. Because of these two effects, network aggregation is suppressed by F-actin turnover, resulting in consistent movements of motors without noticeable confinement.

Overall, with sufficiently fast F-actin turnover, three regimes for confinement and stalling of motors in the phase diagram shown in Fig. 5.15 disappear, implying that myosin motors in cells can keep moving in a superdiffusive, ergodic fashion. It is expected that cells regulate motor motions differently for various physiological functions by controlling F-actin turnover rates.

5.4 Discussion

A myriad of studies showed that cortical actin network and the myosin super family play a very important role in transport of secretory carriers, which are either vesicles or granules, near a plasma membrane [159]. Unconventional myosin proteins 1c, 1e, Va, VI and the non-muscle myosin II are of particular importance [172]. Myosin molecules walking on F-actins transport the carriers actively as their cargos. If there are more than one myosin molecule bound to the cargo, it will be easier for the cargo to maintain connection to F-actins and to hop from one F-actin to the other. However, there can be a tug-of-war between myosin molecules bound to different F-actins oriented in relatively opposite directions. By contrast, if there is only one myosin molecule bound to the cargo, the cargo may keep moving in a unidirectional manner, but it will be harder to maintain connectivity to F-actins for a long time.

Thus, understanding motions of myosin motors in disordered actin networks is very important for defining mechanisms of active transport. Motions of myosin motors have been investigated in a plethora of studies [34, 153, 157, 158]. For example, confinement of myosin motions (i.e. limited mobility) in F-actin networks has been reported in several experimental studies [157, 173]. Various computational studies have suggested possible mechanisms of the motor confinement [157, 158]. In this study, to show how motor motions are confined or restored, we investigated motions of myosin motors in cross-linked F-actin networks using an agent-based

model. The model rigorously accounts for mechanics and dynamics of F-actin, ACP, and motor, including network deformability, force-dependent walking of motors, ACP unbinding, and F-actin turnover.

First, we showed that motors that can bind to one F-actin walk freely in a network regardless of network connectivity because they cannot generate large forces that can make the motors slow down. However, if motors can bind to more than one F-actin, motors can be stalled or slow down due to local force generation. The extent of the local force-induced motor stalling is higher if F-actins in a network are better connected to other F-actins via more ACPs or longer F-actins; motors can develop larger forces on F-actins by pulling them if movement of F-actins is restricted more, but the motors will feel the same amount of forces as reaction forces. Thus, in networks with higher connectivity between F-actins, most of the motors are stalled shortly after they start walking. This is consistent with previous experimental studies showing that motors bound to several filaments exhibit confined movements due to tug-of-war [29]. However, a previous computational study reported that there is no significant difference in motor motions between a bundled network with high connectivity and a homogeneous network with low connectivity [158]. In this study, a few additional tracer motors were put on an actomyosin network that reached a steady-state morphology. Although it was not explained in detail, it is likely that the tracer motors interact with the network in a different way compared to pre-existing motors that drove a change in network morphology. Otherwise, the tracer motors should have been stalled in the bundled network like the pre-existing motors.

We also demonstrated that the tug-of-war may occur at network level, leading to stalling of motors in a network with low connectivity. It was shown in a previous study that forces generated by contractile elements within a network can be transmitted to other contractile elements [174]. If there are a sufficient number of motors so that an average distance between neighboring motors is short enough, forces generated by motors can be transmitted to adjacent motors. Motors initially walk relatively freely, but as a result of mechanical interactions between them, motors eventually find locations where they form a web-like structure that bear large tensile forces at network scale. Then, they are stalled and remain in relatively the same locations for a long time. This network-scale force transmission arises in networks with relatively low connectivity because long-range force transmission through a polymeric network is unlikely to occur in densely cross-linked networks where motors are stalled by local force generation.

In addition, we found that motor motions can be confined due to network aggregation. Motors are not stalled but keep moving around the center of aggregated structures. This is consistent with the previous computational study which demonstrated that aggregation of motors inhibits mobility of motors [158]. Based on these results, we suggested a phase diagram showing how and when motor motions can be confined in disordered networks.

Our study shows that F-actin treadmilling can prevent motors from being stalled or confined, resulting in superdiffusive motions of motors, regardless of motor density, F-actin length, and the density and unbinding rate of ACPs. F-actin turnover induces relaxation of forces acting on motors and ACPs by removing a portion of F-actins. This force relaxation can prevent force-induced stalling of motors and aggregation of F-actins more effectively than ACP unbinding. Suppression of network aggregation via F-actin turnover was demonstrated in previous computational study [42, 64, 128]. In addition, this result is consistent with previous experimental results showing that stabilization of F-actins leads to lower myosin mobility [173]. Since the cell cortex consists of F-actins with fast turnover, it is likely that the stalling and confinement of motors in the cortex are rare events under most physiological conditions. However, motors would walk slower than their unloaded walking velocity since they still bear a certain amount of forces from prestress residing in the cortex. In addition, when the cortex shows aggregating behaviors, such as formation of cytokinetic rings, it is expected that motor motions are confined.

Interestingly, we did not observe a cycling state in which motors are trapped in a network by walking along a closed loop-like structure formed by a few F-actins [157]. The previous study found the cycling state by tracing motors walking on a frozen network structure that may have such a closed loop-like structure permanently. However, in our model, a network cannot have long-lasting loop-like structures because F-actins keep thermally fluctuating or move actively due to forces generated by motors. In cases with F-actin turnover, network morphology changes even more rapidly. Thus, although motors in our model can be trapped in a closed loop-like structure for a short time period, it would not be able to affect motor motions for a longer time.

Some of the results in this study may look similar to previous computational works. For example, a change in network morphology induced by motors has been studied actively during recent decades. In particular, aggregation (i.e. cluster formation) in actomyosin networks has been shown in several studies [25, 110]. Effects of network connectivity or the unbinding rate of ACPs on aggregation have been studied before [158, 175]. However, to our knowledge, these studies did

not investigate and analyze motions of motors as deeply as this study. Compared to those previous works, novelty of this study is quantitative analysis of motor motions under various conditions. In addition, it was shown that movement of F-actins driven by motors is the greatest with intermediate F-actin turnover rates [42], which may look similar to our last results with F-actin turnover. Although we calculated MSDs of F-actins for some cases, our main focus is motions of motors in disordered networks. The extent of active transport can be estimated properly by motions of motors, not by F-actin motions. We also showed clearly how motions can be confined depending on conditions, which has not done in other previous studies in a quantitative manner.

In conclusion, our study demonstrated how motions of myosin motors in cortex-like networks can be regulated by network connectivity, local force generation, network-scale force transmission, and the turnover of ACPs and F-actins. The results from our study provide valuable insights into understanding mechanisms of intracellular transport driven by myosin motors in the actin cytoskeleton beyond those shown in previous studies.

6. CONCLUSIONS AND FUTURE WORK

In this study, we explored the self-organization, contraction, and myosin motion that occurs in the actin cytoskeleton using an agent-based computational model along with *in vitro* experiments. We explored parameters relevant to dynamics and mechanics of the actin cytoskeleton that have not been explored in previous studies and identified important factors that affect self-organization, contraction, and myosin transport.

In Chapter 2, we employed a computational model designed for simulating myosin motility assays with an explicit description of motors that has not been incorporated in previous models. We performed calibration of parameters and showed that the model successfully recapitulated previous experimental observations. We found that repulsive force between filaments and cross-linking play an important role in the motions of F-actins and network morphology.

In Chapter 3, we demonstrated that repulsive forces and bending stiffness of filaments govern the collective motion of filaments as well as pattern formation by determining how easily filaments will be bent upon collisions with other filaments. We showed that high filament concentration and long filaments induce collective behavior, forming rings and band. On the other hand, the bands or the rings could not form with high filament rigidity or too weak repulsive forces. In this case, filaments formed homogeneous networks or flocks, which are loose, transient bundles.

In Chapter 4, we demonstrated that F-actins are fragmented by tensile forces during the contraction of actomyosin networks. We found that F-actin fragmentation can induce contraction of highly connected networks composed of long filaments, which would otherwise not contract. In such cases, the network ruptured catastrophically. On the other hand, in networks composed of short filaments, cross-linker unbinding played an important role and induced gradual contraction of networks. In cells, the catastrophic fracture may not occur due to actin filaments binding to the membrane, which would prevent large force build-up.

In Chapter 5, our study demonstrated how motions of myosin motors in cortex-like networks can be regulated by network connectivity. We found that motor motion can be inhibited, by local force generation and network-scale force transmission. We found that the turnover of ACPs trap motors while F-actin turnover aid motor motion. In cells where F-actin turnover occurs within a few tens of seconds [169], significant trapping of motors would be prevented.

This research, combined with other research endeavors, has the potential to solve challenging problems in biology and engineering. Understanding how the morphology and dynamics of actin are regulated can contribute to identifying new therapeutic targets for diseases resulting from abnormal regulation of actin cytoskeleton dynamics [176]. In tissue engineering, understanding how myosin activity generates force and drives the morphological change of the cortex is important in understanding tissue morphogenesis [177]. Combined with a tissue-level computational model [178], knowledge on actomyosin machinery would enable controlling myosin activity to create tissue with the desired shape. In addition, results from the motility assay study can be utilized in the design of nanorobots, which is a motility assay that can be used to transport and sort molecules [179]. Parameters we identified for the movement and pattern formation of actin filaments can be used to tune the speed and location of transported molecules.

There are ample opportunities for future research through the expansion of the current research. In our study for contraction of cortex-like networks, membrane adhesion of the network was not considered. An *In vitro* experiment shows that actomyosin networks built on lipid bilayers and glass surfaces show different behavior [25]. In a previous study with a lipid bilayer, filaments were mostly buckled due to motor activity [25], whereas our study with a glass surface showed the predominant stretching of filaments. In cells, due to cortex adhesion to the membrane, catastrophic fracture of the actomyosin network found in our study may be prevented. However, it would be also possible that dense cross-linking in the cell cortex prefers stretching over buckling. A computational model of the actomyosin network adhered to the membrane can reveal the role of the membrane and cross-linking in regulating cortical tension and morphology. Another way to expand the current research is incorporating mechanosensitive binding of an actin-binding protein to an actin filament [180]. For example, it has been shown that tension on actin filaments enhances the binding of α-catenin, an actin-binding protein [181]. α-actinin, another actin-binding protein, was shown to exhibit catch-bond behavior, meaning that the protein can accumulate on actin filaments under high tension [182]. Incorporating membrane and other binding proteins with mechanosensitivity into the model would lead to an interesting and more physiologically relevant discovery of the mechanical properties of the actomyosin networks.

REFERENCES

1.   Lodish, H., et al., *Molecular cell biology*. 2008: Macmillan.

2.   Pollard, T.D., *Actin and actin-binding proteins.* Cold Spring Harbor perspectives in biology, 2016. **8**(8): p. a018226.

3.   Tojkander, S., et al., *A molecular pathway for myosin II recruitment to stress fibers.* Current Biology, 2011. **21**(7): p. 539-550.

4.   Svitkina, T.M., *Actin cell cortex: structure and molecular organization.* Trends in cell biology, 2020.

5.   Howard, J., *Mechanics of motor proteins and the cytoskeleton.* 2001.

6.   Lieleg, O., M.M. Claessens, and A.R. Bausch, *Structure and dynamics of cross-linked actin networks.* Soft Matter, 2010. **6**(2): p. 218-225.

7.   Kadzik, R.S., K.E. Homa, and D.R. Kovar, *F-Actin Cytoskeleton Network Self-Organization Through Competition and Cooperation.* Annual Review of Cell and Developmental Biology, 2020. **36**: p. 35-60.

8.   Bausch, A. and K. Kroy, *A bottom-up approach to cell mechanics.* Nature physics, 2006. **2**(4): p. 231-238.

9.   Huber, L., et al., *Emergence of coexisting ordered states in active matter systems.* Science, 2018. **361**(6399): p. 255-258.

10.   Yanagida, T., et al., *Direct observation of motion of single F-actin filaments in the presence of myosin.* Nature, 1984. **307**(5946): p. 58-60.

11.   Butt, T., et al., *Myosin motors drive long range alignment of actin filaments.* Journal of Biological Chemistry, 2010. **285**(7): p. 4964-4974.

12.   Sciortino, A. and A.R. Bausch, *Pattern formation and polarity sorting of driven actin filaments on lipid membranes.* Proceedings of the National Academy of Sciences, 2021. **118**(6).

13.   Schaller, V., et al., *Crosslinking proteins modulate the self-organization of driven systems.* Soft Matter, 2013. **9**(30): p. 7229-33.

14.   Moore, J.M., et al., *Collective motion of driven semiflexible filaments tuned by soft repulsion and stiffness.* Soft Matter, 2020. **16**(41): p. 9436-9442.

15.   Sumino, Y., et al., *Large-scale vortex lattice emerging from collectively moving microtubules.* Nature, 2012. **483**(7390): p. 448.

16. Inoue, D., et al., *Depletion force induced collective motion of microtubules driven by kinesin.* Nanoscale, 2015. **7**(43): p. 18054-18061.

17. Paluch, E., J. van der Gucht, and C. Sykes, *Cracking up: symmetry breaking in cellular systems.* The Journal of cell biology, 2006. **175**(5): p. 687-692.

18. Álvarez-González, B., et al., *Three-dimensional balance of cortical tension and axial contractility enables fast amoeboid migration.* Biophysical journal, 2015. **108**(4): p. 821-832.

19. Kasza, K.E., S. Supriyatno, and J.A. Zallen, *Cellular defects resulting from disease-related myosin II mutations in Drosophila.* Proceedings of the National Academy of Sciences, 2019. **116**(44): p. 22205-22211.

20. Gebala, V., et al., *Blood flow drives lumen formation by inverse membrane blebbing during angiogenesis in vivo.* Nature cell biology, 2016. **18**(4): p. 443-450.

21. Koenderink, G.H. and E.K. Paluch, *Architecture shapes contractility in actomyosin networks.* Current opinion in cell biology, 2018. **50**: p. 79-85.

22. Bendix, P.M., et al., *A quantitative analysis of contractility in active cytoskeletal protein networks.* Biophysical journal, 2008. **94**(8): p. 3126-3136.

23. Chugh, P., et al., *Actin cortex architecture regulates cell surface tension.* Nature cell biology, 2017. **19**(6): p. 689-697.

24. Alvarado, J., et al., *Molecular motors robustly drive active gels to a critically connected state.* Nature Physics, 2013. **9**(9): p. 591-597.

25. Murrell, M.P. and M.L. Gardel, *F-actin buckling coordinates contractility and severing in a biomimetic actomyosin cortex.* Proceedings of the National Academy of Sciences, 2012. **109**(51): p. 20820-20825.

26. Vogel, S.K., et al., *Myosin motors fragment and compact membrane-bound actin filaments.* Elife, 2013. **2**: p. e00116.

27. Li, J., et al., *Buckling-induced F-actin fragmentation modulates the contraction of active cytoskeletal networks.* Soft Matter, 2017. **13**(17): p. 3213-3220.

28. Schuh, M., *An actin-dependent mechanism for long-range vesicle transport.* Nature cell biology, 2011. **13**(12): p. 1431-1436.

29. Lombardo, A.T., et al., *Myosin Va transport of liposomes in three-dimensional actin networks is modulated by actin filament density, position, and polarity.* Proceedings of the National Academy of Sciences, 2019. **116**(17): p. 8326-8335.

30. Moerner, W.E., *New directions in single-molecule imaging and analysis.* Proceedings of the National Academy of Sciences, 2007. **104**(31): p. 12596-12602.

31.   Kulkarni, R.P., et al., *Intracellular transport dynamics of endosomes containing DNA polyplexes along the microtubule network.* Biophysical journal, 2006. **90**(5): p. L42-L44.

32.   Huet, S., et al., *Analysis of transient behavior in complex trajectories: application to secretory vesicle dynamics.* Biophysical journal, 2006. **91**(9): p. 3542-3559.

33.   Desnos, C., et al., *Rab27A and its effector MyRIP link secretory granules to F-actin and control their motion towards release sites.* The Journal of cell biology, 2003. **163**(3): p. 559-570.

34.   Scholz, M., et al., *Tuning molecular motor transport through cytoskeletal filament network organization.* Soft matter, 2020. **16**(8): p. 2135-2140.

35.   Appert-Rolland, C., M. Ebbinghaus, and L. Santen, *Intracellular transport driven by cytoskeletal motors: General mechanisms and defects.* Physics Reports, 2015. **593**: p. 1-59.

36.   Gardel, M.L., et al., *Elastic behavior of cross-linked and bundled actin networks.* Science, 2004. **304**(5675): p. 1301-5.

37.   Sawyer, G.M., et al., *Disease-associated substitutions in the filamin B actin binding domain confer enhanced actin binding affinity in the absence of major structural disturbance: Insights from the crystal structures of filamin B actin binding domains.* Journal of molecular biology, 2009. **390**(5): p. 1030-1047.

38.   Gbadegesin, R.A., et al., *Mutations in the gene that encodes the F-actin binding protein anillin cause FSGS.* Journal of the American Society of Nephrology, 2014. **25**(9): p. 1991-2002.

39.   Weins, A., et al., *Disease-associated mutant α-actinin-4 reveals a mechanism for regulating its F-actin-binding affinity.* Proceedings of the National Academy of Sciences, 2007. **104**(41): p. 16080-16085.

40.   Rief, M., et al., *Myosin-V stepping kinetics: a molecular model for processivity.* Proceedings of the National Academy of Sciences, 2000. **97**(17): p. 9482-9486.

41.   Capitanio, M. and F.S. Pavone, *Interrogating biology with force: single molecule high-resolution measurements with optical tweezers.* Biophysical journal, 2013. **105**(6): p. 1293-1303.

42.   Popov, K., J. Komianos, and G.A. Papoian, *MEDYAN: Mechanochemical simulations of contraction and polarity alignment in actomyosin networks.* PLoS computational biology, 2016. **12**(4): p. e1004877.

43.   Kim, T., et al., *Computational analysis of viscoelastic properties of crosslinked actin networks.* PLoS Comput Biol, 2009. **5**(7): p. e1000439.

44. Jung, W., et al., *Collective and Contractile Filament Motions in the Myosin Motility Assay.* Soft Matter, 2020.

45. Gardel, M.L., et al., *Chapter 19: Mechanical response of cytoskeletal networks.* Methods Cell Biol., 2008. **89**: p. 487-519.

46. Murrell, M., et al., *Forcing cells into shape: the mechanics of actomyosin contractility.* Nat. Rev. Mol. Cell Biol., 2015. **16**(8): p. 486-98.

47. Schliwa, M. and G. Woehlke, *Molecular motors.* Nature, 2003. **422**(6933): p. 759-65.

48. Spudich, J.A., *The myosin swinging cross-bridge model.* Nat. Rev. Mol. Cell Biol., 2001. **2**(5): p. 387-92.

49. Iwase, T., Y. Sasaki, and K. Hatori, *Alignment of actin filament streams driven by myosin motors in crowded environments.* Biochimica et Biophysica Acta (BBA)-General Subjects, 2017. **1861**(11): p. 2717-2725.

50. Schaller, V. and A.R. Bausch, *Topological defects and density fluctuations in collectively moving systems.* Proc. Natl. Acad. Sci. U. S. A., 2013. **110**(12): p. 4488-93.

51. Schaller, V., et al., *Polar pattern formation: hydrodynamic coupling of driven filaments.* Soft Matter, 2011. **7**(7): p. 3213-8.

52. Schaller, V., et al., *Polar patterns of driven filaments.* Nature, 2010. **467**(7311): p. 73-7.

53. Suzuki, R. and A.R. Bausch, *The emergence and transient behaviour of collective motion in active filament systems.* Nat. Commun., 2017. **8**(1): p. 41.

54. Suzuki, R., et al., *Polar pattern formation in driven filament systems require non-binary particle collisions.* Nat. Phys., 2015. **11**(10): p. 839-43.

55. Schaller, V., B. Hammerich, and A.R. Bausch, *Active compaction of crosslinked driven filament networks.* Eur. Phys. J. E Soft Matter, 2012. **35**(8): p. 81.

56. Schaller, V., et al., *Frozen steady states in active systems.* Proc. Natl. Acad. Sci. U. S. A., 2011. **108**(48): p. 19183-8.

57. Vilfan, A., *Twirling motion of actin filaments in gliding assays with nonprocessive Myosin motors.* Biophys. J., 2009. **97**(4): p. 1130-7.

58. Egan, P., et al., *Emergent systems energy laws for predicting myosin ensemble processivity.* PLoS Comput. Biol., 2015. **11**(4): p. e1004177.

59. Freedman, S.L., et al., *A versatile framework for simulating the dynamic mechanical structure of cytoskeletal networks.* Biophys. J., 2017. **113**(2): p. 448-460.

60. Ishigure, Y. and T. Nitta, *Simulating an Actomyosin in Vitro Motility Assay: Toward the Rational Design of Actomyosin-Based Microtransporters.* IEEE Trans. Nanobioscience, 2015. **14**(6): p. 641-8.

61. Kim, T., *Determinants of contractile forces generated in disorganized actomyosin bundles.* Biomech. Model. Mechanobiol., 2015. **14**(2): p. 345-55.

62. Bidone, T.C., et al., *Morphological transformation and force generation of active cytoskeletal networks.* PLoS computational biology, 2017. **13**(1): p. e1005277.

63. Jung, W., M.P. Murrell, and T. Kim, *F-actin cross-linking enhances stability of force generation in disordered actomyosin networks.* Comput. Part. Mech., 2015. **2**(4): p. 317-27.

64. Mak, M., et al., *Interplay of active processes modulates tension and drives phase transition in self-renewing, motor-driven cytoskeletal networks.* Nature communications, 2016. **7**(1): p. 1-12.

65. Underhill, P.T. and P.S. Doyle, *On the coarse-graining of polymers into bead-spring chains.* J. Non-Newton. Fluid., 2004. **122**(1): p. 3-31.

66. Clift, R., J.R. Grace, and M.E. Weber, *Bubbles, drops, and particles*. 2005: Courier Corporation.

67. Bell, G.I., *Models for the specific adhesion of cells to cells.* Science, 1978. **200**(4342): p. 618-27.

68. Ferrer, J.M., et al., *Measuring molecular rupture forces between single actin filaments and actin-binding proteins.* Proceedings of the National Academy of Sciences, 2008. **105**(27): p. 9221-9226.

69. Kishino, A. and T. Yanagida, *Force measurements by micromanipulation of a single actin filament by glass needles.* Nature, 1988. **334**(6177): p. 74-76.

70. Isambert, H., et al., *Flexibility of actin filaments derived from thermal fluctuations. Effect of bound nucleotide, phalloidin, and muscle regulatory proteins.* J. Biol. Chem., 1995. **270**(19): p. 11437-44.

71. Meyer, R.K. and U. Aebi, *Bundling of actin filaments by alpha-actinin depends on its molecular length.* J. Cell Biol., 1990. **110**(6): p. 2013-2024.

72. Erdmann, T., P.J. Albert, and U.S. Schwarz, *Stochastic dynamics of small ensembles of non-processive molecular motors: The parallel cluster model.* J. Chem. Phys., 2013. **139**(17): p. 175104.

73. Erdmann, T. and U.S. Schwarz, *Stochastic force generation by small ensembles of myosin II motors.* Physical review letters, 2012. **108**(18): p. 188101.

74. Cuda, G., et al., *In vitro actin filament sliding velocities produced by mixtures of different types of myosin.* Biophys. J., 1997. **72**(4): p. 1767-79.

75. Umemoto, S. and J.R. Sellers, *Characterization of in vitro motility assays using smooth muscle and cytoplasmic myosins.* J. Biol. Chem., 1990. **265**(25): p. 14864-9.

76. Harris, D.E. and D.M. Warshaw, *Smooth and skeletal muscle myosin both exhibit low duty cycles at zero load in vitro.* J. Biol. Chem., 1993. **268**(20): p. 14764-8.

77. Koenderink, G.H., et al., *An active biopolymer network controlled by molecular motors.* Proc. Natl. Acad. Sci. U. S. A., 2009. **106**(36): p. 15192-7.

78. Uyeda, T.Q., S.J. Kron, and J.A. Spudich, *Myosin step size: estimation from slow sliding movement of actin over low densities of heavy meromyosin.* J. Mol. Biol., 1990. **214**(3): p. 699-710.

79. Debold, E.P., et al., *Phosphate enhances myosin-powered actin filament velocity under acidic conditions in a motility assay.* Am. J. Physiol. Regul. Integr. Comp. Physiol., 2011. **300**(6): p. R1401-R1408.

80. Ozawa, K., et al., *Millimeter-sized belt-like pattern formation of actin filaments in solution by interacting with surface myosin in vitro.* Biophysics and physicobiology, 2019. **16**: p. 1-8.

81. Rickman, J., F. Nédélec, and T. Surrey, *Effects of spatial dimensionality and steric interactions on microtubule-motor self-organization.* Phys. biol., 2019. **16**(4): p. 046004.

82. Wada, S., et al., *Effect of length and rigidity of microtubules on the size of ring-shaped assemblies obtained through active self-organization.* Soft Matter, 2015. **11**(6): p. 1151-1157.

83. Belmonte, J.M., M. Leptin, and F. Nedelec, *A theory that predicts behaviors of disordered cytoskeletal networks.* Mol. Syst. Biol., 2017. **13**: p. 941.

84. Alvarado, J., et al., *Force percolation of contractile active gels.* Soft matter, 2017. **13**(34): p. 5624-5644.

85. Lenz, M., *Geometrical origins of contractility in disordered actomyosin networks.* Phys. Rev. X, 2014. **4**(4): p. 041002.

86. Lenz, M., et al., *Contractile units in disordered actomyosin bundles arise from F-actin buckling.* Phys. Rev. Lett., 2012. **108**(23): p. 238107.

87. Laporte, D., et al., *α-Actinin and fimbrin cooperate with myosin II to organize actomyosin bundles during contractile-ring assembly.* Mol. Biol. Cell, 2012. **23**(16): p. 3094-3110.

88. Tee, S.-Y., A.R. Bausch, and P.A. Janmey, *The mechanical cell.* Current Biology, 2009. **19**(17): p. R745-R748.

89.   Cai, Y., et al., *Nonmuscle myosin IIA-dependent force inhibits cell spreading and drives F-actin flow.* Biophysical journal, 2006. **91**(10): p. 3907-3920.

90.   Mishra, M., et al., *In vitro contraction of cytokinetic ring depends on myosin II but not on actin dynamics.* Nature cell biology, 2013. **15**(7): p. 853-859.

91.   Martin, A.C., M. Kaschube, and E.F. Wieschaus, *Pulsed contractions of an actin–myosin network drive apical constriction.* Nature, 2009. **457**(7228): p. 495-499.

92.   Medeiros, N.A., D.T. Burnette, and P. Forscher, *Myosin II functions in actin-bundle turnover in neuronal growth cones.* Nature cell biology, 2006. **8**(3): p. 216-226.

93.   Guha, M., M. Zhou, and Y.-l. Wang, *Cortical actin turnover during cytokinesis requires myosin II.* Current biology, 2005. **15**(8): p. 732-736.

94.   Ennomani, H., et al., *Architecture and connectivity govern actin network contractility.* Current Biology, 2016. **26**(5): p. 616-626.

95.   Toyoshima, Y.Y., et al., *Myosin subfragment-1 is sufficient to move actin filaments in vitro.* Nature, 1987. **328**(6130): p. 536-539.

96.   Weber, C.A., et al., *Random bursts determine dynamics of active filaments.* Proceedings of the National Academy of Sciences, 2015. **112**(34): p. 10703-10707.

97.   Prathyusha, K., S. Henkes, and R. Sknepnek, *Dynamically generated patterns in dense suspensions of active filaments.* Physical Review E, 2018. **97**(2): p. 022606.

98.   Guiet, R., et al., *Macrophage mesenchymal migration requires podosome stabilization by filamin A.* Journal of Biological Chemistry, 2012. **287**(16): p. 13051-13062.

99.   Song, J., et al., *Reorganization of structural proteins in vascular smooth muscle cells grown in collagen gel and basement membrane matrices (Matrigel): a comparison with their in situ counterparts.* Journal of structural biology, 2001. **133**(1): p. 43-54.

100.   Beach, J.R., et al., *Nonmuscle myosin II isoforms coassemble in living cells.* Current Biology, 2014. **24**(10): p. 1160-1166.

101.   Kovács, M., et al., *Functional divergence of human cytoplasmic myosin ii kinetic characterization of the non-muscle iia isoform.* Journal of Biological Chemistry, 2003. **278**(40): p. 38132-38140.

102.   Kron, S.J. and J.A. Spudich, *Fluorescent actin filaments move on myosin fixed to a glass surface.* Proceedings of the National Academy of Sciences, 1986. **83**(17): p. 6272-6276.

103.   Nagy, A., et al., *Kinetic characterization of nonmuscle myosin IIb at the single molecule level.* Journal of Biological Chemistry, 2013. **288**(1): p. 709-722.

104.   Norstrom, M.F., P.A. Smithback, and R.S. Rock, *Unconventional processive mechanics of non-muscle myosin IIB.* Journal of Biological Chemistry, 2010. **285**(34): p. 26326-26334.

105.   Woodhead, J.L., et al., *Atomic model of a myosin filament in the relaxed state.* Nature, 2005. **436**(7054): p. 1195-1199.

106.   Robert, T.H., et al., *Actin-myosin interaction. Self-assembly into a bipolar "contractile unit".* Journal of molecular biology, 1977. **111**(2): p. 159-171.

107.   Kachar, B., *Polarity and velocity of sliding filaments: control of direction by actin and of speed by myosin.* Science, 1990. **249**(4967): p. 406-408.

108.   TOYOSHIMA, Y.Y., *Bidirectional movement of actin filaments along tracks of heavy meromyosin and native thick filaments.* Journal of Cell Science, 1991. **1991**(Supplement 14): p. 83-85.

109.   Janson, L.W., J. Kolega, and D.L. Taylor, *Modulation of contraction by gelation/solation in a reconstituted motile model.* The Journal of cell biology, 1991. **114**(5): p. 1005-1015.

110.   Wollrab, V., et al., *Polarity sorting drives remodeling of actin-myosin networks.* Journal of cell science, 2019. **132**(4).

111.   Matsuda, K., et al., *Visualizing dynamic actin cross-linking processes driven by the actin-binding protein anillin.* FEBS letters, 2020. **594**(8): p. 1237-1247.

112.   Harada, Y., et al., *Mechanochemical coupling in actomyosin energy transduction studied by in vitro movement assay.* Journal of molecular biology, 1990. **216**(1): p. 49-68.

113.   Jung, W., M.P. Murrell, and T. Kim, *F-actin fragmentation induces distinct mechanisms of stress relaxation in the actin cytoskeleton.* ACS Macro Letters, 2016. **5**(6): p. 641-645.

114.   Tsuda, Y., et al., *Torsional rigidity of single actin filaments and actin–actin bond breaking force under torsion measured directly by in vitro micromanipulation.* Proceedings of the National Academy of Sciences, 1996. **93**(23): p. 12937-12942.

115.   Pardee, J.D. and J. Aspudich, *[18] Purification of muscle actin*, in *Methods in enzymology.* 1982, Elsevier. p. 164-181.

116.   Yajima, J., et al., *Direct long-term observation of kinesin processivity at low load.* Current biology, 2002. **12**(4): p. 301-306.

117.   Field, C.M. and B.M. Alberts, *Anillin, a contractile ring protein that cycles from the nucleus to the cell cortex.* The Journal of cell biology, 1995. **131**(1): p. 165-178.

118.   Yamaguchi, S., et al., *Torque generation by axonemal outer-arm dynein.* Biophysical journal, 2015. **108**(4): p. 872-879.

119. Yamagishi, M., et al., *Structural basis of backwards motion in kinesin-1-kinesin-14 chimera: Implication for kinesin-14 motility.* Structure, 2016. **24**(8): p. 1322-1334.

120. Hartigan, J.A. and M.A. Wong, *Algorithm AS 136: A k-means clustering algorithm.* Journal of the royal statistical society. series c (applied statistics), 1979. **28**(1): p. 100-108.

121. Koehler, S., V. Schaller, and A.R. Bausch, *Collective dynamics of active cytoskeletal networks.* PloS one, 2011. **6**(8): p. e23798.

122. Yin, H.L. and T.P. Stossel, *Control of cytoplasmic actin gel–sol transformation by gelsolin, a calcium-dependent regulatory protein.* Nature, 1979. **281**(5732): p. 583-586.

123. Kumar, S., et al., *Viscoelastic retraction of single living stress fibers and its impact on cell shape, cytoskeletal organization, and extracellular matrix mechanics.* Biophysical journal, 2006. **90**(10): p. 3762-3773.

124. McCullough, B.R., et al., *Cofilin-linked changes in actin filament flexibility promote severing.* Biophysical journal, 2011. **101**(1): p. 151-159.

125. Takiguchi, K., *Heavy meromyosin induces sliding movements between antiparallel actin filaments.* The Journal of Biochemistry, 1991. **109**(4): p. 520-527.

126. Lieleg, O., et al., *Transient binding and dissipation in cross-linked actin networks.* Physical review letters, 2008. **101**(10): p. 108101.

127. Lieleg, O., et al., *Cytoskeletal polymer networks: viscoelastic properties are determined by the microscopic interaction potential of cross-links.* Biophysical journal, 2009. **96**(11): p. 4725-4732.

128. Hiraiwa, T. and G. Salbreux, *Role of turnover in active stress generation in a filament network.* Physical review letters, 2016. **116**(18): p. 188101.

129. Mak, M., et al., *Interplay of active processes modulates tension and drives phase transition in self-renewing, motor-driven cytoskeletal networks.* Nature Communications, 2016. **7**: p. 10323.

130. Fenix, A.M., et al., *Expansion and concatenation of nonmuscle myosin IIA filaments drive cellular contractile system formation during interphase and mitosis.* Molecular biology of the cell, 2016. **27**(9): p. 1465-1478.

131. Vicente-Manzanares, M., et al., *Non-muscle myosin II takes centre stage in cell adhesion and migration.* Nature reviews Molecular cell biology, 2009. **10**(11): p. 778-790.

132. Schmoller, K., et al., *Cyclic hardening in bundled actin networks.* Nature communications, 2010. **1**(1): p. 1-8.

133. Gardel, M., et al., *Scaling of F-actin network rheology to probe single filament elasticity and dynamics.* Physical review letters, 2004. **93**(18): p. 188102.

134.	Jung, W., et al., *Dynamic motions of molecular motors in the actin cytoskeleton.* Cytoskeleton, 2019. **76**(11-12): p. 517-531.

135.	Hirokawa, N., S. Niwa, and Y. Tanaka, *Molecular motors in neurons: transport mechanisms and roles in brain function, development, and disease.* Neuron, 2010. **68**(4): p. 610-638.

136.	Maxfield, F.R. and A.K. Menon, *Intracellular sterol transport and distribution.* Current opinion in cell biology, 2006. **18**(4): p. 379-385.

137.	Caspi, A., R. Granek, and M. Elbaum, *Diffusion and directed motion in cellular transport.* Physical Review E, 2002. **66**(1): p. 011916.

138.	Johns, L.M., et al., *Restriction of secretory granule motion near the plasma membrane of chromaffin cells.* The Journal of cell biology, 2001. **153**(1): p. 177-190.

139.	Steyer, J.A., H. Horstmann, and W. Almers, *Transport, docking and exocytosis of single secretory granules in live chromaffin cells.* Nature, 1997. **388**(6641): p. 474-478.

140.	Zhuravlev, P.I., et al., *Theory of active transport in filopodia and stereocilia.* Proceedings of the National Academy of Sciences, 2012. **109**(27): p. 10849-10854.

141.	Dix, J.A. and A. Verkman, *Crowding effects on diffusion in solutions and cells.* Annu. Rev. Biophys., 2008. **37**: p. 247-263.

142.	Reverey, J.F., et al., *Superdiffusion dominates intracellular particle motion in the supercrowded cytoplasm of pathogenic Acanthamoeba castellanii.* Scientific reports, 2015. **5**(1): p. 1-14.

143.	Müller, M.J., S. Klumpp, and R. Lipowsky, *Tug-of-war as a cooperative mechanism for bidirectional cargo transport by molecular motors.* Proceedings of the National Academy of Sciences, 2008. **105**(12): p. 4609-4614.

144.	Vale, R.D., *Intracellular transport using microtubule-based motors.* Annual review of cell biology, 1987. **3**(1): p. 347-378.

145.	Gross, S.P., *Hither and yon: a review of bi-directional microtubule-based transport.* Physical biology, 2004. **1**(2): p. R1.

146.	Ross, J.L., M.Y. Ali, and D.M. Warshaw, *Cargo transport: molecular motors navigate a complex cytoskeleton.* Current opinion in cell biology, 2008. **20**(1): p. 41-47.

147.	Mallik, R. and S.P. Gross, *Molecular motors: strategies to get along.* Current Biology, 2004. **14**(22): p. R971-R982.

148.	Brown, S.S., *Cooperation between microtubule-and actin-based motor proteins.* Annual review of cell and developmental biology, 1999. **15**(1): p. 63-80.

149.   Meunier, F.A. and L.M. Gutiérrez, *Captivating new roles of F-actin cortex in exocytosis and bulk endocytosis in neurosecretory cells.* Trends in neurosciences, 2016. **39**(9): p. 605-613.

150.   Trifaró, J.M., S. Gasman, and L. Gutierrez, *Cytoskeletal control of vesicle transport and exocytosis in chromaffin cells.* Acta Physiologica, 2008. **192**(2): p. 165-172.

151.   Rudolf, R., et al., *Myosin Va facilitates the distribution of secretory granules in the F-actin rich cortex of PC12 cells.* Journal of Cell Science, 2003. **116**(7): p. 1339-1348.

152.   Cugliandolo, L., J. Kurchan, and F. Ritort, *Evidence of aging in spin-glass mean-field models.* Physical Review B, 1994. **49**(9): p. 6331.

153.   Burov, S., et al., *Distribution of directional change as a signature of complex dynamics.* Proceedings of the National Academy of Sciences, 2013. **110**(49): p. 19689-19694.

154.   Ando, D., et al., *Cytoskeletal network morphology regulates intracellular transport dynamics.* Biophysical journal, 2015. **109**(8): p. 1574-1582.

155.   Maelfeyt, B., S.A. Tabei, and A. Gopinathan, *Anomalous intracellular transport phases depend on cytoskeletal network features.* Physical Review E, 2019. **99**(6): p. 062404.

156.   Mlynarczyk, P.J. and S.M. Abel, *First passage of molecular motors on networks of cytoskeletal filaments.* Physical Review E, 2019. **99**(2): p. 022406.

157.   Scholz, M., et al., *Cycling state that can lead to glassy dynamics in intracellular transport.* Physical Review X, 2016. **6**(1): p. 011037.

158.   Freedman, S.L., et al., *Nonequilibrium phase diagrams for actomyosin networks.* Soft matter, 2018. **14**(37): p. 7740-7747.

159.   Bond, L.M., et al., *Myosin motor proteins are involved in the final stages of the secretory pathways.* Biochemical Society Transactions, 2011. **39**(5): p. 1115-1119.

160.   Linsmeier, I., et al., *Disordered actomyosin networks are sufficient to produce cooperative and telescopic contractility.* Nature communications, 2016. **7**(1): p. 1-9.

161.   Falzone, T.T., et al., *Assembly kinetics determine the architecture of α-actinin crosslinked F-actin networks.* Nature communications, 2012. **3**(1): p. 1-9.

162.   Wachsstock, D.H., W. Schwartz, and T.D. Pollard, *Affinity of alpha-actinin for actin determines the structure and mechanical properties of actin filament gels.* Biophysical journal, 1993. **65**(1): p. 205-214.

163.   Nguyen, L.T., et al., *Molecular dynamics simulation of F-actin reveals the role of cross-linkers in semi-flexible filament assembly.* Soft Matter, 2009. **5**(10): p. 2033-2036.

164. Tabei, S.A., et al., *Intracellular transport of insulin granules is a subordinated random walk.* Proceedings of the National Academy of Sciences, 2013. **110**(13): p. 4911-4916.

165. Mason, T.G., et al., *Particle tracking microrheology of complex fluids.* Physical review letters, 1997. **79**(17): p. 3282.

166. Murrell, M. and M.L. Gardel, *Actomyosin sliding is attenuated in contractile biomimetic cortices.* Molecular biology of the cell, 2014. **25**(12): p. 1845-1853.

167. Xu, J., D. Wirtz, and T.D. Pollard, *Dynamic cross-linking by α-actinin determines the mechanical properties of actin filament networks.* Journal of Biological Chemistry, 1998. **273**(16): p. 9570-9576.

168. Skubiszak, L. and L. Kowalczyk, *Myosin molecule packing within the vertebrate skeletal muscle thick filaments. A complete bipolar model.* Acta Biochimica Polonica, 2002. **49**(4): p. 829-840.

169. Chugh, P. and E.K. Paluch, *The actin cortex at a glance.* Journal of cell science, 2018. **131**(14).

170. McFadden, W.M., et al., *Filament turnover tunes both force generation and dissipation to control long-range flows in a model actomyosin cortex.* PLoS computational biology, 2017. **13**(12): p. e1005811.

171. Chandrasekaran, A., A. Upadhyaya, and G.A. Papoian, *Remarkable structural transformations of actin bundles are driven by their initial polarity, motor activity, crosslinking, and filament treadmilling.* PLoS computational biology, 2019. **15**(7): p. e1007156.

172. Loubery, S. and E. Coudrier, *Myosins in the secretory pathway: tethers or transporters?* Cellular and molecular life sciences: CMLS, 2008. **65**(18): p. 2790-2800.

173. Lang, T., et al., *Role of actin cortex in the subplasmalemmal transport of secretory granules in PC-12 cells.* Biophysical journal, 2000. **78**(6): p. 2863-2877.

174. Ronceray, P., C.P. Broedersz, and M. Lenz, *Fiber networks amplify active stress.* Proceedings of the national academy of sciences, 2016. **113**(11): p. 2827-2832.

175. Schuppler, M., et al., *Boundaries steer the contraction of active gels.* Nature communications, 2016. **7**(1): p. 1-10.

176. Sprenkeler, E.G., S.D. Webbers, and T.W. Kuijpers, *When Actin is not actin'like it should: a new category of distinct primary immunodeficiency disorders.* Journal of Innate Immunity, 2021. **13**(1): p. 3-25.

177. Kasza, K.E. and J.A. Zallen, *Dynamics and regulation of contractile actin–myosin networks in morphogenesis.* Current opinion in cell biology, 2011. **23**(1): p. 30-38.

178. Fletcher, A.G., et al., *Vertex models of epithelial morphogenesis.* Biophysical journal, 2014. **106**(11): p. 2291-2304.

179. Isozaki, N., et al., *Control of molecular shuttles by designing electrical and mechanical properties of microtubules.* Science Robotics, 2017. **2**(10).

180. Jégou, A. and G. Romet-Lemonne, *Mechanically tuning actin filaments to modulate the action of actin-binding proteins.* Current Opinion in Cell Biology, 2021. **68**: p. 72-80.

181. Mei, L., et al., *Molecular mechanism for direct actin force-sensing by α-catenin.* Elife, 2020. **9**: p. e62514.

182. Thomas, D.G. and D.N. Robinson. *The fifth sense: Mechanosensory regulation of alpha-actinin-4 and its relevance for cancer metastasis.* in *Seminars in cell & developmental biology.* 2017. Elsevier.